ISSN 2222-5617

МІНІСТЕРСТВО ОСВІТИ І НАУКИ УКРАЇНИ

Вісник Харківського Національного Університету імені В.Н.Каразіна

Серія “Фізика”

Випуск 25

Серія започаткована 1998 р.

Харків 2016

УДК 530.1/539.8

Вісник містить статті, присвячені сучасному стану теоретичних та експериментальних досліджень у галузі фізики Видання призначене для науковців, викладачів, аспірантів та студентів фізичних спеціальностей вищих навчальних закладів та наукових установ.
Видання є фаховим у галузі фіз.-мат. наук (фізика) наказ МОН України №1328 від 21.12.2015.

Затверджено до друку рішенням Вченої ради Харківського національного університету імені В.Н.Каразіна (протокол №1 від 23 січня 2017 р.)

Адреса редакції:
Україна, 61022, Харків, майдан Свободи, 4, Харківський національний університет імені В.Н. Каразіна, фізичний факультет, 057-707-53-83, ruslan.v.vovk@univer.kharkov.ua
Статті пройшли внутрішнє та зовнішнє рецензування.

Свідоцтво про державну реєстрацію КВ №21573-11473Р від 20.08.2015

UDC 530.1/539.8

Bulletin contains articles on the current state of theoretical and experimental research in the field of physics.
The publication is intended for researchers, teachers and students of physical specialties of higher education and research institutions.
The publication is a professional in the field of physics and mathematics science (Physics) ordered MES of Ukraine #1328 from 12.21.2015.

Approved for publication by the decision of the Academic Council of Kharkiv Karazin National University. (Minutes №1 dated January 23, 2017 p.)

Editorial address:

Svobody Sq. 4, 61022, Kharkiv, Ukraine, V.N. Karazin Kharkiv National University, Department of Physics, 057-707-53-83, ruslan.v.vovk@univer.kharkov.ua

All articles reviewed.

Certificate of registration КВ number 21573-11473P on 20.08.2015

Content

Зміст

Вісник ХНУ, серія «Фізика», вип. 25, 2016. с. 6-11

УДК 544.723; 669.788
PACS: 61.44.Br; 81.05.Zx; 81.30.-t

Peculiarities of hydrogen absorption by melt spun amorphous alloys $Nd_{90}Fe_{10}$

V.I. Dubinko, O.M. Bovda, O.E. Dmytrenko, V.M. Borysenko, I.V. Kolodiy

National Science Center "Kharkov Institute of Physics and Technology"
Kharkov 61108, Ukraine

A fierce exothermic reaction was detected in $Nd_{90}Fe_{10}$ films with sufficient degree of amorphous phase upon filling them with hydrogen or deuterium, which resulted in the melting of the samples and the Cu foil, in which the samples have been wrapped. Quantitative analysis have shown that the amount of heat produced in large $Nd_{90}Fe_{10}$ samples in our experiments is 80÷100 kJ per g of hydrogen, which cannot be explained by DSC data on the heat produced in small samples under different heating-cooling balance. Possible reasons for the discrepancy are discussed including low energy nuclear reactions taking place at the initial stage of hydride formation.

Keywords: hydrogen storage, amorphous alloys, exothermic reactions.

При гідруванні швидко загартованих плівок $Nd_{90}Fe_{10}$ з великим ступенем аморфизації виявлена сильна екзотермічна реакція, яка призводить до плавлення зразків і мідної фольги, в якої загорнуті зразки. Аналіз показав, що питома кількість тепла, що виділяється у великих зразках $Nd_{90}Fe_{10}$ в наших експериментах, на порядок перевершує питому кількість тепла, виробленого в невеликих зразках методом диференціальної калориметрії. Обговорюються можливі причини розбіжності, в тому числі, із залученням низькоенергетичних ядерних реакцій, що протікають на початковому етапі формування гідридів.

Ключові слова: зберігання водню, аморфні сплави, екзотермічні реакції.

При гидрировании быстро закаленных пленок $Nd_{90}Fe_{10}$ с большой степенью аморфизации обнаружена сильная экзотермическая реакция, которая приводит к плавлению образцов и медной фольги, в которую завернуты образцы. Анализ показал, что удельное количество тепла, выделяющееся в больших образцах $Nd_{90}Fe_{10}$ в наших экспериментах, на порядок превосходит удельное количество тепла, производимого в небольших образцах методом дифференциальной калориметрии. Обсуждаются возможные причины расхождения, в том числе, с привлечением низкоэнергетических ядерных реакций, протекающих на начальном этапе образования гидридов.

Ключевые слова: хранение водорода, аморфные сплавы, экзотермические реакции.

Introduction

The Nd-Fe alloys are known to readily absorb hydrogen, and this property is especially pronounced for melt spun $Nd_{80}Fe_{20}$ alloys that have amorphous structure and can absorb up to 2.4 wt% of hydrogen [1]. The interaction of hydrogen with amorphous metals has been studied extensively [2]. These studies were motivated by both scientific and technological interests, mainly the potential use of amorphous hydrides in hydrogen storage technology. The use of amorphous alloys as an alternative new energy storage material, however, still contains technical difficulties, in terms of limited hydrogen cycling ability, relatively high activation energy, fragileness of the host material after hydrogenation, which need further examinations.

In this paper, we explore the kinetics and thermodynamics of hydriding of melt spun $Nd_{90}Fe_{10}$ alloys

Fig. 1 Installation "Strychka" for fabrication of metal films with a complicated nonequilibrium structure.

a

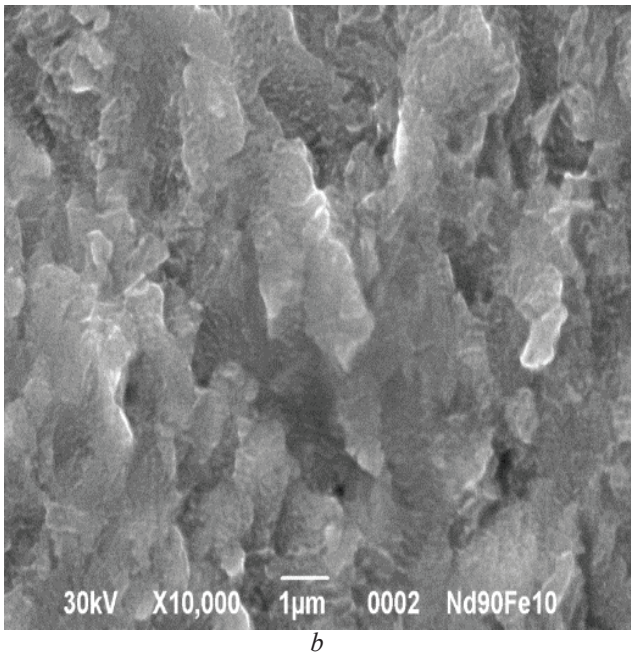

b

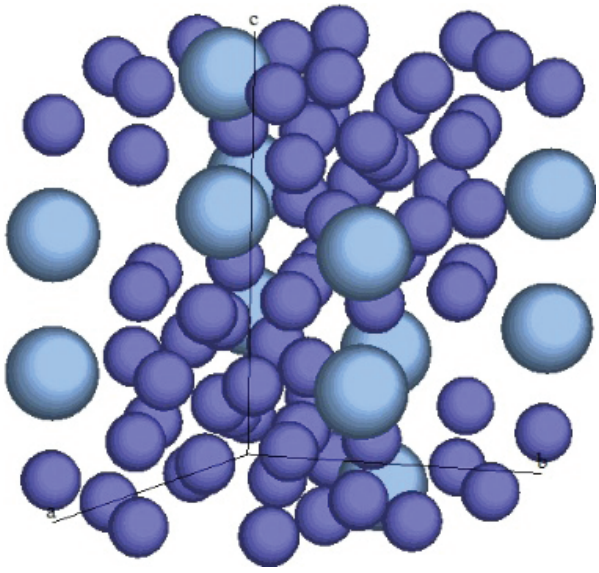

c

Fig. 2 The appearance (a) and surface morphology (b) of the melt spun Nd90Fe10 films. (c) изменить на Fig. 2 The appearance (a), surface morphology (b) and unite cell (c) of the melt spun Nd90Fe10 films.

that have amorphous structure similar to that of $Nd_{80}Fe_{20}$ alloys investigated in [1].

Material fabrication and characterization

The melt spun $Nd_{90}Fe_{10}$ films have been produced in the installation "Strychka" (Fig. 1) by the deposition on a copper wheel rotating with a high speed that provides fast cooling at a rate up to 10^6 K/s. The rotation speed can be varied to obtain a required degree of disorder. The films are several cm in length, several mm in width and ~10 to 30 microns in thickness. Their appearance and surface morphology is shown in Fig. 2. One can see that the film surface is extremely rough containing a lot of micron size caverns, which is a common property of this type of materials.

The microstructure of the films consists of a combination between two crystalline phases Nd-α (low temperature hcp phase, T<683°C) and Nd-β (high temperature bcc phase) and amorphous phase Nd_2Fe_{17}, which is shown in Fig. 2c.

The unite cell of amorphous phase Nd_2Fe_{17} entering the initial microstructure of $Nd_{90}Fe_{10}$.

The lattice parameters of the crystalline phases and their relative fraction in respect to the amorphous phase changes slowly with time and is substantially different for the films produced in 2016, 2010 and 2008, as can be seen from the table 1.

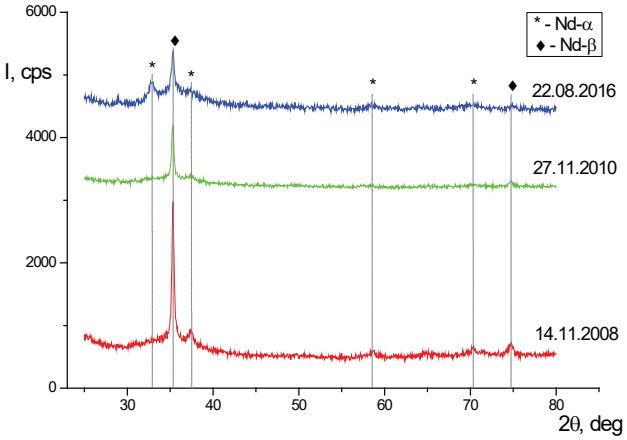

Fig. 3 Diffractograms of three films produced in different years, where the height of the diffraction peak corresponds to the crystalline fraction in a sample X_c = 11% (blue curve); 19% (green curve) and 47% (red curve).

Fig.3 shows X-ray diffractograms of three different films, where the height of the diffraction peak corresponds to the crystalline fraction in a sample. Let the integral intensity of diffraction lines of a crystalline phase be A_c, and the integral intensity of 'disordered' phase be A_d. Then the relative fraction of crystalline phase can be expressed as X_c:

$$X_c = \frac{A_c}{A_c + A_d} 100\%, \qquad (1)$$

Table 1

Relative fraction and lattice parameters of crystalline phase in $Nd_{90}Fe_{10}$ films produced in different years and measured in 2016.

Production year	**Phase**	$X_c = \frac{A_c}{A_c + A_d} 100\%$	**Lattice parameters**, Å
2008	Nd-α	47	a = 3,659; c = 11,784
	Nd-β		a = 4,171
2010	Nd-α	19	a = 3,656; c = 11,804
	Nd-β		a = 4,170
2016	Nd-α	11	a = 3,658; c = 11,801
	Nd-β		a = 4,171

The samples in Fig. 3 correspond to X_c = 11%; 19% and 47%, respectively, and in the following section, we describe the response of samples to a slow heating in the hydrogen atmosphere.

Kinetics and thermodynamics of the hydrogen absorption by the samples

Hydrogenation of samples with X_c = 11% and X_c = 19% was done under hydrogen pressure ranging from 0.2 to 3.4 bar and temperature increased gradually by electric heater. Active hydrogen absorption usually started slightly below or above 300 °C, and its rate and character depended on the hydrogen pressure. Above ~ 1 bar, hydrogenation was accompanied by a substantial heating of the samples, which resulted in the sample melting. An extreme example for the initial pressure of 3.4 bar is shown in Fig. 4. One can see an instant drop of pressure accompanied by a fierce exothermic reaction resulting in a sample heating spike. Duration of the heating spike was about 40 seconds, while the maximum *registered* temperature was 570 °C, which appears to be an underestimate.

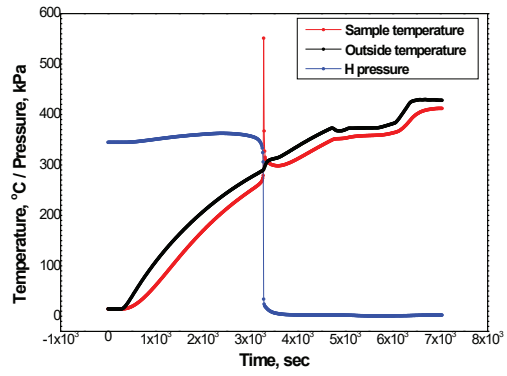

Fig. 4 $Nd_{90}Fe_{10}$ films with X_c = 11% of a mass 2.3713 g wrapped in a Cu foil of a mass 1.6225 gram. The loading ratio measured by the H pressure drop after hydrogenation was ~1.6 H per metal atom (~1.36 wt% H). 'Outside temperature' is measured at 2 mm distance from the external ceramic wall of the reactor.

Examination of the resulting appearance of the NdFe alloy, which has been wrapped in a Cu foil before the testing (Fig. 5.), shows that the alloy and the Cu foil have *melted together* around the thermocouple, which indicates that the maximum temperature was higher than 1000 °C, since the meting temperature of $Nd_{90}Fe_{10}$ is 685 °C and the meting temperature of Cu is 1085 °C.

XRD analysis of the hydrogenated material has shown that all the amorphous phase has transformed into two crystalline hydride phases, fcc NdH_2 and hcp $Nd_2Fe_{17}H_{4.6}$ shown in Fig. 6.

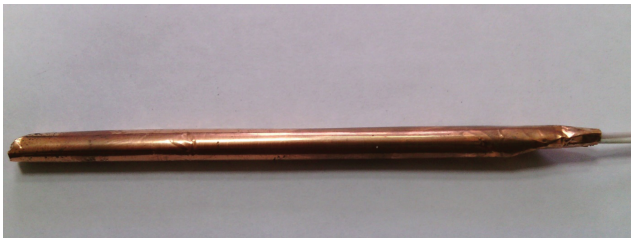

a

b

Fig. 5 $Nd_{90}Fe_{10}$ films with X_c = 11% of a mass 2.3713 g wrapped in a Cu foil of a mass 1.6225 gram before (a) and after (b) hydrogenation at a rate shown in Fig. 4.

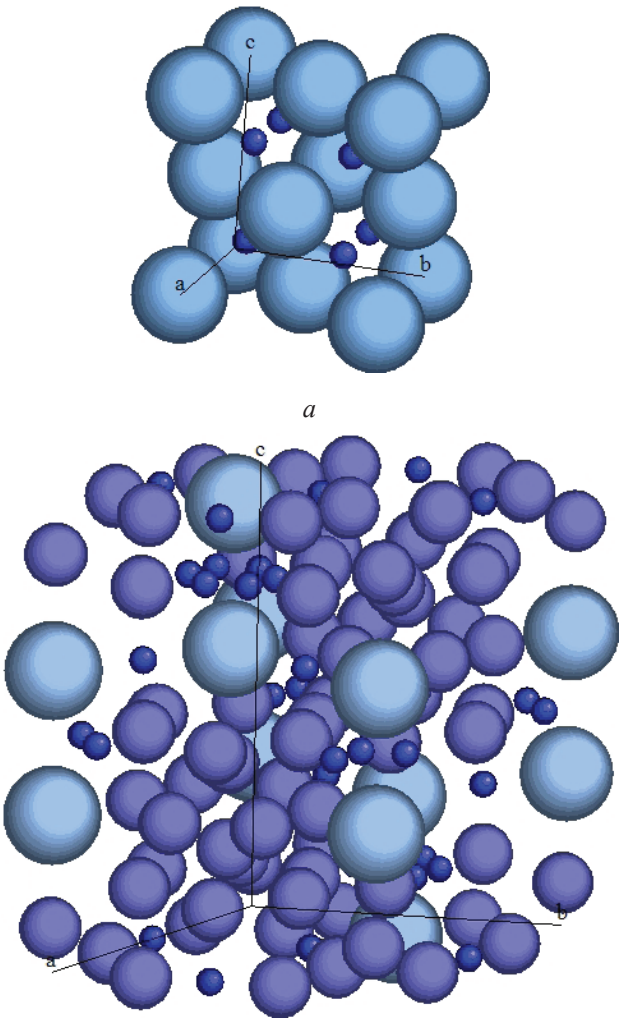

a

b

Fig. 6 Unite cells of fcc NdH2 (left) and hcp Nd2Fe17H4.6 (right) phases. NdH2 is a dominating phase containing a majority of absorbed hydrogen. изменить на Fig. 6 Unite cells of fcc NdH2 (a) and hcp Nd2Fe17H4.6 (b) phases. NdH2 is a dominating phase containing a majority of absorbed hydrogen.

The amount of heat produced by hydrogenation

The energy required for heating the $Nd_{90}Fe_{10}$ films and Cu foil from 270 to 1100 °C and for melting the Cu foil is given by

$$\Delta Q_{NdFe+Cu}(\Delta T) = C_{NdFe} m_{NdFe} \Delta T + C_{Cu} m_{Cu} \Delta T + Q_{Cu}^{melt} m_{Cu} = 1263 \text{ J},$$

$$\Delta T = 830 \text{ K}, \qquad (2)$$

where $m_{NdFe} = 2.3713$ g, $m_{Cu} = 1.6225$ g and $C_{NdFe} = 0.214 \frac{J}{g \cdot K}$, $C_{Cu} = 0.385 \frac{J}{g \cdot K}$ are the masses and the heat capacities of NdFe films and Cu foils, respectively, $Q_{Cu}^{melt} = 207$ J/g is the latent heat of melting of Cu.

The energy required to heat the walls of ceramic (Al_2O_3) chamber tube around the samples from 295 to 308 °C is given by

$$\Delta Q_{Al_2O_3}(\Delta T) = C_{Al_2O_3} m_{Al_2O_3} \Delta T = 1322 \text{ J},$$

$$\Delta T = 13 \text{ K}, \qquad (3)$$

where $m_{Al_2O_3} = 93.5$ g and $C_{Al_2O_3} = 1105 J/(g \cdot K)$ are the mass and the heat capacity of the Al_2O_3 tube surrounding the samples (the tube inner diameter 10 mm, outer diameter 20 mm, the sample length 100 mm).

So the *minimum* amount of heat produced by the observed reaction (*without account of the heat dissipation*) can be estimated as **2585 J** given by the sum:

$$\Delta Q_{tot} = \Delta Q_{NdFe+Cu}(830 \text{ K}) + \Delta Q_{Al_2O_3}(13 \text{ K}) = 1263 \text{ J} + 1322 \text{ J} = 2585 \text{ J}, \qquad (4)$$

Dividing this heat by the amount of absorbed hydrogen that caused the reaction, 0.031 g, one obtains a specific heat of hydrogen absorption as

$$Q_H = 2585 \text{ J}/0.032 \text{ g} = 80170 \text{ J/g}, \qquad (5)$$

which will be compared with a direct DSC measurements in the following section.

Differential scanning calorimetry of $Nd_{90}Fe_{10}$

Differential scanning calorimetry (DSC) is a thermoanalytical technique in which the difference in the amount of heat required to increase the temperature of a sample and reference is measured as a function of temperature. The temperature program for a DSC analysis is designed such that the sample holder temperature increases linearly as a function of time.

Fig. 7 shows the results of heating the small $Nd_{90}Fe_{10}$ samples (11.9 and 18.8 mg) in the pure Ar atmosphere (red curves) and in the mixed atmosphere of H and He (blue curves). In the first case, the lower red curve shows zero weight gain, which means that Ar is not absorbed by the sample, as expected. The upper red curve shows one small exothermic peak at 510 °C and a larger endothermic peak at 676 °C. The former corresponds to the crystallization of amorphous phase of $Nd_{90}Fe_{10}$, while the latter corresponds to the melting of $Nd_{90}Fe_{10}$ alloy.

The lower blue curve shows the weight % increase of the sample due to the H absorption, which amounts to ~1wt% at the temperature of the first exothermic peak on the upper blue curve (14.78 J/g) and to 5.52 wt% at the temperature of the second and much more powerful exothermic peak (438.6 J/g). From these data, one can evaluate the amount of heat released in the first and in the

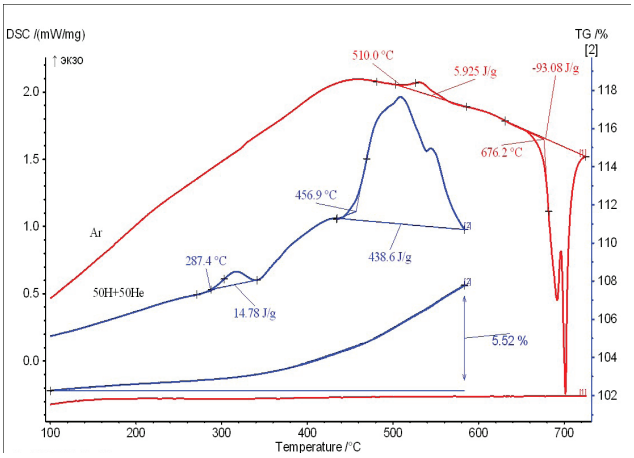

Fig. 7 DSC of $Nd_{90}Fe_{10}$ samples in the Ar (11.9 mg; heating rate 20 K/min - red curves) and H/He atmosphere (18.8 mg; heating rate 10 K/min - blue curves).

second reaction *per gram of absorbed hydrogen*: $Q_1 = 1500$ J/g and $Q_2 = 9800$ J/ g.

Thus, a specific heat of hydrogen absorption in a DCS experiment is given by $Q_1 + Q_2 = 11300$ J/g, which is almost an order of magnitude less than 80170 J/g estimated in our hydrogenation experiments. It means that the underlying reactions taking place in our experiments should be different from those taking place in a DSC installation.

Deuterium absorption by $Nd_{90}Fe_{10}$ mixed with Cu powder

In this experimental setup, we used deuterium atmosphere and attempted to prolong the deuterium absorption stage and avoid melting of the samples by mixing a powder produced from $Nd_{90}Fe_{10}$ with Cu powder and packing the mixture in a Cu tube. In this way, deuterium access to $Nd_{90}Fe_{10}$ was delayed, and the heat produced under hydrogenation in 1.722 g of $Nd_{90}Fe_{10}$ was distributed over all the material of the mixture and the tube with a total mass of 14. 372 g. As a result, the sample temperature T_S did not exceed the furnace temperature T_F by more than 5 °C even during the most active deuterium absorption stage that lasted 40 min (Fig. 8), and the overall time when $T_S > T_F$ was about 15 min. Taking into account the heat balance, one can estimate the total produced heat as 2190 J and the specific heat of hydrogen absorption as 102100 J/g, which is close to our estimate 80170 J/g of the specific heat produced under hydrogenation of pure $Nd_{90}Fe_{10}$ samples.

Discussion

Specific heat produced per one gram of absorbed hydrogen or deuterium in our reactor conditions seems to be much higher than that in DSC installation, which means that the underlying reactions should be different. We have tested samples with a mass in the gram range, while DSC samples were ~ 10 mg, which could imply different heating-cooling balance affecting the reaction route.

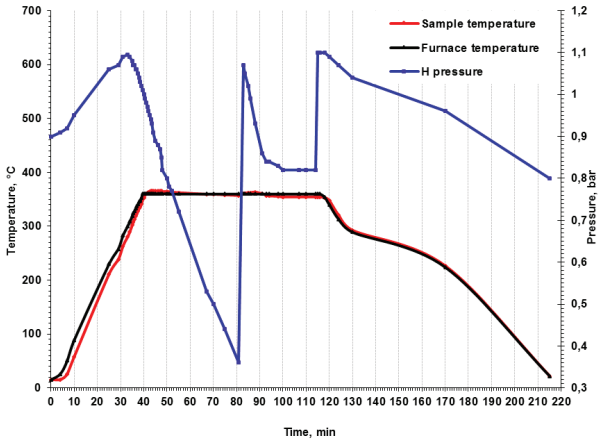

Fig. 8 $Nd_{90}Fe_{10}$ powder with $X_c = 11\%$ of a mass 1.7222 g mixed with Cu powder of a mass 2.2526 g, wrapped in a Cu foil of a mass 0.43955 g and packed in a Cu tube of a mass 9.565 g. The loading ratio measured by the weight gain after D absorption was ~1.1 H per metal atom (~1.834 wt% D).

One of the possible reasons for abnormal heat production is known to be the low energy nuclear reactions (LENR) that take place in heavily deuterated palladium [3] or hydrogenated nickel [4] under nonequilibrium conditions. These reactions can be triggered by localized anharmonic vibrations (LAVs) created at sufficiently high temperatures at special places of the disordered lattice [5-9]. Another driving mechanism of the LAV creation is irradiation that can displace atoms from equilibrium positions far enough to induce anharmonic vibration mode [10]. In view of that, it is desirable to fill the alloys with hydrogen or deuterium or the H-D mixture directly under irradiation and to measure their response to such combined treatment.

Conclusions and outlook

A fierce exothermic reaction was detected in $Nd_{90}Fe_{10}$ films with sufficient degree of amorphous phase upon filling them with hydrogen or deuterium, which resulted in the melting of the samples and the Cu foil, in which the samples have been wrapped.

Quantitative analysis have shown that the amount of heat produced in $Nd_{90}Fe_{10}$ samples in our experiments cannot be explained by DSC data on the heat produced in small samples.

One of the possible explanations of this discrepancy is based LENR taking place *at the initial stage of hydride formation*, when 80÷90% of amorphous phase in the films produced LAVs [5-10] that triggered LENR. Subsequently, the amorphous phase transforms to crystalline hydrides where the LAVs do not form, which stops the LENR. Upon cooling, various hydride phases are observed by X ray analysis: NdH_2 (fcc) and $Nd_2Fe_{17}H_{4.8}$ (hcp).

In order to initiate LENR, it is desirable to make the

hydrogenation directly under irradiation and to measure the response to such combined treatment. This problem needs further investigations.

The Nd-Fe structure explored in the present study may be not the only one that could provide the necessary conditions for the LAV induced LENR. In spite of a huge body of investigations of materials connected to the hydrogen storage problem, they have not been focused on the investigation of the *energy production* under hydrogenation. In the cases when abnormally large enthalpies of hydride formation have been reported, the samples have been destroyed by the reaction, similar to case under investigation in this report. There is a need to re-investigate some of these materials with a due control of the heat production under hydrogenation and external triggering.

Among the promising candidates to be investigated are the Ti-Zr-Ni melt-spun alloys that can take various structures ranging from amorphous to quasi-crystalline, Laves phase, etc., which can store large amounts of hydrogen and provide the necessary conditions for the LAV excitation in the hydrogen subsystem.

References

1. Yи.P. Bobrov, O.M. Bovda, O.E. Dmytrenko, Research of interaction of hydrogen with the melt-spun Nd80Fe20 alloy, VANT #6/18 (2009) 245-247.
2. N. Eliaz, D. Eliezer, An overview of hydrogen interaction with amorphous alloys, Advanced Performance Materials 6 (1999) 5-31.
3. M. Fleischmann, S. Pons, M. Hawkins, Electrochemically induced nuclear fusion of deuterium. J. Electroanal. Chem. 261 (1989) 301-308 and errata in Vol. 263, 187-188.
4. Пархомов А.Г. Никель-водородные реакторы, созданные после публикации отчета об эксперименте в Лугано. Журнал Формирующихся Направлений Науки, 4(11) (2016) 58–62.
5. V.I. Dubinko, P.A. Selyshchev and F.R. Archilla, Reaction-rate theory with account of the crystal anharmonicity, Phys. Rev. E 83 (2011), 041124-1-13.
6. V.I. Dubinko, Low-energy Nuclear Reactions Driven by Discrete Breathers, J. Condensed Matter Nucl. Sci., 14, (2014) 87-107.
7. V.I. Dubinko, Quantum tunneling in gap discrete breathers, Letters on Materials, 5 (2015) 97-104.
8. V.I. Dubinko, Quantum Tunneling in Breather 'Nano-colliders', J. Condensed Matter Nucl. Sci., 19, (2016) 1-12.
9. V. I. Dubinko, D. V. Laptev, Chemical and nuclear catalysis driven by localized anharmonic vibrations, Letters on Materials 6 (2016) 16–21.
10. V. I. Dubinko, Radiation-induced catalysis of low energy nuclear reactions in solids, J. Micromechanics and Molecular Physics, 1 (2016) 165006 -1-12.

Вісник ХНУ, серія «Фізика», вип. 25, 2016. с. 12-15

УДК 538.945:539.214
PACS: 83.50. – v Deformation and flow of metals
83.60. Wc Instability of flow

The influence of electrical current pulses on the plastic deformation of copper

O.S. Mazitov, S.V. Lebediev

V.N. Karazin Kharkov National University
Svoboda square, 4, Kharkov, Ukraine, 61022

The paper studied the influence of electrical current pulses with density of 300 – 900 A/mm^2 and duration of $4\cdot10^{-4}$ s on the plastic deformation of the technically pure copper. The deformation curves under and without the influence of current pulses during the deformation of specimen were obtained. The comparison of obtained curves was carried out. It was determined that the passing of electrical current pulses during the deformation of copper leads to the resource of plasticity growing.
Keywords: electroplastic effect, plastic deformation, electrical current pulses.

В роботі вивчено вплив імпульсів електричного струму густиною 300 – 900 А/мм^2 та тривалістю $4\cdot10^{-4}$ с на пластичну деформацію технічно чистої міді. Були отримані деформаційні криві при впливі та без впливу імпульсів струму в процесі деформації зразка. Було виконано порівняння отриманих кривих. Встановлено, що проходження імпульсів електричного струму при деформації міді приводить до зростання ресурсу пластичності.
Ключові слова: електропластичний ефект, пластична деформація, імпульси електричного струму.

В работе изучено влияние импульсов электрического тока плотностью 300 – 900 А/мм^2 и длительностью $4\cdot10^{-4}$ с на пластическую деформацию технически чистой меди. Были получены деформационные кривые при воздействии и без воздействия импульсов тока в процессе деформации образца. Было выполнено сравнение полученных кривых. Установлено, что прохождение импульсов электрического тока при деформации меди приводит к возрастанию ресурса пластичности.
Ключевые слова: электропластический эффект, пластическая деформация, импульсы электрического тока.

Introduction

It is known that lattice defects and deformation conditions (such as strain rate and temperature) influence on the mechanical properties of metal. But also the influence of phonons and electrons of conductivity on dislocations motion exists. It is possible to affect on the crystal by the flux of high-energy electrons in the electric current pulse [1, 2]. The phenomenon of sharp reduction of resistance to deformation of the metal and growing of plasticity by passing of current pulses is called the electroplastic effect. It is stated that the critical value of the electric current density exists and above that value the picture of deformation changes qualitatively and it cannot be explained only by influence of temperature and (or) magnetic field. When the direction of the drift velocity of electrons is along the direction of external force there is the maximum effect [3].

There is a big amount of experimental results at this time which demonstrate the influence of the electrical current pulses with large densities on the plastic flow of pure metals and alloys [4]. In available works it was found that the electroplastic effect is observed when the drift velocity of electrons is higher than velocity of dislocations motion. However, issues that deal with a lattice heating and controlling the phenomenon on the microscopic level remain outstanding.

In this context, it might be useful to study this phenomenon at higher densities of electric current considering the Joule's heating and other related exposures on the deformable specimen. It will allow to separate the influence of thermal and athermal processes on the deallocation of dislocations from stoppers and their displacement in the crystal lattice [5].

Object and methodology of the experiment

To carry out the tasks assigned in the work copper specimens were used. Impact on the object was carried out by the external load, temperature, electrical current pulses. Tests were carried out by the universal testing machine, which had the next technical characteristics:

- creating loads on the specimen up to $2\cdot10^3$ N with ultimate sensitivity of 10^{-2} N;
- registration of elongation during active loading with sensitivity of $5\cdot10^{-6}$ and relative deformation of $5\cdot10^{-2}$ %;

- strain rate range of $10^{-6} – 10^{-2}$ s^{-1}.

For research a roll of technically pure copper wire with diameter of 0,8 mm was made in factory. While the preparation the wire was cut into segments with length of 50 mm and in order to reduce the number of defects in the specimens created by rolling the annealing with temperature of 450°C and vacuum of 10^{-2} mm was made.

Electric current pulses generator which created single and multiple pulses with current up to 1 kA, duration of ~10^{-5} – 10^{-4} s and voltage of 65 - 400 V was used in experiment. Discharger with frequency of 400 – 1250 Hz also was used in the work. To make experiments with annealed lattice defects during passing of pulses we need to have a big drifting velocities of electrons with density of $10^3 – 10^4$ A/mm^2 and duration of 10^{-4}– 10^{-6} s.

Electric scheme consists of the next elements: 1 – control block; 2, 3 – thyristors; 4 – inductor; 5 – specimen; 6 – capacitor bank; 7 – voltmeter; 8 – standart resistance of 1 mOhm; 9 – oscilloscope; 10 – load resistor; 11 – capacitor bank of 20 mF; 12 – 220 V supply; 13 – transformer; 14 – diode bridge.

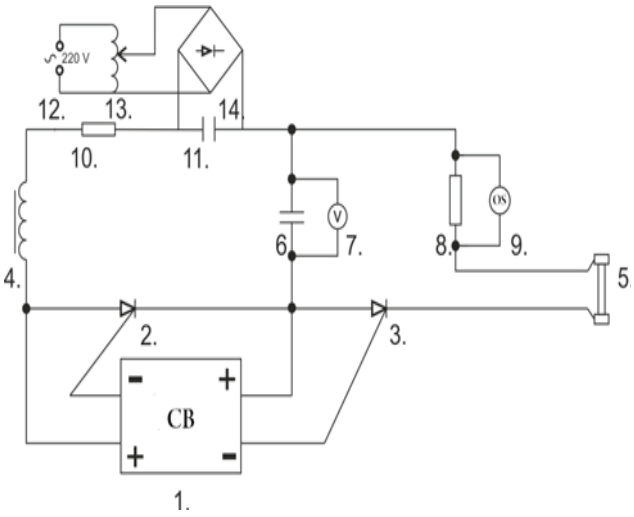

Fig.1. Electric scheme of the pulse machine.

Relation of current and duration that is shown on fig.2 is regulated by changing the voltage on supply. Calibration of pulses by amplitude and duration is carried out by Rigol DS1052D oscilloscope. In addition, the graphic image of electric current pulse was carried out (fig.3).

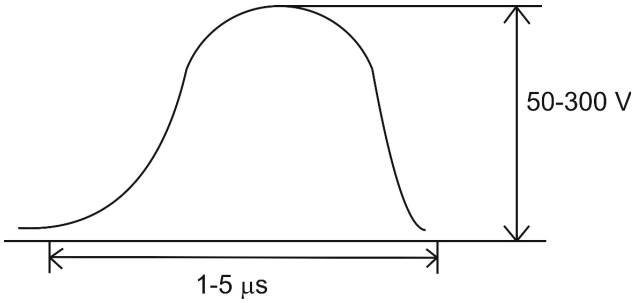

Fig.2. Single pulse curve in voltage – tome coordinates.

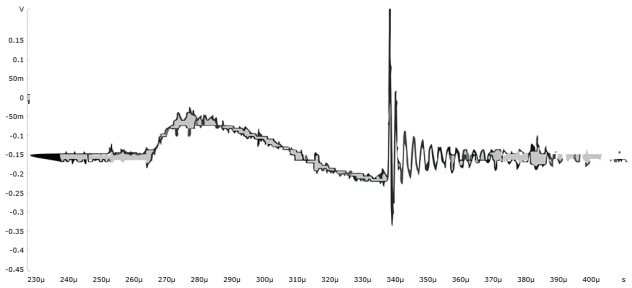

Fig.3. The scan of the electric current pulse in time.

Main scheme characteristics: current of (0,1 - 10)·10^3 A; working voltage of 60 – 450 V; pulse duration of (1,4 - 18)·10^{-5} s; bell-shaped pulse; steepness of the front and slope are 4·10^6 and 2·10^5 kA/s respectively; the smallest duty cycle in automatic turning on mode is of 1 s.

Results and discussion

To define the influence of electric current pulses on deformation characteristics of metal the loading curves in coordinates load P – time t, obtained without (j=0) and with the electric current pulses (j≠0), were compared (fig.4).

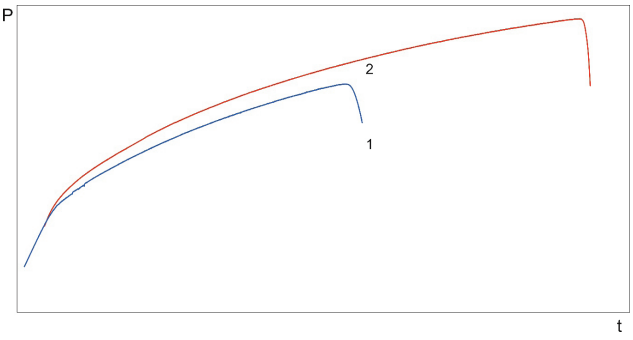

Fig.4. The load – time diagram in the area of elastic and plastic loading of copper specimens with diameter of 0,8 mm without (1) and with (2) electric current pulses.

The initial area of P(t) curve of the polycrystalline copper (99,5 %) without electric pulse exposure (dependence 1) allows to define: the effective elastic modulus in the specimen – moving rod of loading machine system (<E>), yield stress (σ_0), strain hardening coefficient ($\theta=d\sigma/d\varepsilon$). The electric current pulses exposure on the

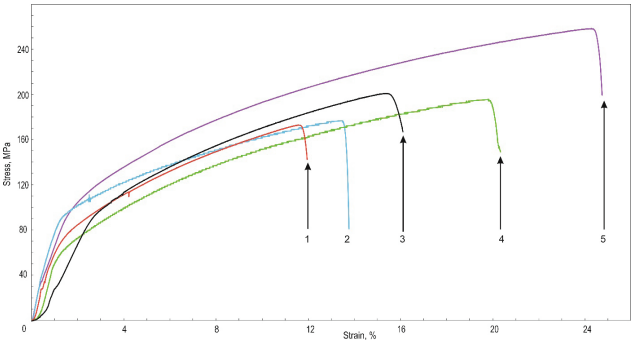

Fig.5. Deformation curves under different values of densities of electric current (1 – 0 A/mm^2, 2 – 291 A/mm^2, 3 – 500 A/mm^2, 4 – 708 A/mm^2, 5 – 916 A/mm^2).

elastic and plastic area of loading curve is shown on fig.4 (dependence 2).

It is already known that there is no clear explanation how electric current pulses influence on plastic deformation of metals and alloys.

Examples of the influence of electric current pulses in continuous mode on deformation curve character of polycrystalline copper specimens are shown on fig.5. As can be seen, electric current pulses of different density influence on deformation curve character in different ways.

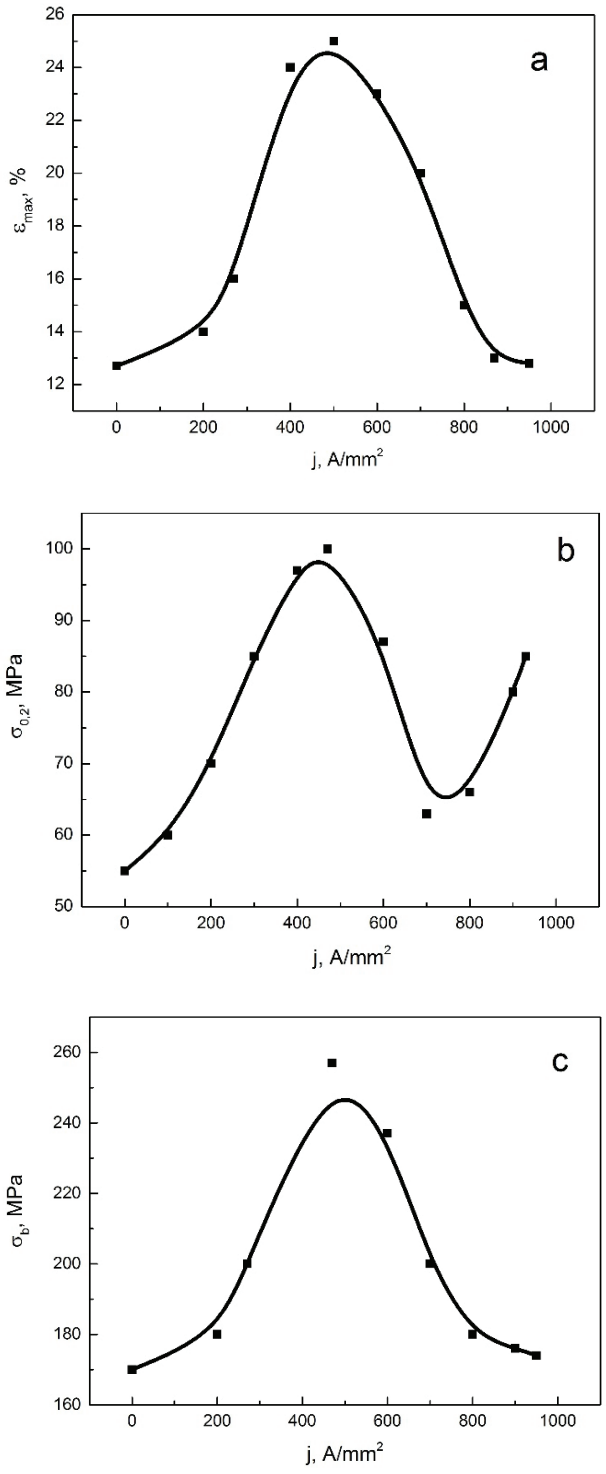

Fig.6. The dependencies of strengthening characteristics on electric current density, a – plasticity resource, b – conditional yield stress, c – ultimate tensile strength.

Let us consider the influence of electric current density on mechanical characteristics of copper. Dependencies $\varepsilon_{max}(j)$, $\sigma_{0,2}(j)$, $\sigma_b(j)$ are shown on fig.6 respectively, where ε_{max} – plasticity resource, $\sigma_{0,2}$ – conditional yield stress, σ_b – ultimate tensile strength.

As can be seen from these three figures, ultimate tensile strength, plasticity resource and conditional yield stress are increasing non-monotonously and the maximum is observed at j = 500 A/mm^2. It is also noteworthy that plasticity resource and ultimate tensile strength at 900 A/mm^2 are approximately equal to the value when there is no exposure of electric current pulses whereas conditional yield stress with current density higher than 700 A/mm^2 increases rapidly.

It can be seen from graphics that with current density up to 500 A/mm^2 both ultimate tensile strength and plasticity resource increase which is abnormally. This effect, supposedly, occurs in the result of exposure of electric current pulse that influence on dynamics of the dislocations motion. Probably, that with passing of electric current pulse the velocity of dislocations motion increases, whereas with its absence velocity decreases and dislocations are starting to concentrate in the specimen. Thus, the specimen becomes stronger.

In addition, the role of adiabatic heating was considered. Let us evaluate the temperature increase of the copper specimen with unit volume from the relation:

$$\Delta T = (\rho \cdot \langle\tau\rangle \cdot c_p^{-1} \cdot D^{-1}) \cdot \langle j\rangle^2, \qquad (1)$$

where specific electrical resistance $\rho = 1{,}73 \cdot 10^{-8}$ Ohm·m (without temperature dependence); duration of pulse at the level of 0,7·j is $\langle\tau\rangle = 10^{-2}$ s; specific heat capacity $c_p = 3{,}85 \cdot 10^2$ J·kg^{-1}·K^{-1} (without temperature dependence); density $D = 8{,}93 \cdot 10^3$ kg·m^{-3}. Then, for current density values of (291 and 916) $\cdot 10^6$ A/m^2 temperature increase ΔT will be 2,1 and 20,6 K respectively.

While electric current pulses are passing through, some of the electrons interact with atoms of crystal lattice causing the latter to oscillate with frequencies higher than phonons have. Such oscillations are called breathers [6]. When the flux of electrons passes through the crystal lattice, the latter starts to shake. Therefore, dislocations continue their motion and do not accumulate near the stoppers. In the result of dislocations motion the plasticity of specimen grows, that can be seen on fig.4 (a). After definite moment (j = 500 A/mm^2) the plasticity starts to decrease. This is explained by the strengthening of specimen at high densities of dislocations.

Conclusions

1. The influence of electric current pulses on plastic deformation of the technically pure copper with temperature

of 300 K is shown.
2. It was stated that with determined density (j=500 A/mm^2) the maximum value of plasticity resource and ultimate tensile strength is observed.
3. It was found out that values of strengthening characteristics with current of 900 A/mm^2 approximately coincide with the values when there are no electric current pulses.

References

1. O.A. Troitskiy. Technical physics letters 10, 18 (1969).
2. A.F. Sprecher, S.L. Mannan, H.Conrad. Acta Metall. 34, 7, 1145 (1986).
3. V.I. Spitsin, O.A. Troitskiy elektroplasticheskaya deformatsiya metallov – Moskva: Nauka, 1985. – 160 p. – In Russian.
4. O.A. Troitskiy, Yu.V. Baranov, Yu.S. Avramov, A.D. Shlyapin. Fizicheskie osnovyi i tehnika obrabotki sovremennyih materialov. M.- I., (2004). 590 s.
5. V.P. Lebedev, S.V. Savich. Vestnik HNU. Seriya: Fizika 962, v.15, 88 (2011).
6. Dubinko V.I. Reaction – rate theory with of the crystal anharmonicity / V.I. Dubinko, P.A. Selyshchev, J.F.R. Archilla // Physical Review E. – 2011. – Vol. 83, № 041. – P. 124 – 137.

Вісник ХНУ, серія «Фізика», вип. 25, 2016. с. 16-25

PACS numbers: 73.20.–r, 73.25.+i, 73.50.–h, 73.61.–r

Towards to the theory of magnetoplasma waves on the semiconductor nanotube surface

G.I. Rashba

Kharkiv National University named after V.N. Karazin
Sq. Svobody 4, Kharkiv, 61022, Ukraine
E-mail: georgiy.i.rashba@gmail.com

The effective mass approximation is used to consider plasma and magnetoplasma waves in electron system on the surface of the cylindrical semiconductor nanotube. The electron-electron interaction is taken into account within the framework of the random phase approximation. In the case of degenerate electron gas the spectral windows on the wavevector-frequency plane and the spectra of the waves are obtained. Their frequencies undergo quantum oscillations of the de Haas-van Alfven type which are attributed to the Fermi level traversing the sub-zone boundaries in the electron energy spectrum. The spectrum and the damping of waves in the non-degenerate electron gas were found. In a magnetic field parallel to the cylinder axis the frequencies of the magnetoplasma waves undergoes the Aharonov-Bohm type oscillations appearing with changing magnetic field strength.

Keywords: magnetoplasma waves, semiconductor nanotube, random phase approximation, spectral windows, spectrum and the damping of waves, de Haas-van Alfven type oscillation, Aharonov-Bohm type oscillation.

У наближенні ефективної маси розглядаються плазмові і магнітоплазмові хвилі у системі електронів на поверхні циліндричної напівпровідникової нанотрубки. Електрон-електронна взаємодію враховується у наближенні хаотичних фаз. У випадку виродженого електронного газу знайдені положення вікон прозорості для хвиль на площині хвильовий вектор-частота та спектри цих хвиль. Їх частоти випробовують квантові осциляції типу де Гааза-ван Альфена, обумовлені перетином границь підзон у спектрі енергії електронів рівнем Фермі. Знайдено спектр і згасання хвиль у невиродженому електронному газі. У магнітному полі, паралельному осі циліндра, частоти магнітоплазмових хвиль випробовують осциляції типу Ааронова-Бома зі зміною напруженості магнітного поля.

Ключові слова: магнітоплазмові хвилі, напівпровідникова нанотрубка, наближення хаотичних фаз, вікна прозорості, спектр і згасання хвиль, осциляції типу де Гааза-ван Альфена, осциляції типу Ааронова-Бома.

В приближении эффективной массы рассматриваются плазменные и магнитоплазменные волны в системе электронов на поверхности цилиндрической полупроводниковой нанотрубки. Электрон-электронное взаимодействие учитывается в приближении хаотических фаз. В случае вырожденного электронного газа найдены положения окон прозрачности для волн на плоскости волновой вектор-частота и спектры волн. Их частоты испытывают квантовые осцилляции типа де Гааза-ван Альфена, обусловленные пересечением границ подзон в спектре энергии электронов уровнем Ферми. Найдены спектр и затухание волн в невырожденном электронном газе. В магнитном поле, параллельном оси цилиндра, частоты магнитоплазменных волн испытывают осцилляции типа Ааронова-Бома с изменением напряженности магнитного поля.

Ключевые слова: магнитоплазменные волны, полупроводниковая нанотрубка, приближение хаотических фаз, окна прозрачности, спектр и затухание волн, осцилляции типа де Гааза-ван Альфена, осцилляции типа Ааронова-Бома.

Introduction

A keen interest of researchers in electron nanosystems on curving surfaces [1,2] is attributed to a number of reasons. These systems are functional elements of many devices and engineering gadgets. The perfection of experimental setup allows for production of these systems in a laboratory framework. For theorists these systems are convenient objects for field-testing of novel methods of computations of physical values. The curvature of the structure and external magnetic field enrich the picture of phenomena occurring in nanostructures. The control methods of their properties become more diverse.

Various effects have been found on curving surfaces in such electron systems, which cannot be reproduced in those of the plane geometry. Among them are the effects of hybridization of the spatial and magnetic quantization of electron motion, the modification of the hamiltonian of the electron system [2,3], the unusual performance of conductance [4] and magnetic response of the system [5], the peculiarities of the screening of electron-electron interaction [6], the specific resonances in electron scattering produced in carbon nanotubes [7] and quantum wires [8] by impurity atoms, etc.

The typical examples of the curving surface nanosystems are carbon and semiconductor nanotubes [1-7]. The electron energy spectrum in these systems is zoned.

It allows due to a small number of electrons near the zone bottom for use of the effective mass approximation. This approximation enables to describe qualitatively, and often quantitatively, the properties of this kind of systems.

Plasma oscillations of the electron gas density on the curving surface were investigated in Ref. [9]. However, the dispersion relationships of the spectrum and damping of plasmons are not given therein [9]. The present paper considers plasma and magnetoplasma waves on the surface of a cylindrical nanotube. We employ the effective mass approximation with the electron-electron interaction being considered in the random phase approximation. We consider the spectrum of density oscillations of degenerate electron gas in Section I and of the non-degenerate gas in Section II. The magnetoplasma waves on cylindrical surface in the longitudinal magnetic field are considered in Section III.

Degenerate electron gas

In the effective mass approximation the wave function of stationary electron state on the surface of cylindrical nanotube has the following form:

$$\psi_{mk}\left(\varphi,z\right)=\frac{1}{\sqrt{2\pi}}\mathrm{e}^{\mathrm{i}m\varphi}\,\frac{1}{\sqrt{L}}\mathrm{e}^{\mathrm{i}kz}\,, \tag{1}$$

where $m=0,\pm1,...$ is the azimuthal quantum number, k is the projection of electron wave vector to the cylinder axis z, φ is the polar angle, L is the length of the tube. The electron energy in the state (1) is:

$$\varepsilon_{mk}=\varepsilon_0 m^2+\frac{k^2}{2m_*}\,. \tag{2}$$

Here m_* is the effective electron mass, $\varepsilon_0=1\big/2m_*a^2$ is the rotational quantum, a is the tube radius. Herein the quantum constant is assumed to be equal to unity.

The spectrum (2) consists of many one-dimensional subzones. The electron state density

$$\nu\left(\varepsilon\right)=\frac{\sqrt{2m_*}L}{\pi}\sum_m\frac{1}{\sqrt{\varepsilon-\varepsilon_0 m^2}} \tag{3}$$

has the square root singularities at the subzone boundaries $\varepsilon_m=\varepsilon_0 m^2$. In this formula the summation is done over those values of m for which the expression under the root is positive. By calculating the sum according to the Poisson formula, we obtain:

$$\nu\left(\varepsilon\right)=2m_*aL\left[1+2\sum_{l=1}^{\infty}\mathrm{J}_0\left(2\pi l\sqrt{\frac{\varepsilon}{\varepsilon_0}}\right)\right],$$

where J_0 is the Bessel function. In the limit $\varepsilon>>\varepsilon_0$, we have

$$\nu\left(\varepsilon\right)=2m_*aL\left[1+\frac{2}{\pi}\left(\frac{\varepsilon_0}{\varepsilon}\right)^{1/4}\sum_{l=1}^{\infty}\frac{1}{\sqrt{l}}\cos\left(2\pi l\sqrt{\frac{\varepsilon}{\varepsilon_0}}-\frac{\pi}{4}\right)\right].$$

The density of states oscillates with varying $\sqrt{\varepsilon}$ with the period $\left(\sqrt{2m_*}a\right)^{-1}$. The monotonous term $2m_*aL$ is equal to the density of states of the two-dimensional electron gas on the area $S=2\pi aL$.

In the random phase approximation, the dispersion equation for the spectrum of plasma waves on the surface of the nanotube has the form [6]:

$$1-\frac{\upsilon_m\left(q\right)}{2\pi L}P_m\left(q,\omega\right)=0\,, \tag{4}$$

where

$$\upsilon_m\left(q\right)=4\pi\overline{e}^2\mathrm{I}_m\left(a\left|q\right|\right)\mathrm{K}_m\left(a\left|q\right|\right) \tag{5}$$

is the cylindrical harmonic of the electron Coulomb interaction energy, $\overline{e}$ is the electron charge divided by the background dielectric constant, I_m and K_m are the modified Bessel functions [10], P_m is the delayed polarization operator which

depends on the projection q of the wave vector to the axis z and frequency ω. With the aim to consider further the magnetoplasma waves, we shall derive the value of P_m for the electron gas in the magnetic field B, which is parallel to the cylinder axis:

$$P_m(q,\omega)=\sum_{m'k\sigma}\frac{f\left(\varepsilon_{(m'+m)(k+q)\sigma}\right)-f\left(\varepsilon_{m'k\sigma}\right)}{\varepsilon_{(m'+m)(k+q)\sigma}-\varepsilon_{m'k\sigma}-\omega-\mathrm{i}0}, \tag{6}$$

where

$$\varepsilon_{mk\sigma}=\varepsilon_0\left(m+\frac{\Phi}{\Phi_0}\right)^2+\frac{k^2}{2m_*}+\sigma\mu_B B \tag{7}$$

is the electron energy in magnetic field [5], $\Phi=\pi a^2 B$ is the magnetic flux through the tube cross-section, $\Phi=2\pi c/e$ is the flux quantum (e is the electron charge, c is the speed of light), μ_B is the electron spin magnetic moment, $\sigma=\pm1$ is the spin quantum number, f is the Fermi function.

The function (6) depends on $|q|$ and satisfies the following symmetry properties:

$$\begin{gathered}\operatorname{Re}P_m(q,-\omega,-\Phi)=\operatorname{Re}P_m(q,\omega,\Phi),\\ \operatorname{Im}P_m(q,-\omega,-\Phi)=-\operatorname{Im}P_m(q,\omega,\Phi),\\ P_{-m}(q,\omega,-\Phi)=P_m(q,\omega,\Phi).\end{gathered} \tag{8}$$

Using $P_m=\sum_{m'\sigma}P^{\sigma}_{mm'}$, we obtain at zero temperature:

$$\operatorname{Re}P^{\sigma}_{mm'}(q,\omega)=-\frac{m_*L}{2\pi q}\left(\ln\left|\frac{-q\upsilon^{\sigma}_{m'+m}-\omega_q+\Omega_{mm'}-\omega}{-q\upsilon^{\sigma}_{m'}+\omega_q+\Omega_{mm'}-\omega}\right|+\ln\left|\frac{q\upsilon^{\sigma}_{m'}+\omega_q+\Omega_{mm'}-\omega}{q\upsilon^{\sigma}_{m'+m}-\omega_q+\Omega_{mm'}-\omega}\right|\right),$$

$$0<q<k^{\sigma}_{m'}-k^{\sigma}_{m'+m};$$

$$\operatorname{Re}P^{\sigma}_{mm'}(q,\omega)=-\frac{m_*L}{2\pi q}\ln\left|\frac{q\upsilon^{\sigma}_{m'}+\omega_q+\Omega_{mm'}-\omega}{q\upsilon^{\sigma}_{m'+m}-\omega_q+\Omega_{mm'}-\omega}\right|, \tag{9}$$

$$k^{\sigma}_{m'}-k^{\sigma}_{m'+m}<q<k^{\sigma}_{m'}+k^{\sigma}_{m'+m};$$

$$\operatorname{Re}P^{\sigma}_{mm'}(q,\omega)=-\frac{m_*L}{2\pi q}\ln\left|\frac{q\upsilon^{\sigma}_{m'}+\omega_q+\Omega_{mm'}-\omega}{-q\upsilon^{\sigma}_{m'}+\omega_q+\Omega_{mm'}-\omega}\right|,$$

$$q>k^{\sigma}_{m'}+k^{\sigma}_{m'+m};$$

$$\operatorname{Im}P^{\sigma}_{mm'}(q,\omega)=-\frac{m_*L}{2|q|}\left\{\Theta\left[\omega-\left(-q\upsilon^{\sigma}_{m'}+\omega_q+\Omega_{mm'}\right)\right]\Theta\left[-q\upsilon^{\sigma}_{m'+m}-\omega_q+\Omega_{mm'}-\omega\right]+\right.$$

$$\left.+\Theta\left[\omega-\left(q\upsilon^{\sigma}_{m'+m}-\omega_q+\Omega_{mm'}\right)\right]\Theta\left[q\upsilon^{\sigma}_{m'}+\omega_q+\Omega_{mm'}-\omega\right]\right\},$$

$$0<q<k^{\sigma}_{m'}-k^{\sigma}_{m'+m};$$

$$\operatorname{Im}P^{\sigma}_{mm'}(q,\omega)=-\frac{m_*L}{2|q|}\Theta\left[\omega-\left(q\upsilon^{\sigma}_{m'+m}-\omega_q+\Omega_{mm'}\right)\right]\Theta\left[q\upsilon^{\sigma}_{m'}+\omega_q+\Omega_{mm'}-\omega\right], \tag{10}$$

$$k^{\sigma}_{m'}-k^{\sigma}_{m'+m}<q<k^{\sigma}_{m'}+k^{\sigma}_{m'+m};$$

$$\operatorname{Im}P^{\sigma}_{mm'}(q,\omega)=-\frac{m_*L}{2|q|}\Theta\left[\omega-\left(-q\upsilon^{\sigma}_{m'}+\omega_q+\Omega_{mm'}\right)\right]\Theta\left[q\upsilon^{\sigma}_{m'}+\omega_q+\Omega_{mm'}-\omega\right],$$

$$q>k^{\sigma}_{m'}+k^{\sigma}_{m'+m}.$$

Here

$$\upsilon_m^\sigma = \frac{k_m^\sigma}{m_*} = \sqrt{\frac{2}{m_*}}\sqrt{\mu_0 - \varepsilon_{m\sigma}} \tag{11}$$

is the electron limiting velocity in the subzone with the number (m,σ),

$$\varepsilon_{m\sigma} = \varepsilon_0\left(m + \frac{\Phi}{\Phi_0}\right)^2 + \sigma\mu_B B$$

is the subzone boundary, $\omega_q = q^2/2m_*$, μ_0 is the chemical potential at zero temperature,

$$\Omega_{mm'} = \varepsilon_{(m'+m)\sigma} - \varepsilon_{m'\sigma} \tag{12}$$

are the frequencies of electron vertical transitions, Θ is the Heaviside function.

From the Eqs. (9) and (10) one can see that the polarization operator real part as function of the frequency ω has logarithmic singularities at the region boundaries on the plane (q,ω), in which the collisionless damping of plasma waves is absent. The boundaries of these regions are derivable from the formula (10). The polarization operator imaginary part is zero in the spectral windows for such plasma waves that are limited by parabolas on the plane (q,ω).

It follows from the equation (10) that each of the subzones in the electron energy spectrum is connected with a branch of plasma waves that propagate along the tube axis. In particular, for the branch with the number $m = 0$ the frequencies of the transitions (12) are zero and the dispersion equation (4) is reduced. Let us present the solution of this equation in the absence of magnetic field in the ultra-quantum limits, where only the lowermost subzone $'$ is filled up. In this case, there is a parabolic spectral window which is limited by the parabola $\omega = q\upsilon_0 - \omega_q$ and by the axis q on the plane (q,ω), the region is above the parabola $\omega = q\upsilon_0 + \omega_q$ and to the right of the parabola $\omega = -q\upsilon_0 + \omega_q$, in which the collisionless damping of the waves is absent. The analysis of the equation (4) indicates that in this case there are no solutions for the equation (4) in the parabolic spectral window. They do exist above the parabola $\omega = q\upsilon_0 + \omega_q$ and in the region of the collisionless damping. Above the parabola $\omega = q\upsilon_0 + \omega_q$, we have the following solution:

$$\omega_0(q) = q\upsilon_0 + \omega_q \operatorname{cth}\frac{2\pi^2 q}{m_*\upsilon_0(q)}. \tag{13}$$

In the long-wavelength approximation $qa << 1$, we shall use the expansions [10]:

$$I_0(x)K_0(x) \approx \ln\frac{2}{x\mathrm{e}^\gamma},$$
$$I_1(x)K_1(x) \approx \frac{1}{2}\left[1 + \frac{x^2}{2}\ln\frac{x}{2}\right], \tag{14}$$
$$I_m(x)K_m(x) \approx \frac{1}{2m}\left[1 - \frac{\left(\frac{x}{2}\right)^2}{m-1}\right] \quad (m = 2,3,\ldots),$$

where $x << 1$, $\gamma = 0,577\ldots$ is the Euler number. In this approximation using the formula (13) we obtain the plasmon

spectrum:

$$\omega_0(q) = \frac{\overline{e}^2}{\pi} q \ln \frac{2}{aq\mathrm{e}^{\gamma}}. \tag{15}$$

The dispersion of this wave is normal. In the region $qa \gg 1$ the dispersion curve (13) comes close to the parabola $\omega = q\upsilon_0 + \omega_q$ from above.

The plasma wave collisionless damping region is situated on the plane (q,ω) between the parabolas $\omega = q\upsilon_0 + \omega_q$, $\omega = q\upsilon_0 - \omega_q$ and $\omega = -q\upsilon_0 + \omega_q$. In this region the solution of the dispersion equation (4) in the case under consideration has the form:

$$\omega_0(q) = q\upsilon_0 + \omega_q \mathrm{th} \frac{2\pi^2 q}{m_* \upsilon_0(q)}. \tag{16}$$

In the long-wavelength limit we obtain hence:

$$\omega_0(q) = q\upsilon_0 + \frac{\pi q^3}{4m_*^2 \overline{e}^2 \ln \frac{2}{aq\mathrm{e}^{\gamma}}}.$$

In the limit $qa \gg 1$ the dispersion curve (16) approaches the parabola $\omega = q\upsilon_0 + \omega_q$ from below. It corresponds to the damping plasma wave.

In the absence of magnetic field in the case of long wavelengths $q\upsilon \ll \omega$ (υ – the Fermi electron velocity) we obtain the following equation from the formula (9):

$$\mathrm{Re}\, P_0(q,\omega) = \frac{qL}{\pi\omega} \sum_{m'} \Theta(\mu_0 - \varepsilon_{m'}), \tag{17}$$

where $\varepsilon_{m'} = \varepsilon_0 m'^2$ is the subzone boundary with the number m'. In case of a large number of filled subzones, we employ the Poisson formula for calculation of the sum:

$$\sum_{m=-\infty}^{\infty} \varphi(m) = \sum_{l=-\infty}^{\infty} \int_{-\infty}^{\infty} dx\, \varphi(x) \mathrm{e}^{2\pi i l x}. \tag{18}$$

Then for the mode $m = 0$ at $qa \ll 1$ we obtain:

$$\omega_0(q) = \frac{4\overline{e}^2}{\pi} q \ln \frac{2}{qa\mathrm{e}^{\gamma}} \sqrt{\frac{\mu_0}{\varepsilon_0}} \left(1 + \frac{1}{\pi} \sqrt{\frac{\varepsilon_0}{\mu_0}} \sum_{l=1}^{\infty} \frac{1}{l} \sin 2\pi l \sqrt{\frac{\mu_0}{\varepsilon_0}} \right). \tag{19}$$

The wave frequency undergoes quantum oscillations of the de Haas-van Alfven type with the Fermi energy variations being μ_0, as accounted for by crossing of the subzone boundaries by the Fermi level. The Fermi energy is associated with the linear density $n = N/L$ of electrons via the relationship:

$$n = \frac{2}{\pi} \sqrt{2m_* \varepsilon_0} \sum_{m} \left(\frac{\mu_0}{\varepsilon_0} - m^2 \right)^{1/2}.$$

The period of oscillations with varying $\sqrt{\mu_0}$ is equal to $1/\sqrt{2m_* a}$. It is determined by the electron effective

mass and by the tube radius. The relative oscillation amplitude $\sim \sqrt{\frac{\varepsilon_0}{\mu_0}}$ is small at $\mu_0 \gg \varepsilon_0$.

Let us consider the dispersion of modes with the numbers $m > 0$. In the long-wavelength limit, we obtain from the formula (9) that

$$\mathrm{Re}\, P_m = \frac{2m_* L}{\pi} \sum_{m'} \frac{\upsilon_{m'} - \upsilon_{m'+m}}{\omega - \Omega_{mm'}}, \tag{20}$$

where the summation is performed over those values of m', at which the sub-root expressions in (11) are positive.

The sum in Eq. (20) is calculated according to the Poisson formula (18). In the dispersion equation (34) we still consider that $qa \ll 1$. In addition, we shall restrict ourselves to the case of high frequencies that satisfy the inequality:

$$\omega >> \varepsilon_0 \left[\left(m + \sqrt{\frac{\mu_0}{\varepsilon_0}} \right)^2 - \frac{\mu_0}{\varepsilon_0} \right].$$

Here $\left[\sqrt{\frac{\mu_0}{\varepsilon_0}} \right]$ is the number of filled subzones. Then from the formula (20) we obtain:

$$\mathrm{Re}\, P_m = \frac{2\sqrt{2m_*\varepsilon_0}\, m^2 \mu_0 L}{\left(\omega^2 - \varepsilon_m^2\right)} \left[1 + \frac{2}{\pi} \sqrt{\frac{\varepsilon_0}{\mu_0}} \sum_{l=1}^{\infty} \frac{1}{l} \mathrm{J}_1 \left(2\pi l \sqrt{\frac{\mu_0}{\varepsilon_0}} \right) \right], \tag{21}$$

where J_1 is the Bessel function. In this case, the solutions of the equation (4) have the form:

$$\omega_1^2(q) = \varepsilon_1^2 + 2\overline{e}^2 \sqrt{2m_*\varepsilon_0}\, \mu_0 \left[1 + \frac{1}{2}(aq)^2 \ln \frac{aq}{2} \right] \left[1 + \frac{2}{\pi} \sqrt{\frac{\varepsilon_0}{\mu_0}} \sum_{l=1}^{\infty} \frac{1}{l} \mathrm{J}_1 \left(2\pi l \sqrt{\frac{\mu_0}{\varepsilon_0}} \right) \right],$$

$$\omega_m^2(q) = \varepsilon_m^2 + 2\overline{e}^2 \sqrt{2m_*\varepsilon_0}\, m\mu_0 \left[1 - \frac{(aq)^2}{4(m-1)} \right] \left[1 + \frac{2}{\pi} \sqrt{\frac{\varepsilon_0}{\mu_0}} \sum_{l=1}^{\infty} \frac{1}{l} \mathrm{J}_1 \left(2\pi l \sqrt{\frac{\mu_0}{\varepsilon_0}} \right) \right] \tag{22}$$

$$(m = 2,3,\ldots).$$

The cut-off wave frequencies with the spectrum (22) are equal to:

$$\omega_m^2(0) = \varepsilon_m^2 + 2\overline{e}^2 \sqrt{2m_*\varepsilon_0}\, m\mu_0 \left[1 + \frac{2}{\pi} \sqrt{\frac{\varepsilon_0}{\mu_0}} \sum_{l=1}^{\infty} \frac{1}{l} \mathrm{J}_1 \left(2\pi l \sqrt{\frac{\mu_0}{\varepsilon_0}} \right) \right] \tag{23}$$

$$(m = 1,2,\ldots).$$

The dispersion of these waves is anomalous. Their frequencies undergo the above-considered oscillations associated with the traversal of the subzone boundaries by the Fermi level.

Non-degenerate electron gas

In this Section we employ the Boltzmann distribution function to compute the polarization operator (9), (10) in the absence of magnetic field. The real and imaginary parts of the polarization operator of the Boltzmann electron gas are as follows:

$$\mathrm{Re}\, P_m(q,\omega) = \frac{N}{q} \sqrt{\frac{m_*\beta}{2}} \left\langle \mathrm{F}\left(x_{mm'}^-\right) - \mathrm{F}\left(x_{mm'}^+\right) \right\rangle, \tag{24}$$

$$\mathrm{Im}\, P_m(q,\omega) = \frac{N}{|q|} \sqrt{\frac{\pi m_*\beta}{2}} \left\langle \exp\left(-\beta \frac{k_{mm'}^{+2}}{2m_*} \right) - \exp\left(-\beta \frac{k_{mm'}^{-2}}{2m_*} \right) \right\rangle, \tag{25}$$

where

$$\left\langle ... \right\rangle = \frac{\sum_{m'} e^{-\beta\varepsilon_0 m'^2} ...}{\sum_{m'} e^{-\beta\varepsilon_0 m'^2}},$$

$$F(x) = \frac{1}{\sqrt{\pi}} P. \int_{-\infty}^{\infty} dy \frac{e^{-y^2}}{x-y},$$

$$x_{mm'}^{\pm} = \frac{1}{q}\sqrt{\frac{m_*\beta}{2}}\left(\omega_{\pm} \pm \Omega_{mm'}^{\pm}\right),\ \Omega_{mm'}^{\pm} = 2m\varepsilon_0\left(\frac{m}{2} \mp m'\right),\ k_{mm'}^{\pm} = \sqrt{\frac{2m_*}{\beta}}\, x_{mm'}^{\pm},\ \omega_{\pm} = \omega \pm \omega_q,$$

β is the inverse temperature. The number of electrons N, as included in (24) and (25), is associated with the chemical potential μ via the relation:

$$N = \sqrt{\frac{2m_*}{\pi\beta}} L e^{\beta\mu} \sum_{m=-\infty}^{\infty} e^{-\beta\varepsilon_0 m^2} = \sqrt{\frac{2m_*}{\varepsilon_0}} \frac{L}{\beta} e^{\beta\mu} \sum_{l=-\infty}^{\infty} \exp\left(-\frac{\pi^2 l^2}{\beta\varepsilon_0}\right).$$

Here we use the formula [11]:

$$\sum_{m=-\infty}^{\infty} \exp\left[-(m+b)^2 x\right] = \sqrt{\frac{\pi}{x}} \sum_{l=-\infty}^{\infty} \exp\left(-\frac{\pi^2 l^2}{x}\right) \cos 2\pi l b. \tag{26}$$

To calculate the spectrum and the damping of the mode with the number $m = 0$ we use the following expressions:

$$\begin{aligned} \operatorname{Re} P_0(q,\omega) &= \frac{N}{q}\sqrt{\frac{m_*\beta}{2}}\left[F\left(\sqrt{\frac{m_*\beta}{2}}\frac{\omega_-}{q}\right) - F\left(\sqrt{\frac{m_*\beta}{2}}\frac{\omega_+}{q}\right)\right], \\ \operatorname{Im} P_0(q,\omega) &= -\frac{N}{|q|}\sqrt{2\pi m_*\beta}\,\operatorname{sh}\frac{\beta\omega}{2}\exp\left(-\frac{\beta m_*\omega^2}{2q^2} - \frac{\beta q^2}{8m_*}\right). \end{aligned} \tag{27}$$

In the long-wavelength limit $qr_D \ll 1$ (r_D is the Debye screening radius), we obtain the following from the formula (27):

$$\begin{aligned} \operatorname{Re} P_0(q,\omega) &= \frac{Nq^2}{m_*\omega^2}, \\ \operatorname{Im} P_0(q,\omega) &= -\frac{N}{|q|}\sqrt{\frac{\pi m_*\beta}{2}}\beta\omega\exp\left(-\frac{\beta m_*\omega^2}{2q^2}\right). \end{aligned} \tag{28}$$

Then from the dispersion equation in the case of $qa \ll 1$, we obtain the plasma wave spectrum

$$\omega_0^2(q) = \frac{2\overline{e}^2 n}{m_*} q^2 \ln\frac{2}{aqe^{\gamma}}. \tag{29}$$

The decrement of the damping of this wave

$$\gamma(q) = \frac{\operatorname{Im} P\left(q,\omega(q)\right)}{\frac{\partial}{\partial\omega(q)}\operatorname{Re} P\left(q,\omega(q)\right)} \tag{30}$$

is equal to

$$\gamma_0(q)=\sqrt{\frac{\pi}{8}}\left(\frac{m_*\beta}{q^2}\right)^{3/2}\omega_0^4(q)\exp\left[-\frac{\beta m_*}{2}\left(\frac{\omega_0(q)}{q}\right)^2\right]. \tag{31}$$

The dispersion of the wave with the spectrum (29) is normal, the damping decrement (31) diminishes exponentially at $\rightarrow$.

The real part of the polarization operator (24) at $|m|>0$ within the long-wavelength limit is:

$$\mathrm{Re}\,P_m=\frac{N}{2\varepsilon_0}\left\langle\left\{\left[m'-\frac{\omega}{2m\varepsilon_0}\right]^2-\frac{m^2}{4}\right\}^{-1}\right\rangle. \tag{32}$$

The included sums $\sum_{m'}$ in the case of $\beta\varepsilon_0\ll 1$ can be replaced by integrals. Therefore

$$\mathrm{Re}\,P_m=-\frac{N}{2m}\sqrt{\frac{\beta}{\varepsilon_0}}\left\{\mathrm{F}\left(\sqrt{\beta\varepsilon_0}\left[\frac{\omega}{2m\varepsilon_0}+\frac{m}{2}\right]\right)-\mathrm{F}\left(\sqrt{\beta\varepsilon_0}\left[\frac{\omega}{2m\varepsilon_0}-\frac{m}{2}\right]\right)\right\}. \tag{33}$$

In the case of the high frequencies that satisfy the inequality

$$\omega>>2m\varepsilon_0\left(\frac{m}{2}+\frac{1}{\sqrt{\beta\varepsilon_0}}\right),$$

one can use the asymptote of the function $\mathrm{F}(x)\approx x^{-1}$ at $x\gg 1$. Then the expression (33) is approximated by

$$\mathrm{Re}\,P_m=\frac{2N\varepsilon_0 m^2}{\omega^2-\varepsilon_m^2}. \tag{34}$$

By substituting this expression in the dispersion equation (4) at $qa\ll 1$, we obtain:

$$\omega_1^2(q)=\varepsilon_0^2+2\overline{e}^2\varepsilon_0 n\left[1+\frac{(aq)^2}{2}\ln\frac{aq}{2}\right], \tag{35}$$

$$\omega_m^2(q)=\varepsilon_m^2+2\overline{e}^2\varepsilon_0 n|m|\left[1-\frac{a^2q^2}{4(|m|-1)}\right]\qquad(m=\pm2,\pm3,\ldots). \tag{36}$$

The wave dispersion with the spectrum (35), (36) is anomalous. The cut-off frequencies in the spectrum of these waves are

$$\omega_m^2(0)=\varepsilon_m^2+2\overline{e}^2\varepsilon_0 n|m|. \tag{37}$$

To compute the decrement of the damping of the modes with the numbers $|m|>0$, we shall make use of the formula (30), (34) and of the imaginary part of the polarization operator (25) that is equal in the long-wavelength limit to:

$$\mathrm{Im}\,P_m=-\frac{N}{|m|}\sqrt{\frac{\pi\beta}{\varepsilon_0}}\mathrm{sh}\frac{\beta\omega}{2}. \tag{38}$$

Then the decrement of the damping of the waves with the spectrum (35), (36) is as follows:

$$\gamma_1(q)=\frac{\overline{e}^4\varepsilon_0 n^2}{\omega_1(q)}\sqrt{\frac{\pi\beta}{\varepsilon_0}}sh\frac{\beta\omega_1(q)}{2}\left[1+\frac{(aq)^2}{2}\ln\frac{aq}{2}\right]^2, \tag{39}$$

$$\gamma_m(q)=\frac{\overline{e}^4\varepsilon_0 n^2}{|m|\omega_m(q)}\sqrt{\frac{\pi\beta}{\varepsilon_0}}\,\mathrm{sh}\,\frac{\beta\omega_m(q)}{2}\left[1-\frac{a^2q^2}{4(|m|-1)}\right]^2 \qquad (m=\pm2,\pm3,...). \tag{40}$$

The ratio γ_m/ω_m decreases with increasing mode number in proportion to $|m|^{-3}$.

Magnetoplasma waves

In the magnetic field, which is parallel to the cylinder axis, the energy of electron is given by Eq. (7), while the polarization operator of degenerate electron gas is derived in Eq.(9), (10).

Let us obtain the solution of the dispersion equation (4) in the ultra-quantum limit, when only two subzones are filled with the numbers $(m,\sigma)=(0,\pm)=0^{\pm}$. In this case, there are lobe and triangular spectral windows in the wave vector-frequency plane besides the parabolic spectral window which is found between the parabola $\omega=q\upsilon_0^+-\omega_q$ and the axis q, and also besides the collisionless wave damping region above the parabola $\omega=q\upsilon_0^-+\omega_q$ and to the right of the parabola $\omega=-q\upsilon_0^-+\omega_q$. The lobe spectral window is confined within the parabolas $\omega=q\upsilon_0^++\omega_q$ and $\omega=q\upsilon_0^--\omega_q$, and the triangular spectral window is limited by the parabolas $\omega=-q\upsilon_0^++\omega_q$, $\omega=q\upsilon_0^--\omega_q$ and the axis q. The coordinates of the lobe window uppermost boundary in the plane (q,ω) are $\left(m_*\left(\upsilon_0^--\upsilon_0^+\right),\frac{m_*}{2}\left(\upsilon_0^{-2}-\upsilon_0^{+2}\right)\right)$. If $q<m_*\left(\upsilon_0^--\upsilon_0^+\right)$, solutions for the equation (4) exist in the lobe spectral window above the parabola $\omega=q\upsilon_0^-+\omega_q$ and in the regions of collisionless damping. The dispersion law of magnetoplasma wave in the lobe spectral window is

$$\omega_0(q)=q\frac{\upsilon_0^++\upsilon_0^-}{2}+\omega_q\mathrm{cth}\frac{2\pi^2q}{m_*\upsilon_0(q)}-\left[\frac{q^2}{4}\left(\upsilon_0^+-\upsilon_0^-\right)^2+\frac{\omega_q^2}{\mathrm{sh}^2\dfrac{2\pi^2q}{m_*\upsilon_0(q)}}\right]^{1/2}. \tag{41}$$

At small values of q the spectrum of this wave is linear. With increasing q, the dispersion curve (41) comes closer to the lobe boundary $\omega=q\upsilon_0^++\omega_q$. The appearance of the quantum number of the magnetic flux Φ/Φ_0 in the formula (7) has its effect on the wave spectrum brought for consideration in Section I. In particular, the formula (19), in the presence of magnetic field and taking into account (26), takes the following form:

$$\omega_0(q)=\frac{4\overline{e}^2}{\pi}q\ln\frac{2}{qa\mathrm{e}^{\gamma}}\sqrt{\frac{\mu_0}{\varepsilon_0}}\left(1+\frac{1}{\pi}\sqrt{\frac{\varepsilon_0}{\mu_0}}\sum_{l=1}^{\infty}\frac{1}{l}\sin2\pi l\sqrt{\frac{\mu_0}{\varepsilon_0}}\cos2\pi l\frac{\Phi}{\Phi_0}\right). \tag{42}$$

This formula does not account for the spin splitting of the levels. Besides the oscillations of the de Haas-van Alfven type, which were considered in Section I, appearing with changing μ_0, the wave frequency undergoes oscillations of the Aharonov-Bohm type appearing with changing magnetic field. The period of these oscillations is equal to one quantum of the magnetic flux Φ_0. In the magnetic field, the linear electron density n is connected with the chemical potential μ_0 via the relation:

$$n = \frac{2}{\pi}\sqrt{2m_*\varepsilon_0}\sum_m\left[\frac{\mu_0}{\varepsilon_0} - \left(m + \frac{\Phi}{\Phi_0}\right)^2\right]^{1/2}.$$

The frequencies of modes with the numbers $|m| > 0$ also undergo the Aharonov-Bohm type oscillations. In the formulae (22), (23), under the sign of the sum $\sum_l$, it appears the factor $\cos 2\pi l\frac{\Phi}{\Phi_0}$.

Conclusions

The energy spectrum (2) of electron on the nanotube surface is a set of one-dimensional subzones, the positions of the boundaries of which are not equidistant. As a result, the density of states (3) oscillates with changing $\sqrt{\varepsilon}$ with the period $\left(\sqrt{2m_*}a\right)^{-1}$. This accounts for the oscillations of plasma wave frequencies in the degenerate electron gas with changing value of $\sqrt{\mu_0}$. These oscillations resemble the de Haas-van Alfven oscillations of electron gas magnetization that emerge with changing magnetic field strength. This distinction is attributed to existence of the non-equidistant boundaries of the subzones in the spectrum (2). The cause of the oscillations is a jumping density variation of the density of states, when the Fermi level traverses the subzone boundaries. The measurement of the period of the oscillations allows to obtain $\sqrt{m_*}a$. To be able to observe these oscillations, it is necessary to have the capability to change the Fermi level of electrons on the tube like it is done in the two-dimensional electron gas [12]. While measuring the plasmon frequencies on tubes with different values of m_*, a, μ_0, a spread of the frequency values should be expected, caused by the oscillations.

In a magnetic field, which is parallel to the cylinder axis, the Aharonov-Bohm oscillations appearing with changing magnetic field will be superposed on the magnetoplasma wave frequency oscillations of the de Haas-Van Alfven type. The reason for the former oscillations differs. Their period does not depend on μ_0 and is equal to one quantum of the magnetic flux Φ_0. It related to the area πa^2, which is occupied by the projection of the orbit of electron to the plane $z = 0$, and it does not depend on the energy of the electron.

The oscillations described here can be observed in experiments on the measurement of the cross-section of scattering of the light and electrons by plasma waves on the nanotube surface.

Acknowledgement. The author is very grateful to professor A.M. Ermolaev for fruitful discussion of the results of this article.

References

1. M.S. Dresselhaus, G. Dresselhaus, and P.C. Eklund, Science of Fullerenes and Carbon Nanotubes (Academic, New York, 1996).
2. L.I. Magarill, A.V. Chaplik, M.V. Entin, Uspehi fizicheskikh nauk **175**, 995 (2005).
3. R.C.T. da Kosta, Phys. Rev. **A23**, 1982 (1981).
4. L.I. Magarill, D.A. Romanov, A.V. Chaplik, JETP **113**, 1411 (1998).
5. V.A. Geyler, V.A. Margulis, A.B. Shorohov, JETP **115**, 1450 (1999).
6. R.Z. Vitlina, L.I. Magarill, A.V. Chaplik, JETP letters **86**, 132 (2007).
7. G.D. Mahan, Phys. Rev. **B69,** 125407 (2004).
8. A.M. Ermolaev and G.I. Rashba, J. Phys.: Condens. Matter **20**, 175212 (2008).
9. V.V. Rotkin, R.A. Suris, Fizika tverdogo tela **36**, 3569 (1994).
10. H. Bateman, A. Erdelyi, Higher Transcendental Functions (Mc Graw-Hill Book Company, New York, 1953), Vol. 1,2.
11. A.P. Prudnikov, U.A. Brichkov, O.I. Marichev, Integrali i ryadi (Nauka, Moskva, 1981).
12. T. Ando, A. Fowler, and F. Stern, Rev. Mod. Phys. **54**, 437 (1982).

Вісник ХНУ, серія «Фізика», вип. 25, 2016. с. 26-29

PACS numbers: 42.15.-i; 42.25.-p; 42.50.Ct; 42.50.Wk; 42.62.Fi; 42.65.-k
УДК 535.016; 535.1; 535.318; 535.321.9; 535.324.2; 535.39; 535.434

Stimulated Doppler effect on the surface of a gas bubble thermocapillary trapped by a laser in an absorbing liquid

V.I. Lymar, N.A. Kazachkova, O.I. Kofman, N.V. Slabunova, N.A. Luzan

V.N. Karazin Kharkiv National University, Svobody Sq., 4, Kharkiv, 61022, Ukraine
lymar@univer.kharkov.ua

A possibility to control the gas bubble size in an absorbing liquid through the laser thermo-capillary trapping has been demonstrated. The coarse structure of the observed interference patterns in reflected and transmitted lights are explained qualitatively within the framework of a two-ray approach. The movement of interference fringes can be treated as manifestation of the Doppler effect because of the moving bubble walls. The method to measure the relative refractive index value for moving contiguous media by means of the Doppler shifts ratio measurement has been proposed. There is a two times discrepancy between Doppler shifts ratio value predicted theoretically and measured in the experiment. It is following from a special stimulated character of the Doppler effect at experimentally realized non-equilibrium thermodynamic conditions, that are imposed by the laser light field.

Keyword: thermocapillary trap; gas bubble; laser beam scattering; interference pattern; refractive index; Doppler effect.

Продемонстровано можливість контролю та управління розміром газової бульбашки, яка знаходиться у поглинаючій світло рідині та захоплена у лазерну термокапілярну пастку. Груба структура інтерференційних картин, що спостерігаються у відбитому та пройденому світлі, пояснюється якісно в рамках двопроменевого наближення. Рух інтерференційних смуг можна розглядати як прояв ефекту Доплера на рухомих стінках бульбашки. Запропоновано метод визначення відносного показника заломлення двох суміжних середовищ з рухомою границею розділу між ними через вимірювання відношення доплерівських зсувів частот. Наявне двократне розходження у значеннях цього відношення, передбаченого теоретично та виміряного експериментально, пояснюється як прояв особливого вимушеного характеру ефекту Доплера, який реалізується експериментально при нерівноважних термодинамічних умовах, зумовлених дією лазерного випромінювання.

Ключові слова: термокапілярна пастка; газова бульбашка; розсіювання лазерного світла; інтерференційна картина; показник заломлення; ефект Доплера.

Продемонстрирована возможность контроля и управления размером газового пузырька, который находится в поглощающей свет жидкости и захвачен в лазерную термокапиллярную ловушку. Грубая структура интерференционных картин, которые наблюдаются в отраженном и пропущенном свете, объясняется качественно в рамках двухлучевого приближения. Движение интерференционных полос можно рассматривать как проявление эффекта Доплера на движущихся стенках пузырька. Предложен метод определения относительного показателя преломления двух смежных сред с движущейся границей раздела между ними посредством измерения отношения доплеровских сдвигов частот. Имеющееся двухкратное расхождение в значениях этого отношения, предсказываемого теоретически и измеренного экспериментально, объясняется как проявление особенного вынужденного характера эффекта Доплера, который реализуется экспериментально при неравновесных термодинамических условиях, обусловленных действием лазерного излучения.

Ключевые слова: термокапиллярная ловушка; газовый пузырек; рассеяние лазерного света; интерференционная картина; показатель преломления; эффект Доплера.

Introduction

Light fields are subjected to substance distribution for the most of the well-known classical optical phenomena in nature, but soon afterwards laser invention and, especially, after particles laser trapping experiments, it became clear that alternative contrary situations are possible up to and including Bose-Einstein condensation. Microparticles with relative refractive index $n>1$ are trapped easily by means of known Ashkin's dipole force technique. To trap particles with $n<1$, e.g. gas bubbles in liquid, it becomes rather more involved [1]. But because of surface tension temperature dependence it is possible to trap the gas bubble easily using so-called dissipative thermo-capillary force in the absorbing liquids [2, 3]. A broad size range of the bubbles, captured by a light beam, a large action radius and a high specific value of the capturing force are some of the useful thermo-capillary trap properties [4]. In the process they are evidently adjustable varying with the liquid medium absorbance. It is believed our results also can be regarded as an increasing appeal of the optical thermo-capillary gas

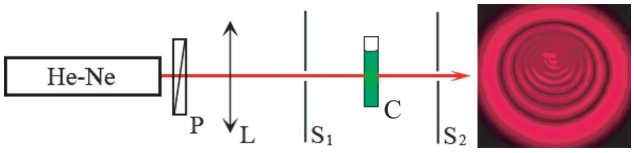

Fig. 1. Principal experimental scheme of the laser thermocapillary trap: **He-Ne** – laser used; **P** – linear polarizer; **L** – convergent lens; **C**– cell with an absorbing liquid; **S1** and **S2** – plane screens. Photo inset shows observed on screen **S2** pattern of Gaussian laser beam thermal self-defocusing.

bubble trap technique.

Experimental scheme and results

Our experimental setup is extremely simple (Fig. 1). A linearly polarised laser beam is focused on the cell C, containing an absorbing liquid, by means of the converging lens L. The cell is arranged between the screens S_1 and S_2 to observe the interference patterns (see lower) in reflected (RL) and transmitted light (TL). The polarizer P is used to control the laser beam power. There is some degree of freedom in the choice of laser types and liquids, but, evidently, laser light wavelength has to fall into the absorption band of the liquid. He-Ne-laser at λ = 632.8 nm and power P ≈ 15 mW jointly with ethanol solution, coloured by brilliant green dye, has been applied in our experiments. The photo in Fig. 1 demonstrates thermal self-defocusing (thermal lens aberration) observed on the screen S_2, created by a focused Gaussian laser beam in the solution mentioned above. But if the gas bubble is captured by the beam [2], then interference patterns shown in photos of Fig. 2 are appearing sharply on the screens S_1 and S_2. The radii of circular interference fringes are increasing or decreasing with time obviously in the process of bubble size change. As a rule, at laser power P ≈ 10 mW, diameters of the interference circles grow if a gas bubble is trapped in a dense solution, and, on the contrary, they reduce if capturing takes place in a dilute solution. It is noticeable that this evolution process can be controlled by means of the linear polarizer P. The process of changing the size of captured gas bubble can be stopped by increasing or decreasing the laser beam power and directed toward gas bubble growth or collapse at will.

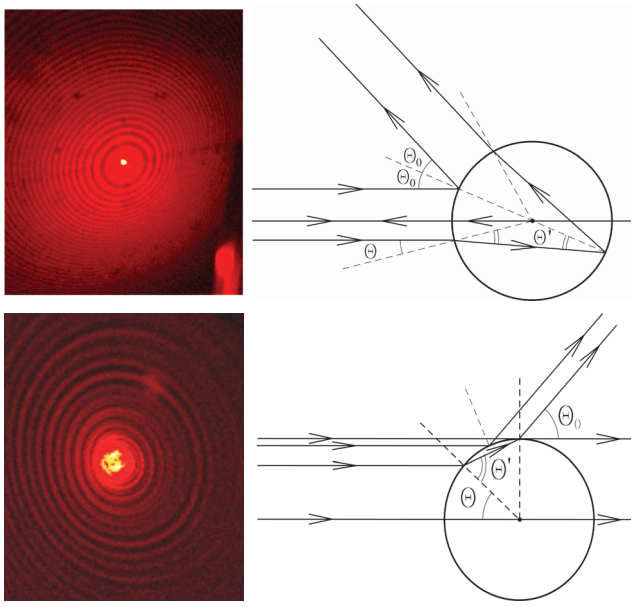

Fig. 2. The interference patterns observed on the screens **S1** in reflected (upper) and **S2** in transmitted (lower) lights after the gas bubble capture. The drawing schemes explain the patterns in an approach of two-ray interference: **Θ** and **Θ′** are angles of incidence and refraction on the gas bubble surface; $\mathbf{2\Theta_0}$ and $\mathbf{\Theta_0}$ are angles of deflections in reflected and transmitted lights.

Two-ray interference and Doppler effect

The interference pictures in the photos (Fig. 2) have both coarse (CFS) and fine fringe structures (only the CFS is noticeable in the photos). Certainly, Mie theory [5, 8] or generalized Lorenz-Mie theory [6] has to be applied to explain the structure completely. But one way of looking at the CFS is in terms of two-ray interference. Beam courses are sketched on the schemes in Fig. 2 at zero and maximum angles of deflection (n=1.360 is taken as the initial value for ethanol). If $2\Theta_0$ and Θ_0 are deflection angles in RL and TL accordingly, their magnitudes determine interference circles radiuses, Θ and Θ′ are angles of incidence and refraction on a bubble surface (Fig. 2), then the following correlations take place:

$$\theta_0 = 2\cdot\theta' - \theta \text{ in RL; } \theta_0 = 2\cdot(\theta' - \theta) \text{ in TL;}$$
$$\sin\theta' = n\cdot\sin\theta \quad .$$

In doing so, an optical path difference is arising in RL:

$$\Delta_r(\theta) = d\cdot\left(2\cdot\cos\theta' - n\cdot(\sin\theta_0 + \sin\theta)\cdot\tan(\theta' - \theta)\right). \quad (1)$$

And the same in TL:

$$\Delta_t(\theta) = d\cdot(\cos\theta' - n\cdot\cos\theta)\cdot(1 - \sin\theta'). \quad (2)$$

Here d is a bubble diameter. If this value is changing with time then, for a constant interference order, the values of deflection angles have to be changed both in RL and in TL. It clarifies the interference patterns movement. Let time derivatives be specified by primes. Then we have at the limit of zero deflection angles from (1) and (2):

$$\left|\Delta_r'(0)/\Delta_t'(0)\right| = 2/(n-1) = \left|\delta\omega_r/\delta\omega_t\right|. \quad (3)$$

In Eqn. (3) the last fraction is the ratio of Doppler frequency shifts for the waves reflected from ($\delta\omega_r$) and transmitted through ($\delta\omega_t$) the moving dielectric interface [7]. Hence observed interference patterns time evolution can be treated as a manifestation of the Doppler effect on the moving bubble walls. Measurement of the Doppler shifts ratio (DSR) gives the method to determine the

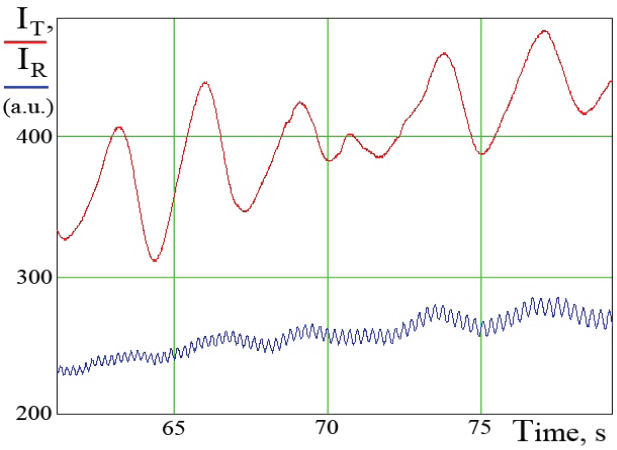

Fig. 3. The time dependences of the transmitted $\mathbf{I_T}$ (upper red) and reflected $\mathbf{I_R}$ (lower blue) signals at moving interference patterns of Fig. 2; the observation angle ($n\cdot\Theta_0$ for $\mathbf{I_T}$ and $2\cdot n\cdot\Theta_0$ for $\mathbf{I_R}$) is equal to 1/15 rad. The experimental value of Doppler frequency shifts ratio is $\delta\omega_r/\delta\omega_t \approx 71/6$.

refractive index n value in the vicinity of the bubble.

To carry out the measurement, optical fibers were arranged instead of the screens S_1 and S_2 (Fig. 1). Reflected and transmitted signals were communicated by means of the fibers to photomultipliers and further to computer after an analogue-digital transformation. One of the measurement results is displayed in Fig. 3. The transmitted signal I_T is sketched by the upper red curve, the reflected I_R – by the lower blue.

In doing so the angle of observation ($n\cdot\Theta_0$ for I_T and $2\cdot n\cdot\Theta_0$ for I_R) was ~1/15 rad. According to (3) at initial value n=1.360 the DSR has to be equal about six, while from Fig. 3 it results in 71/6, i.e. close to twelve.

At first glance, this two-times disagreement is naturally connected with a rough estimate of our two-ray interference model. To elucidate the question the MiePlot-4503 program [8] was applied to the problem of a plane wave scattering on the gas bubble surrounded by ethanol. At reasonably small deflection angles in RL and TL the program gives the DSR value about 63/10, which is in a satisfactory correspondence with Eqn. (3). Therefore, both Mie theory, and two-ray interference model results in the same DSR. Another source of the discrepancy could be caused by the motion of the gas bubble centre in the process of a bubble growth or collapse [9]. But a more attentive examination of this item testifies to the validity of Eqn. (3): a displacement of the bubble as a whole has no influence on the optical path differences $\Delta_r(0)$ and $\Delta_t(0)$ in the RL and TL accordingly.

Stimulated Doppler effect

From the above discussion it follows that the theoretical approaches do not take into account one essential feature of the experiment – the movement of gas bubble walls is stimulated by the laser light. At the limit of zero deflection angles the Doppler effect takes place on the moving back bubble surface only, both in RL and TL, because the front bubble wall is constantly in contact with an immobile wall of the cell [2]. Let a photon of the laser light be an incident on some small-scale area of the back bubble wall

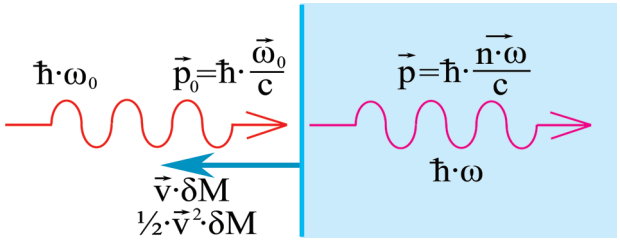

Fig. 4. A photon of the laser light is an incident on some small-scale area of the back moving bubble wall: ω_0 and ω are the frequencies of the photons incident on and passed through the surface accordingly; n is the refractive index of the liquid; $\vec{v}$ is the velocity of the moving interface.

(Fig. 4). If δM is some mass, connected with that area (the sense of δM will be adjusted later on), then the following impulse-energy conservation laws have to be fulfilled:

$$\vec{\mathbf{p}}_0 = \vec{\mathbf{p}} + \vec{\mathbf{v}}\cdot\delta M; \tag{4}$$

$$\hbar\cdot\omega_0 = \hbar\cdot\omega + \mathbf{v}^2\cdot\delta M/2. \tag{5}$$

Here $\left(\vec{\mathbf{p}}_0,\ \hbar\cdot\omega_0\right)$ is an impulse-energy of the incident photon; $\left(\vec{\mathbf{p}},\ \hbar\cdot\omega\right)$ is the same of the transmitted one; $\left(\vec{\mathbf{v}}\cdot\delta M,\ \mathbf{v}^2\cdot\delta M/2\right)$ is the same of the mass δM. Assuming $\omega \approx \omega_0$ and in the collinear geometry, as it is shown in Fig. 4, we have:

$$\delta M \approx \pm\frac{\hbar\cdot\omega_0}{\mathbf{v}\cdot c}\cdot(n-1); \tag{6}$$

$$\delta\omega_t = \omega-\omega_0 \approx \mp\frac{(n-1)\cdot\mathbf{v}}{2\cdot c}\cdot\omega_0. \tag{7}$$

In Eqns. (6, 7) the upper sign corresponds to the counter movement of the incident wave and the interface (as in Fig. 4), the lower sign – to their passing movement. Perhaps, the δM could be named, to some extent, as a "mass defect" of the treated small-scale area in the process of photon transition through the surface, the movement of which is stimulated by that transition. In our case this "mass defect" has rather a classical, non-relativistic nature: if δM is a positive, then a gas condensation process is occurring into the liquid; at opposite condition the liquid evaporation into the gas phase is preferred. The condensation-evaporation processes are controlled in our experiment by means of the laser light intensity value and it is possible because non-

equilibrium thermodynamic conditions, created by the laser beam, have realized in our system.

Eqns. (6) and (7) describe stimulated Doppler effect (SDE) at the collinear geometry in TL. The well-known substitution of the refractive index n value on minus unity [10] in these equations leads to the formulas, which deal with the SDE at the collinear geometry in RL:

$$\delta M \approx \mp \frac{2 \cdot \hbar \cdot \omega_0}{\mathbf{v} \cdot c}; \tag{8}$$

$$\delta\omega_r = \omega - \omega_0 \approx \pm \frac{\mathbf{v}}{c} \cdot \omega_0. \tag{9}$$

Certainly, Eqns. (6) - (9) corresponds to the particular cases of the more general non-collinear SDE. From Eqns. (4) and (5) it is straightforward to deduce the extended relations for the SDE "mass defect" δM and Doppler shift δω:

$$\delta M \approx -\frac{\hbar}{\mathbf{v}^2} \cdot \vec{\mathbf{v}} \cdot \delta\vec{\mathbf{k}}; \tag{10}$$

$$\delta\omega = \omega - \omega_0 \approx \frac{1}{2} \cdot \vec{\mathbf{v}} \cdot \delta\vec{\mathbf{k}}, \tag{11}$$

where $\delta\vec{\mathbf{k}} = \vec{\mathbf{k}} - \vec{\mathbf{k}}_\mathbf{0}$ is the wave vector change in the process assuming $\omega \approx \omega_0$.

Eqns. (6), (8) or (10) points out the fact that the process of interface movement should be consistent with the process of mass release or deposition. In contrast to the classical Doppler effect (CDE), the SDE is not possible simultaneously in transition and reflection on the same portion of the surface because of the different signs and values of δM in RL and TL. If the SDE takes place at small deflection angles in transmition, then the CDE should be observed at the same angles in reflection or vice versa. We suppose it is the former that has been realized in our experiment. Doppler frequency shifts at the CDE are two times greater than the corresponding SDE shifts, $\delta\omega_t$, $\delta\omega_r$ or δω in Eqns. (7), (9) or (11). Then the DSR $\delta\omega_r/\delta\omega_r$ value ought to be double of the result of Eqn. (3), if the CDE is present in RL and the SDE – in TL. Finally, it is necessary to note, that at a non-stimulated nature of the gas bubble growth or collapse it is the classical DSR value of Eqn. (3) that should be observed in experiments, since only the CDE should take place on the bubble walls.

Summary

As it has been mentioned above, laser beam thermal self-defocusing is observed in our experiment. It indicates of the noticeable optical nonlinearity of the used liquid. The measurement of the DSR gives a possibility to determine the refractive index value n including a nonlinear optics contribution. Therefore, at the limit of zero deflection angles we have:

$$\frac{\delta\omega_r}{\delta\omega_t} = \frac{4}{n-1} \approx \frac{71}{6}. \tag{12}$$

Calculated by Eqn. (12) value $n \approx 1.338$ is much better than by using Eqn. (3). But we have to take into account that our measurements were carried out at the non-zero observation (deflection) angles. Under the assumption that the SDE takes place as well at the total internal reflection on the bubble periphery, it follows from Eqn. (11) the linear angle correction to the DSR is equal to $2n \cdot \theta_0/(n-1)^2$, here $n \cdot \theta_0$ is the observation angle in TL, its magnitude is equal to 1/15 rad. An approximately half of that value is accounted for the angle half-width of the self-defocusing pattern shown in the photo-inset of Fig. 1. That is why we suppose that only the half of the angle correction written above is suitable to correct the DSR value:

$$\frac{4}{n-1} + \frac{n \cdot \theta_0}{(n-1)^2} \approx \frac{71}{6}. \tag{13}$$

Last equation results in $n \approx 1.3539$. It is the latter value that we consider as final and therefore the refractive index variation $\Delta n \approx 0.006$ is caused by the thermal optical nonlinearity. These results are in sufficiently well accordance with the experimental estimations obtained in the earlier research [2, 9].

In conclusion, the refractive index determination by means of the DSR measurements is well suited method for optical applications, especially in the field of nonlinear optics.

Acknowledgment

V. I. L. would like to express a sincere gratitude to Prof. Philip Laven for his remarkably helpful Internet site [8] and, especially, for his kind permission to use the program MiePlot-4503 and its results for the report. To the light memory of V.K. Miloslavsky.

References

1. Lankers M., Khaled E.E.M., Popp J., Rossling G., Stahl H., and Kiefer W., Determination of size changes of optically trapped gas bubbles by elastic light backscattering, Appl. Opt., vol. 36, No.7, pp.1638-1643, 1997.
2. Yarovaya R.G., Makarovskii N.A., and Lupashko N.A., Influence of a laser beam on the motion of gas bubbles in an absorbing liquid, Sov. Journ. Tech. Phys., vol. 33, No.7, pp. 817-821, 1988.
3. Bazhenov V.Yu., Vasnetsov M.V., Soskin M.S., and Taranenko V.B., Dynamics of laser-induced bubble and free-surface oscillations in an absorbing liquid, Appl. Phys. B, vol. B49, pp. 485-489, 1989.
4. Ivanova N.A., Bezugliy B.A., Optical thermocapillary trap for a bubble, Pis'ma Zhurn. Tekhn. Fiz., vol. 32, No.19, pp. 66-71, 2006. *(in Russian)*.
5. C.F. Bohren, and D.R. Huffman, Absorption and scattering of light by small particles (Wiley, New-York, 1983).
6. G. Gouesbet, G. Grehan, Generalized Lorenz-Mie theories (Springer-Verlag, Berlin-Heidelberg, 2011).
7. I. Ye. Tamm, Foundations of electricity theory (Nauka, Moscow, 1989). *(in Russian)*.
8. See, please, the internet site "The Optics of a Water Drop (Mie Scattering and the Debye Series)" by Prof. Philip Laven: http://www.philiplaven.com/ index1.html; http://www.philiplaven.com/mieplot.htm/.
9. A.D. Butenko, N.A. Kazachkova, O.I. Kofman and V.I. Lymar, "Optical gas bubble management" at its laser thermo-capillary trapping in an absorbing liquid, ME-21 in Proceedings of the 10th Int. Conf. on Laser-light and Interactions with Particles, F. Onofri and B. Stout, eds., Aix-Marseille University, Marseille, August 2014.
10. R.P.Feynman, R.B. Leighton, M. Sands, The Feynman lectures on physics (Addisson-Wesley Pub. Co., Reading-London, 1963).

Вісник ХНУ, серія «Фізика», вип. 25, 2016. с. 30-42

81.05.Je; 82.45.Qr; 81.15.Pq; 82.45.Yz
УДК 620.22 – 621.921.34

Effect of NbN doping on forming of the structure in diamond-(Fe-Cu-Ni-Sn) system and physico-mechanical properties of this composites

V.A. Mechnik[1], E.S. Gevorkyan[2], N. A. Bondarenko[1],
S.R. Vovk[3], I. M. Chursina[3], R.V. Vovk[3]

[1]V. Bakul Institute for Superhard Materials of the National Academy of Sciences of Ukraine, Avtozavodskaya Street 2, Kiev 04074, Ukraine
[2]Ukrainian State University of Railway Transport (UkrSURT), Feyerbakh square 7, Kharkov 61001, Ukraine
[3]V.N. Karazin Kharkov National University 61022, Svobody sq. 4, Kharkov 61022, Ukraine

In this study the changes in the structure of the transition zone of diamond – metal bond and the metal bond in composites diamond-(Fe-Cu-Ni-Sn-NbN), after sintering in an oven at 800C for 1 hour in dependence of the parameters of the hot mounting pressing and their influence on the mechanical and tribological properties, was investigated. It is shown that an increase in pressure from 100 to 200 MPa and with a duration of the hot mounting pressing from 2 to 3 minutes, the composition diamond-(49,98Fe-31,36Cu-8,82Ni-7,84Sn-2NbN) provides an increase of 4,3 times in the wear resistance of the samples by improving the retention of the diamond grains of the metal bond and increases the strength limits upon compression from 758 to 890 MPa and upon bending from 754 to 880 MPa. This is consistent with a change in the phase composition, the morphology and the structure of the phase components of the composite. It was found that samples of composites diamond-(49,98Fe-31,36Cu-8,82Ni-7,84Sn-2NbN) have higher wear resistance than the composites diamond-(51Fe-32Cu-9Ni-8Sn) of about 3,8 times and 2, 4 times higher regarding the samples diamond-(49,98Fe-31,36Cu-8,82Ni-7,84Sn-2CrB2), obtained under the same conditions. Thus, in the composite metal bond with the addition of powder NbN, grinding of the elements of the structure occurs, which is accompanied by the disappearance of the pores at the interphase boundaries. It was elucidated the mechanism, which provides increase (enhances) the tribological properties of such composites.

Keywords: Diamond, iron, copper, nickel, tin, niobium nitride, metal bond, transition zone, phase, composite, pressure, temperature, structure, properties, wear resistance.

Досліджено зміни структури перехідної зони алмаз-металева зв'язка і металевої зв'язки в композитах алмаз-(Fe-Cu-Ni-Sn-NbN) після спікання в прес-формі в печі при температурі 800 °С впродовж 1 год залежно від параметрів гарячої допресовки та досліджено їх вплив на механічні і трибологічні властивості. Показано, що збільшення тиску від 100 до 200 МПа і тривалості гарячої допресовки від 2 до 3 хв композиту алмаз-(49,98Fe-31,36Cu-8,82Ni-7,84Sn-2NbN) забезпечує підвищення в 4,3 рази його зносостійкості за рахунок поліпшення утримання алмазних зерен металевою зв'язкою та підвищення границі міцності під час стиску від 758 до 890 МПа і згинання - від 754 до 880 МПа. Це добре узгоджується зі зміною фазового складу, морфологією фазових складових та структурою композиту. Встановлено, що зразки алмаз-(49,98Fe-31,36Cu-8,82Ni-7,84Sn-2NbN) мають зносостійкість вище, ніж зразки алмаз-(52Fe-32Cu-9Ni-8Sn) в 3,8 і 2,4 рази для зразків алмаз-(49,98Fe-31,36Cu-8,82Ni-7,84Sn-2CrB_2), одержаних в однакових умовах. При цьому в металевій зв'язці композиту з добавкою порошку NbN відбувається подрібнення елементів структури, яке супроводжується зникненням пор на міжфазних границях. З'ясовано механізм, який забезпечує підвищення трибологічних властивостей таких композитів.

Ключові слова: алмаз, залізо, мідь, нікель, олово, нітрид ніобію, металева зв'язка, перехідна зона, фаза, композит, тиск, температура, структура, властивості, зносостійкість.

Изучены изменения структуры переходной зоны алмаз металлическая связка и металлической связке в композитах алмаз(Fe-Cu-Ni-Sn-NbN) после спекания в пресс-форме в печи при температуре 800 С в течение 1 ч в зависимости от параметров горячей до прессовки и исследовано их влияние на механические и трибологические свойства. Показано, что увеличение давления от 100 до 200 МПа и продолжительности горячей допрессовки от 2 до 3 мин композицииалмаз(49,98Fe-31,36Cu-8,82Ni-7,84Sn-2NbN) обеспечивает повышение в 4,3 раза износостойкости образцов за счет улучшения удерживания алмазных зерен металлической связкой и повышения пределов прочно-сти при сжатии от 758до 890 МПа и изгибе от 754 до 880 МПа. Это хорошо согласуется с изменением фазового состава, морфологии фазовых составляющих и структуры композита. Установлено, что образцы композитов ал-маз(49,98Fe-31,36Cu-8,82Ni-7,84Sn-2NbN) имеют износостойкость выше, чем композиты алмаз(51Fe-32Cu-9Ni-8Sn) в 3,8 и 2,4 раза для образцов алмаз(49,98Fe-31,36Cu-8,82Ni-7,84Sn-2CrB2), полученных в одинаковых условиях. При этом в металлической связке композита с добавкой порошка NbN происходит измельчение элементов структуры, которое сопровождается исчезновением пор на межфазных границах. Выяснено механизм, который обеспечивает повышение трибологических свойств таких композитов.

Ключовые слова: алмаз, железо, медь, никель, олово, нитрид ниобия, металлическая связка, переходная зона, фаза, композит, давление, температура, структура, свойства, износостойкость.

Introduction

At the present time, intensive research works in the diamond composite material (DCM) system diamond-(Fe-Cu-Ni-Sn), which are used for the manufacture of tools for stone processing and mining industries, are conducting, regarding the nature of the physical and chemical processes occurring during the formation of the composition, their influence to the structure and the properties [1, 2]. These processes are determined the structure-phase state of the composition in all steps of sintering and the mechanical properties of the DCM [3, 4]. Such DCM should have high hardness, strength, durability (wear resistance) and reliability, should have the ability to be self-sharpening and be chemically inert to the reactants of coolant. Specific results obtained in the study, have applied to the development of new DCM with predetermined properties [5-11].

In [12, 13] was shown that directed changes in the structure and phase composition of the transition zone diamond-metallic bond of the DCM diamond-(51Fe-32Cu-9Ni-8Sn) by varying with technological parameters of the hot mounting pressing after sintering in the mold in the oven, allow a significant impact on their physical and mechanical properties. In these works, is also noted that the presence in the microstructure of a transition zone of lamellar precipitates of graphite neighboring the diamond grains, it is a major cause of premature failure by a mechanism of intense cracking and falling of diamond grains with a metal bond, as well as the deterioration of the composite. The study of the carbon (non-diamond) interaction, formed in the surface graphitization of diamond grains, with the metal bond components during sintering compositions diamond-(51Fe-32Cu-9Ni-8Sn) in the mold in an oven at 800C for 1 hour followed by hot mounting pressing, showed that the formation of Fe3C nanostructures in the transition zone allows higher values of the metal bond regarding hardness, the strength limits under (upon) compression and bending, as well as the wear resistance of the DCM in various conditions of their practical use [14]. In [14], it was noted that an increase in pressure from 100 to 200 MPa and hot mounting pressing from 2 to 3 minutes, provides complete decarburization in the transition zone diamond-metal bond and increases 2 times the wear resistance of the DCM.

Hence, correlations between the structure of the transition zone, phase composition and the physical -mechanical properties of DCM on the one hand and their wear resistance from the other were observed.

To improve the mechanical and performance properties of DCM, in the initial materials is introducing hromium diboride (CrB2) additives in a small amount comparing with the basic components [15-18]. Thus, a necessary condition to provide the desired structure and properties of the DCM is not only a uniform distribution of the components in the bulk metal bond, but also the realization of the interaction of carbon, formed during graphitization of the surface diamond grains in sintering process of the composition, with the solid phases α-Fe and CrB2 during its hot mounting pressing. Borides, nitrides, carbides and silicides of the transition metals as activating materials [19] continue to play a major role in enhancing the durability and the performance properties of heterophase composites and, in the opinion of the lead experts, they will remain on such positions for many more years [20-23]. Often when using such additives, the transition zone is contaminated by the reaction products, which generates structural instability and degrades the DCM properties [15, 16]. Laws of structure formation in the system in the presence of solid additives, such as NbN, are not currently investigated.

The aim of this work is to study the impact of the NbN additive in the composition diamond-(51Fe-32Cu-9Ni-8Sn), as well as the effect of the technological modes of the hot mounting pressing on the structural-phase state of the transition zone and to the metal bond, the mechanical and tribological properties of sintered at 800 C for 1 h in the mold in the oven composites and to identify the mechanism for the improvement of their structure, to increase the wear resistance and, as well, to compare the results with the data obtained in [14, 17, 18].

Experimental methods

The objects of the experiment were: powder mixtures 51Fe-32Cu-9Ni-8Sn and diamond-(51Fe-32Cu-9Ni-8Sn). From these, were obtained pellets at room temperature and at a pressure of 100 MPa, as well as samples of metal bond and DCM (10 mm in diameter and with thickness of 8 mm) and thin foils (with thickness 80-100 nm). To produce DCM samples, was used powders of diamond AS160T, graininess 400/315 (TU 2-37-344-85), iron PZH1M2 (GOST 9849-74), copper ICP-1 (GOST 4960-75), nickel GNU (GOST 9722-79), tin PO-1 (GOST 9723-73), chromium diboride (CrB2) (70.62% wt. Cr and 29.30% wt. B) and niobium nitride (NbN) (86.82% wt. Nb and 13.10% wt. N), produced by the Donetsk plant of chemical reagents. The methodology in batch processing, the process parameters to obtain DCM samples and the experimental methods of their tribological properties are described in detail in [14]. To study the microstructure and properties of the DCM samples, it was taken into account the data regarding the dependence of the wear of the Cutting Diamond Segmented Circles (CDSC), 320 mm in diameter in the cutting process of the granite (Janevski deposit, Ukraine), with a thickness of 30 mm at a speed of longitudinal flow of 100 cm/min and cutting capacity of 300 cm^2/min, from the content of the NbN in the batch diamond-(51Fe-32Cu-9Ni-8Sn), obtained by us (Table 1).

The work elements (40,0 mm x 12,0 mm x 3,2 mm) were sintered in the mold in a muffle furnace at 800 C for 1

Table 1

Dependence of the wear of the CDSC from the NbN content in the composition of DCM

Circle	NbN content	Specific consumption of diamonds, ct / m^2 of cutting area
1	0	1,80
2	0,5	1,18
3	1,0	0,95
4	1,5	0,68
5	2,0	0,35
6	2,5	0,81
7	3,0	1,63
8	4,0	2,34
9	5,0	3,26
10	6,0	4,00

hour, followed by hot mounting pressing under pressure of 200 MPa. The most resistant to abrasion proved CDSC (5), of which the work elements contained in the composition of the initial batch 2% (wt.) NbN. This became the basis for determining the optimal composition of the batch and the study of the structure and the properties of the DCM. The microstructure of the metal bond and of the transition zone diamond-metal bond of DCM samples and the associated diffraction patterns were examined with the transmission electron microscope SELMI TEM with a potential acceleration of 125 kV at a resolution of 0,18 nm. The quantitative phase composition of the metallic bond was calculated using the package MAUD. Thin foil specimens from DCM for the study of the microstructure of the transition zone, and metal bond obtained by polishing in the electrolyte 20% HClO4 + 30% HNO3 + H2O.

The diffraction patterns from the NbN powder and the sample of the metal bond with composition 49,98Fe-31,36Cu-8,82Ni-7,84Sn-2NbN obtained by the diffractometer DRON 4.13S in the emission of copper anode in Bragg-Brentano geometry in the range of angles 20° ~ 2θ ~ 80°. The X-ray phase analysis was performed by standard methods using the software package X - powder [24]. The diffraction spectrum of the samples as a set of revised values of the interplanar spacing of the crystal lattice phase d_i and the relative intensities of the reflexes of this phase *Ii* were identified by comparing with the references from the catalogs ASTM-ICPDS [25]. The morphology of the surface of the transition zone and its chemical composition was studied in a scanning electron microscope SELMI SEM - 106M, with a potential acceleration of 20 kV. Quantitative calculations of chemical composition performed using ZAF correction method and the software package magelanes 3.1. Determination error: for heavy elements ~ 0.01% (wt.), for light elements ~ 1% (wt.).

The microhardness of the samples was determined by the PMT- 3 device using a Vickers indenter at a load of 4,91 N. Print sizes were measured at a magnification of 25 times. The hardness was calculated by the formula Hb = 0,4636P / x2, where P - load; x - indentation diagonal. The limits of the compressive strength and bending strength was investigated by the standard method (error ~ 5%). The tribological tests were performed on samples of QAM multi-functional apparatus for testing materials of friction without lubrication scheme disc (corundum counterface of medium hardness SM-2 vitrified 7K15 diameter of 60 mm and a width of 8) -palets (sample KAM), which was established on the basis of serial car IMASH- 20-75 [26]. The normal load on the sample at the disc was 500 g, the disc rotation speed was 300 rev/min and the duration of steps was: burnishing works and testing, 0,5 and 4,0 hours, respectively, which corresponds to the friction path (L) 1,7 and 13,6 km. During the tests, it was recorded the friction coefficient *f*, the massive wear Δ*m*, defined by the weight loss of the samples in weighing analytical balances VLA-20g-M (accuracy ±4 mg) and the mass wear intensity Im (I_m=Δ*m*/*L*).

Results and discussion

Structure of NbN and the condition of the initial materials before and after sintering

X-ray and diffractometric studies shown, that the niobium nitride (NbN) in the initial state has a two-phase

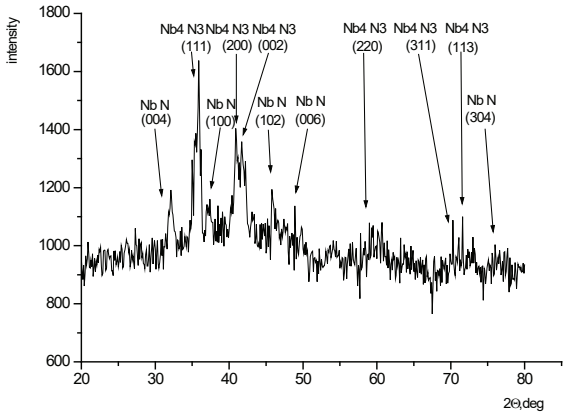

Fig. 1. The X-ray diffraction diagram of NbN in the initial state.

structure. Thus, on the X-ray diffraction diagram of the NbN powder (Fig. 1), are recorded interference reflexes from the planes, (111), (200), (002), (220), (311), (113) for phase Nb4N3 (tetragonal) with a crystal lattice period a = 0,4382 nm, c = 0,4316 nm, V = 0,8288 nm3 and (004), (100), (102), (006), (304) for the NbN phase (hexagonal) with a crystal lattice period a = 0,2956 nm and c = 1,1270 nm, V = 0,8531 nm3, which is consistent with the bibliography [25] and the experimental data [19].

Factual studies have established that NbN powder in the initial (bulk) state consists of irregularly shaped

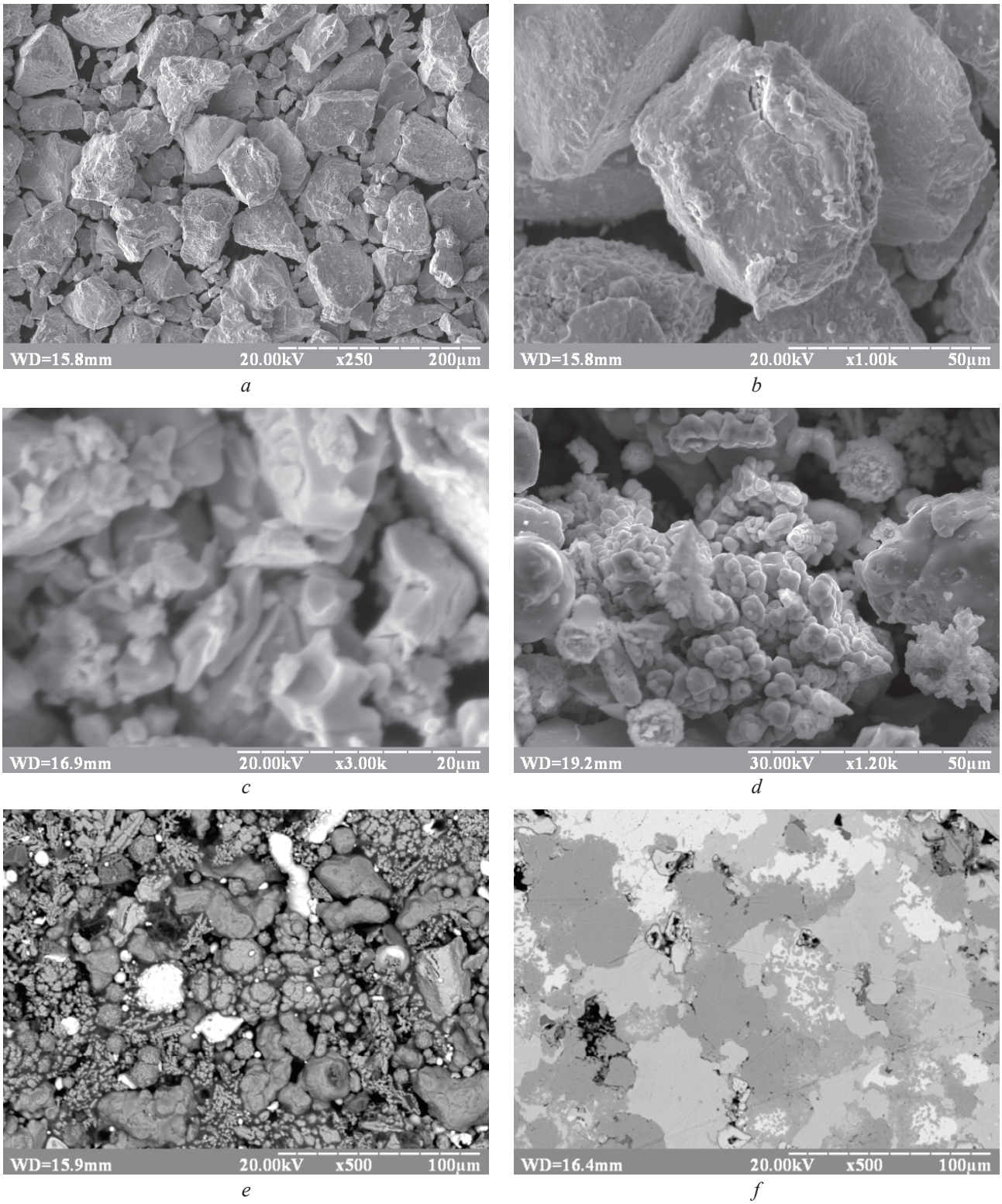

Fig. 2. SEM images of NbN particles in the initial state (a, b) and cold pressed fractogram of the NbN powder at a pressure of 100 MPa (c); photomicrographs of the initial mixture 49,98Fe-31,36Cu-8,82Ni-7,84Sn-2NbN (d), the briquette, obtained from the initial mixture at a pressure of 100 MPa, (d) and bond sample (e) obtained at a temperature of 800 C for 1 hour with hot mounting pressing at a pressure of 100 MPa.

particles, the average size of which ranges between 10-30 µm (Fig. 2a), although we meet also some larger particle size (up to 50 µm) (Fig. 2b) with a developed surface. It is characteristic that particles larger than 40 µm have an irregular shape with relief with irregularities, the number of which increases by increasing the particle size. In the particles smaller than 20-30 µm, by reducing further the size, the irregularities are smoothed out. When compacting at room temperature, the NbN particles do not change the shape, between them is observed gaps, that predetermined

by the insufficient compaction pressure (100 MPa). The strength of the compact in this case is determined by the mechanical clamping of particles (Fig. 2c). The shape and the dimensions of powders of iron, copper, nickel, tin, and niobium nitride NbN to the resulting mixture, in comparison with separate particles in the initial state, has not changed (Fig. 2d). During briquetting the mixture, i.e. in the process of cold compaction at a pressure of 100 MPa, the shape of particles of iron, copper, nickel and niobium nitride does not change (Fig. 2e), although, compared with the initial state, they are compacted more strongly (Fig. 2a, b, d). However, in the process of pressing the mixture, all particles are deformed due to their contact each other. Thus, there is a relatively uniform distribution of all components.

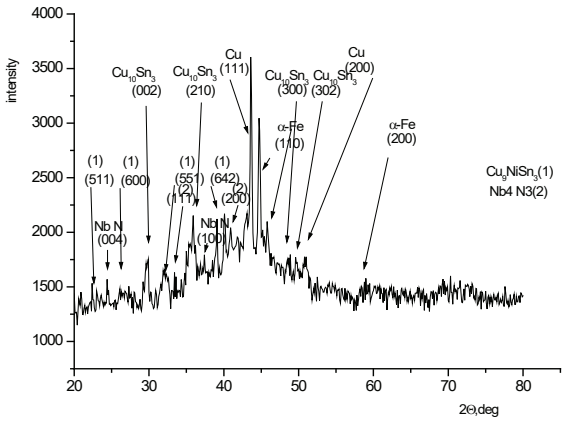

Fig. 3. The XRD diagram of the surface of the sample with a metallic bond of composition 49,98Fe-31,36Cu-8,82Ni-7,84Sn-2NbN, obtained by sintering in the mold in an oven at 800 C for 1 hour with hot mounting pressing at a pressure of 160 MPa for 3 min.

During sintering the briquette, the compaction of the bond components occurs by adjusting the surfaces of adjacent particles to one another, which contributes to a compact contact at the interphase boundaries in the composite bunch (Fig. 2f). In addition, the sintered metal bond sample is characterized by a homogeneous structure throughout the volume, which is an advantage and points to prospects for its use in DCM technology. All this affects the structure and properties of the DCM.

Table 2.

The diffraction data for the metal bond sample

d_i nm	2 θ, deg	I_i	Phase	*hkl*
0,33594	26,5333	464,12	Cu_9NiSn_3	511
0,3284	29.5934	574,53	NbN	004
0,30192	29,5879	546,64	Cu_9NiSn_3	600
0,25074	35,8172	561,99	$Cu_{10}Sn_3$	002
0,23046	39,0861	579,46	Nb_4N_3	111
0,22482	40,1091	658,25	Cu_9NiSn_3	511
0,22465	40,1409	588,10	$Cu_{10}Sn_3$	210
0,22131	40,7733	533,36	NbN	100
0,22036	40,9576	522,45	Cu_9NiSn_3	642
0,21090	42,8822	579,03	Nb_4N_3	200
0,20727	43,6727	949,84	Cu	111
0,20278	44,6909	901,66	α-Fe	110
0,19798	45,8348	571,58	$Cu_{10}Sn_3$	300
0,18793	48,5764	476,25	$Cu_{10}Sn_3$	302
0,18375	49,6121	543,15	Cu	200
0,18001	50,7152	529,04	α-Fe	200

Fig. 3 shows a diffractogram of the metallic bond sample 49,98Fe-31,36Cu-8,82Ni-7,84Sn-2NbN, obtained by sintering in the mold in an oven at 800 C for 1 hour, followed by hot mounting pressing at a pressure of 160 MPa for 3 min. The interference maxima on the X-ray XRD from the (111) and (200) for phase for copper (lattice parameter a = 0,3608 nm); (110) and (200) for iron (a = 0,2863 nm); (002) (210) (300) (302); (211) Cu10Sn3; (511) (600) (551) (642) Cu9NiSn3 (a = 1,801 nm); (111) (200) and (220) Nb4N3 (a = 0,4382 nm) and (004), (100) NbN (a = 0,2956 nm, c = 1,1274 nm) are consistent with [25] and the corresponding parameters for copper, iron, and niobium nitride [19]. Diffraction data (interplanar spacing, relative intensity, the angles 2θ, phase and lattice indices (hkl), corresponding to the interference maxima), are shown in Table 2. Crystal structure and quantitative phase composition of the bond sample are shown in Table 3. Analysis of the results showed that during the formation of the metal bond sample occurs elements' interaction that forms solid solutions on the basis of copper and iron

Table 3.

The crystal structure and phase composition of the metal bond of DCM

Phase	PG	Lattice parameter, nm			Concentration phase, % (wt.)	
		A	*в*	*C*	SEM	XRD
Cu	*Fm*3*m*	0,3608	–	–	41,8	44,2 ± 2,3
α-Fe	*Im*3*m*	0,2857			38,5	34 ± 1,8
Cu_9NiSn_3	*F*-43*m*	1,8010			19,7	12,1 ± 1,9
$Cu_{10}Sn_3$	*hP*26	–	–	–		7,1 ± 1,3
NbN	*C*6/*m*2	0,2952	–	1,1271	–	2,2 ± 0,9
Nb_4N_3	–	0,4381	–	0,4312	–	0,4 ±0,7

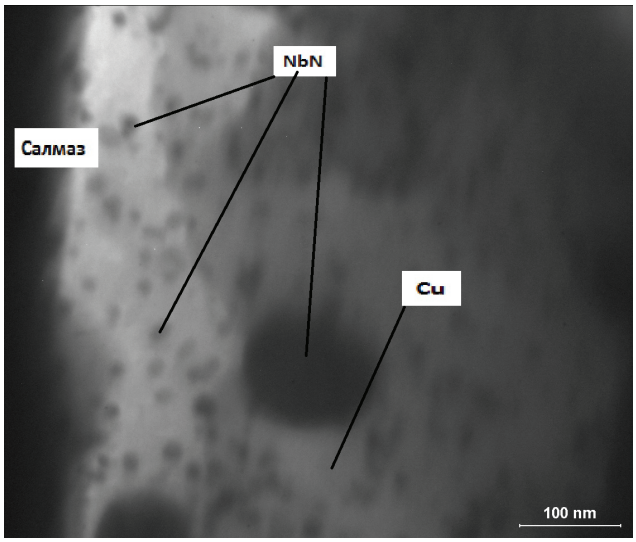

a

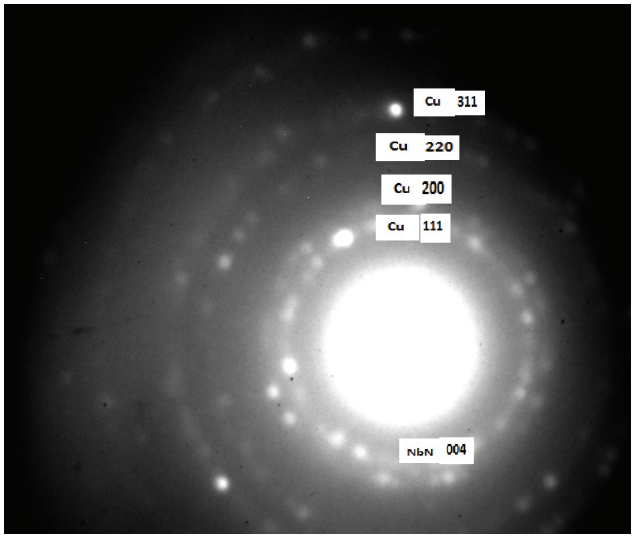

b

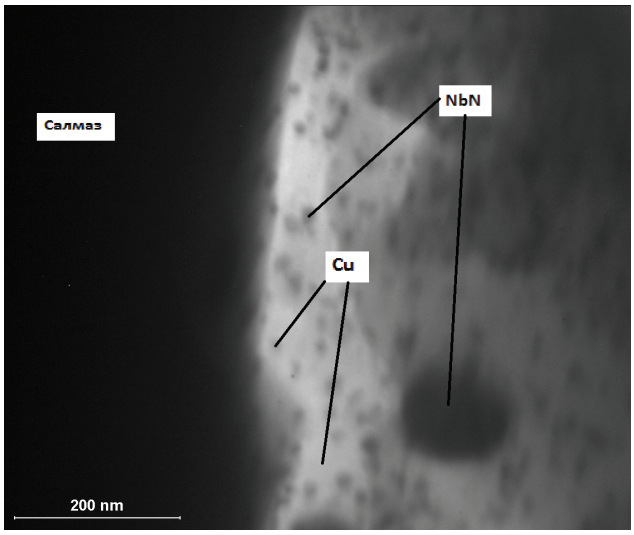

c

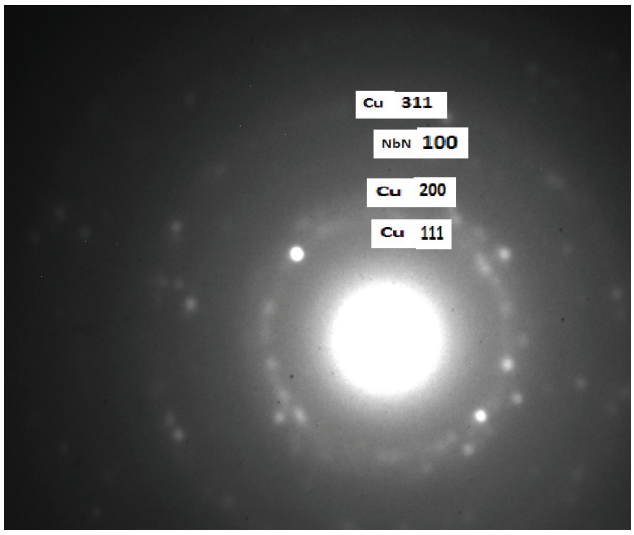

d

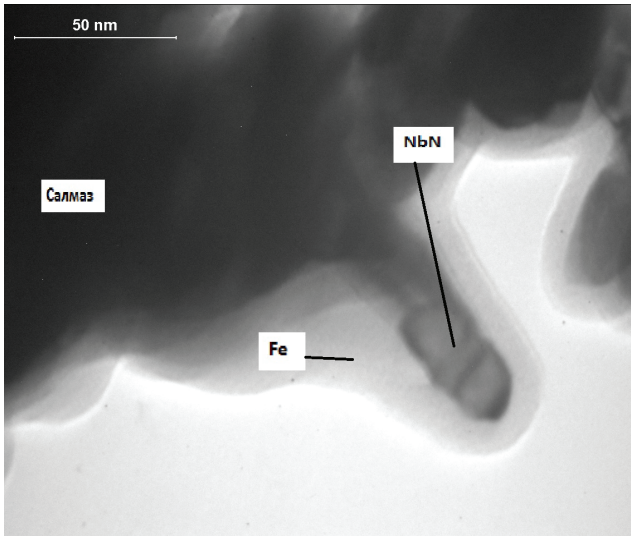

e

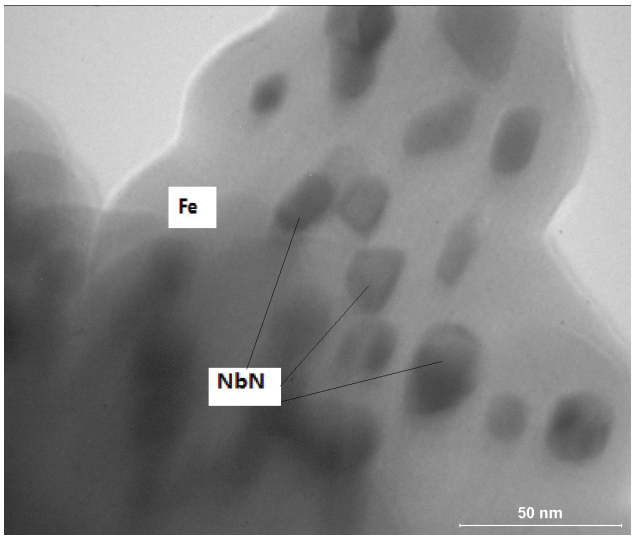

f

Fig. 4. TEM images of the sections of the transition zone diamond-metal bond of the samples 1 (a), 2 (b), 3 (e), 4 (f) and microelectrongraphs of its fragments for samples 1 (b), 2 (d): (a, b) - p = 100 MPa, t = 2 min; (c, d) - p = 100 MPa, t = 3 min; (e) - p = 200 MPa, t = 2 min, (f) - p = 200 MPa, t = 3 min.

(main phases), which is confirmed by the change in lattice parameters compared to the pure elements for copper (a = 0,3615 nm) and iron (a = 0,2864 nm), as well as the formation of new phases - Cu9NiSn3 and Cu10Sn3.

Comparison of the results with the data of [14] shows that the introduction of NbN in the amount of 2% (wt.) in the composition of the metal bond sample 51Fe-32Cu-9Ni-8Sn affects the phase formation in the process of its formation. Furthermore, the content of the sintered sample of the formed phases Cu9NiSn3 and Cu10Sn3 is respectively 12.1% (wt.) and 7.1% (wt.), which can affect the mechanical and tribological properties of the DCM.

The structure of transition zone diamond-metal bond of the sintered samples DCM

The results of the structural studies of the transition zone diamond-metal bond of DCM samples obtained from the batch diamond-(49,98Fe-31,36Cu-8,82Ni-7,84Sn-2NbN), sintering in the mold in an oven at 800 C for 1 hour, in dependence from *p-t* parameters of the hot mounting pressing, is shown in Fig. 4. The microstructure of the transition zone diamond-metal bond of obtained DCM samples (Fig. 4, a, c, e, f) is radically different from the above described microstructure of sintered samples of the metal bond. The structure of the transition zone diamond-metal bond of the sample 1, obtained at a pressure of 100 MPa, under hot mounting pressing for 2 minutes, is composed of copper phase and niobium nitride, which are uniformly distributed in the absence of graphitic inclusions (Fig. 4a). The grain size in the transition zone does not exceed 100 nm. Furthermore, niobium nitride NbN is present as inclusions in spherical shape, average particle size is from 10 to 100 nm, which is considerably smaller than the niobium nitride in the initial state (10-50 μm) (see Fig. 2a, b). As a result, the microstructure of the transition zone of the sintered DCM sample includes both nano-sized crystals of copper separated by almost invisible boundaries and nanoscale inclusions of niobium nitride. In this case, the contact diamond-metal bond is very tight; the boundaries between the grains are thin, clearly formed, with no visible pores and cracks, which has a positive effect on the performance properties of the DCM.

At the roundabout prints of the mikroelectrongraphs of this sample are clearly visible the interference reflexes for the phases of Cu and NbN (Fig. 4b). Copper phase grains are textured in the directions (311), (220), (200) and (111) and niobium nitride phase grains in the direction (004). Expansion of the diffraction peaks on circular (ring) imprints indicating a low degree of crystallinity of these phases. By increasing the duration of the hot mounting pressing from 2 to 3 minutes, the structure of the transition zone remains practically unchanged (sample 2) (Fig. 4c). In this case, the copper phases grains textured in the directions (311), (200) and (111) and niobium nitride phase grains in the direction (100). Expansion of the diffraction peaks in the ring imprints on mikroelectrongraphs of this sample once more confirms the low degree of crystallinity of the phases of Cu and NbN (Fig. 4d). Diffraction data (interplanar spacing and phase identification codes of the crystal lattice (hkl)) for samples 1 and 2 are shown in Tables 4 and 5. The calculated values *di* for the phases are coincide with the data in [18], indicating the reliability of the results. Thus, our experimental data on the structural state of the transition zone of the investigated composites and their comparison with previous experimental data [5-7, 9-11] suggest that the use of the NbN in the composition diamond-(51Fe-32Cu-9Ni-8Sn) completely eliminates the phase transformation diamond → graphite at the sintering stage, which is very important to improve the structure and the working (exploitation) properties of such DCM

It was revealed that when the pressure of hot mounting pressing increases from 100 to 200 MPa in samples 3 and 4 is formed a solid nanograin structure of the transition zone with uniformly distributed phase α-Fe and NbN (Fig. 4, e, f). A characteristic feature of these results is the absence of both the graphite inclusions in the transition zone and the formation of carbide phases, which reduces its brittleness and, as a consequence, is very important to improve the structure and improve service properties such DCM.

Below are the studies that were carried out regarding the effect of the structure of the transition zone of the obtained DCM samples to their physical, mechanical and tribological properties.

Peculiar properties of the transitional zone diamond-

Table 4

The diffraction data of the transition zone for the sample DCM 1

d_i (calculation), nm	d_i (experiment), nm	Phase	*hkl*
0,2570	0,2580	NbN	400
0,2079	0,2080	Cu	111
0,1811	0,1808	Cu	200
0,1280	0,1270	Cu	220
0,1090	0,1090	Cu	311

Table 5

The diffraction data of the transition zone for the sample DCM 2

d_i (calculation), nm	d_i (experiment), nm	Phase	*hkl*
0,2079	0,2080	Cu	111
0,1810	0,1808	Cu	200
0,1661	0,1470	NbN	110
0,1092	0,0900	Cu	311

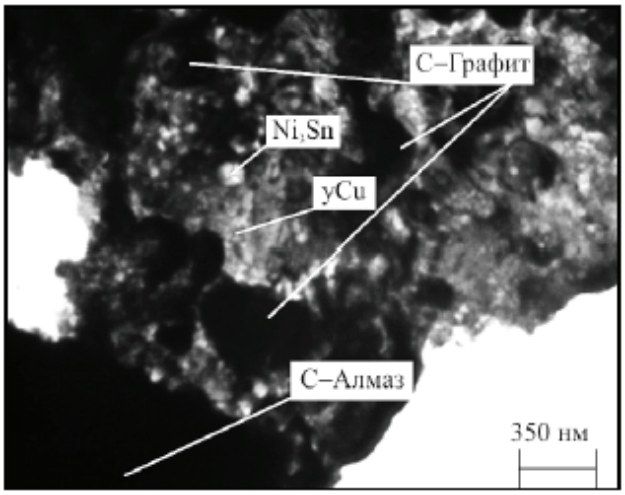

a

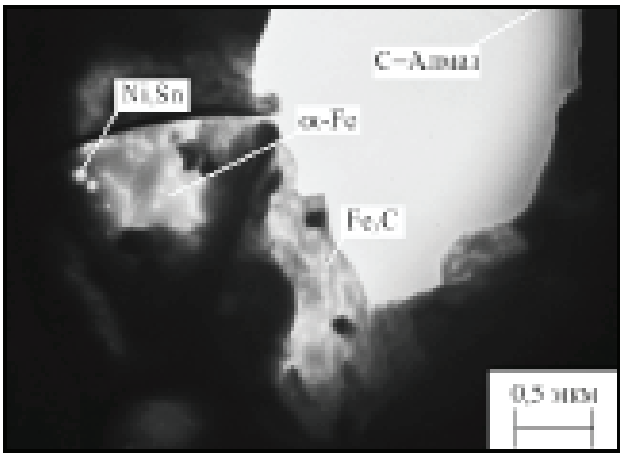

b

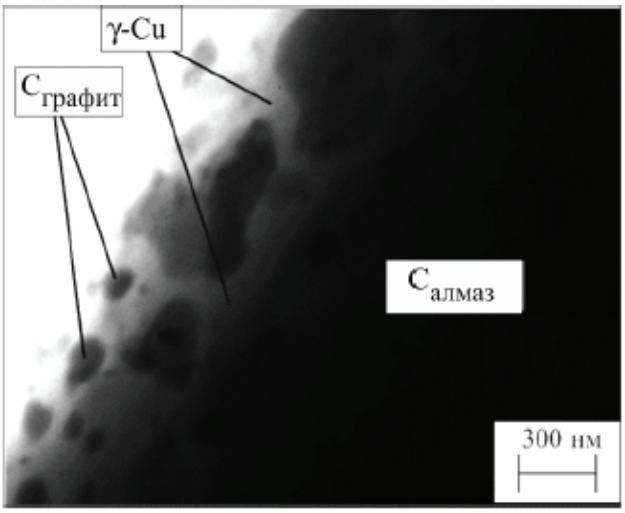

c

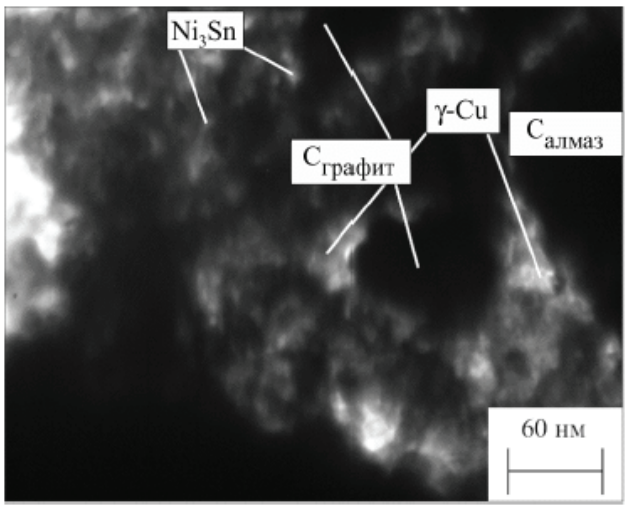

d

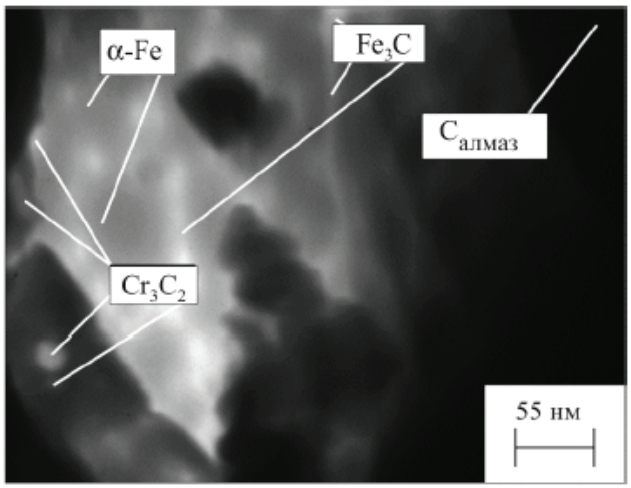

e

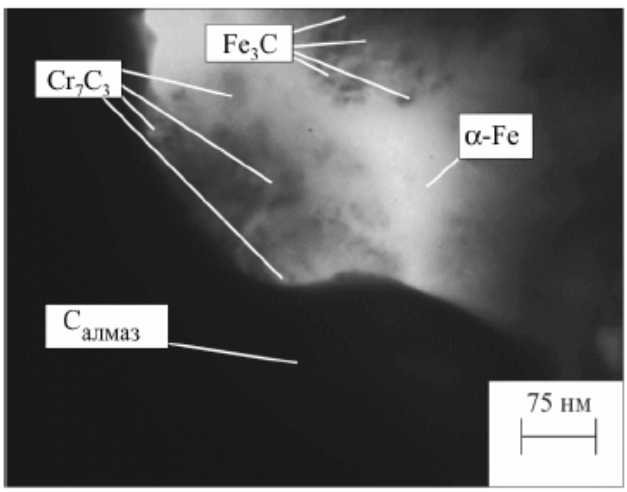

f

Fig. 5. TEM images of sections of the transition zone diamond-bond samples 5 (a), 8 (b), 9 (c), 10 (d), 11 (e), 12 (f), obtained by sintering in a mold in an oven at 800 C for 1 hour, followed by hot mounting pressing at: a) p = 100 MPa, t = 2 min; b) p = 100 MPa, t = 3 min; c) p = 100 MPa, t = 2 min; d) p = 100 MPa, t = 3 min; e) p = 200 MPa, t = 2 min; f) p = 200 MPa, t = 3 min.

metal bond in composites: diamond-(Fe-Cu-Ni-Sn-NbN) (samples 1-4), diamond-(Fe-Cu-Ni-Sn) (samples 5-8), diamond-(Fe-Cu-Ni-Sn-CrB2) (samples 9-12) and their impact on the tribological properties.

The comparison of the peculiar properties of the structure of the investigated samples diamond-(49,98Fe-31,36Cu-8,82Ni-7,84Sn-2NbN) (samples of the first type) and their analogues, diamond-(51Fe-32Cu-9Ni-8Sn) [7] (samples of the second type) and diamond-(49,98Fe-31,36Cu-8,82Ni-7,84Sn-2CrB2) (samples of the third type) [10, 11], obtained by sintering in the mold in an oven at a temperature of 800 C for 1 hour, followed by hot mounting pressing, shows that exist common identities as well as fundamental differences.

In particular, it is shown that the main phases of the metallic bond of DCM samples of the first, second and third types, obtained under identical conditions, are solid solutions based on iron and copper intermetallics Cu9NiSn3. It should be noted that the other phases in the metal bond samples of the first type are Cu10Sn3, NbN and Nb4N3, and Ni3Sn and Ni3Sn, CrB2 in second and third type, respectively. This means that the formation of phases in the system depends on the composition of the initial materials.

A fundamental difference of the structure of the DCM samples is the construction of the transition zone diamond-metal bond. Thus, the structure of the transition zone diamond-metal bond of the samples of the first type in dependence on the parameters of the hot mounting pressing, is consisting of phases Cu, NbN (see Fig. 4 a-d) and (or) α-Fe and NbN (see Fig. 4e,f) with complete absence of graphitic inclusions, cracks and micropores. Whereas, the structure of the transition zone diamond-metal bond of DCM samples of the second [14] and third [17, 18] types, differs substantially from the structure of the metallic bond, because to its formation affects the interaction of carbon which is obtained by the surface graphitization of diamond grains at the stage of sintering, with the solid phases. Thus, the structure of the transition zone of the sample 5, manufactured from the batch diamond-(51Fe-32Cu-9Ni-8Sn) at a pressure of 100 MPa and a holding time under pressure for 2 minutes, consisting of Cu, Ni3Sn phases with graphite inclusions (Fig. 5a). This is the reason for its destruction and premature loss of diamond grains with a metal bond, which reduces the wear resistance of DCM.

A distinctive feature of the structure of the transition zone in the sample 8, obtained from the same batch, at a pressure of 200 MPa, is the presence of Fe3C nanoscale layers and no graphite inclusions (Fig. 5b). This effect is due to the fact that the carbon which is formed in the surface graphitization of diamond grains at the stage of sintering the composition interacted with the solid phase α-Fe during its hot mounting pressing, by forming iron carbides. This in turn, provides the decarburization in the transition zone of the DCM sample, which can prevent premature failure of the transition zone and deposition (falling out) of diamond grains from the metal bond of the composite.

The transmission electron microscopy (TEM) data (presented in Fig. 5c-f), shows that the structure of the transition zone diamond-metal bond of DCM samples of third type (samples 9-12) also depends on technological parameters of the hot mounting pressing. Thus, the structure of the transition zone in the DCM samples (samples 9 and 10) obtained under insufficient pressure values (lower than 200 MPa) and with duration of the hot mounting pressing less than 3 minutes, is consisting of Cu, Ni3Sn phases with graphite inclusions (Fig. 5c, d), which serves the cause of its premature failure of the mechanism of intensive cracking and loss of diamond grains from the bond of the composite.

Whereas, the structure of the transition zone diamond-metal bond of DCM samples (samples 11 and 12) obtained under insufficient pressure values (lower than 200 MPa), consists of layers of carbides Fe3C, Cr3C2 and Sr7C3 with a nanometer thickness (Fig. 5e, f). Thus, in the transition zone of these samples there are no graphite inclusions, micro-cracks and pores. The mechanism of formation of

Table 6

The mechanical properties of the DCM samples

Sample	Pressure p, MPa	Duration of hot mounting pressing t, min	Microhardness H_b, GPa			Strength limits upon compressive R_{cm}, MPa	Strength limits upon bending R_{bm}, MPa
			Cu	Ni_3Sn	α-Fe		
1	100	2	2,82	–	3,67	758	754
2		3	2,84	–	3,80	790	781
3	200	2	2,95	–	4,20	856	830
4		3	3,35	–	4,40	890	880
5	100	2	2,50	2,63	2,93	710	610
6		3	2,61	2,67	3,16	720	625
7	200	2	2,70	3,05	3,42	800	635
8		3	2,79	3,33	3,74	826	650
9	100	2	2,60	3,76	2,93	730	640
10		3	2,70	2,82	3,46	750	645
11	200	2	2,80	3,03	3,96	780	655
12		3	2,92	3,48	4,12	840	675

these layers is explained due to the fact that carbon obtained by graphitizing the surface layer of diamond grains in the sintering compositions interacted with α-Fe and CrB2 under hot mounting pressing, forming iron and chromium carbides.

Thus, as a result of the conducted research, it was found that several factors affect to the formation of nanostructures in the transition zone diamond-metal bond sintered in mold in the oven at 800 C for 1 h of the composites diamond-(51Fe-32Cu-9Ni-8Sn). The main factors are: The composition of DCM, including the existence of hardening additives niobium nitride and chromium diboride, pressure and the duration of hot mounting pressing. It should be noted some advantages of this method for producing DCM compared with other methods. Firstly, the metal components of the composite in the initial state have sizes ranging ~ 5–50 μm, i.e. in our case the burnishing of powder mixtures do not require the use of nanoparticles in their composition, that reduces the possibility of oxidation of the initial materials in the process of batch burnishing at one hand, and on the other, it significantly reduces the cost of DCM.

Secondly, in the caseς of samples of the second and third type, that is, when occurs phase transformation diamond → graphite, carbon, which is formed in the surface graphitization of diamond grains under sintering the composition, ceases natural sources in improving mechanical and tribological properties of the DCM. Thirdly, the correct choice of introducing additives and technological parameters of hot mounting pressing is the key for obtaining DCM with useful new properties. Furthermore, during the formation of the DCM samples, occurs significant milling of the structural elements of the transition zone diamond-metal bond. To confirm these conclusions, studies regarding mechanical and tribological properties of the DCM, was carried out.

The results of determination of microhardness (Hv), strength limits upon compressive (Rcm) and upon bending (Rbm), of sintered at 800 C with a duration of 1 h in the mold in an oven followed by hot mounting pressing composites diamond-(49,98Fe-31,36Cu-8,82Ni-7,84Sn-2NbN) (samples of the first type) and their analogues, diamond-(51Fe-32Cu-9Ni-8Sn) (the samples of the second type) [14] and diamond-(49,98Fe-31,36Cu-8, 82Ni-7,84Sn-2CrB2) (examples of the third type) [17, 18], sintered in the same conditions as the samples of the first type, are shown in Table. 6. Analysis of the data showed, that the mechanical properties of the DCM samples depending from both, composition and technological parameters of their hot mounting pressing. Thus, by increasing pressure of hot mounting pressing of the composition diamond-(49,98Fe-31,36Cu-8,82Ni-7,84Sn-2NbN) (samples of the first type) from 100 to 200 MPa and the duration of the process from 2 to 3 minutes, is observed an increase in microhardness in the sections of the metal connection for the phase Cu from 2,82-2,84 GPa (samples 1 and 2) to 2,95-3,35 GPa (samples 3 and 4) and for the phase α-Fe from 2,67-3,80 GPa (samples 1 and 2) to 4,20-4,40 GPa (samples 3 and 4). This increases the value of strength limits upon compressive from 758 to 890 MPa and upon bending from 754 to 880 MPa. The mechanism of this improvement is likely consisting of the compacting of the structural components of the composite and, as a consequence, of the disappearance of pores at the interfaces boundaries, as well as in the boundary of the section diamond-metal bond.

A similar tendency in the dependencies on the mechanical characteristics and the duration of hot mounting pressing is preserved for the DCM samples of second type (samples 5-8), but their mechanical properties have smaller values than the samples of the first type. When administered chromium diboride to the composition diamond-(51Fe-32Cu-9Ni-8Sn), is observed a slight increase in strength properties (samples 9-12) in comparison to the samples

Table 7

The tribological properties of the DCM samples

Sample	Coefficient of friction, f		Massive wear Δm, g		Wear intensity I_m, g/Km	
	Burnishing	Testing	burnishing	Testing	burnishing	Testing
1	0,207	0,092	0,040	0,106	0,0236	0,0078
2	0,211	0,096	0,039	0,095	0,0229	0,0070
3	0,220	0,105	0,018	0,027	0,0106	0,0020
4	0,223	0,108	0,017	0,025	0,0101	0,0018
5	0,203	0,088	0,089	0,184	0,0518	0,0135
6	0,206	0,089	0,080	0,168	0,0471	0,0124
7	0,211	0,094	0,052	0,111	0,0306	0,0082
8	0,216	0,098	0,041	0,094	0,0241	0,0069
9	0,209	0,096	0,083	0,170	0,0488	0,0125
10	0,209	0,108	0,080	0,160	0,0470	0,0118
11	0,227	0,112	0,038	0,074	0,0223	0,0054
12	0,229	0,116	0,032	0,060	0,0188	0,0044

5-8.

The results of the tribological tests of the obtained DCM samples (coefficient of friction f, massive wear Δm, wear intensity Im) paired with an abrasive circle of electrocorundum are given in Table 7. The analysis showed that the tribological properties of the DCM samples, as well as the mechanical properties, are depending from the composition of the initial materials and the technological parameters of the hot mounting pressing. We note some differences in the nature of changes in the tribological properties of the DCM samples in dependence from their composition and technological parameters of hot mounting pressing and the duration of the experiment. It can be seen that after a period of burnishing (friction path 1,7 km), all DCM samples (samples 1-12) exhibit a relatively high coefficient of friction f (0,207-0,223), compared with values of the coefficient of friction f (0,092-0,116) after the testing period (friction path 13,6 km). This is due to the fact that the step of the burnishing of DCM characterized with an increased wear due to intense friction with the metal bond with the abrasive circle, since the diamond grains have no enough time to be exposed to a sufficient amount.

It was revealed that the tribological characteristics of the DCM samples after testing in two stages are depending on the parameters of hot mounting pressing. Thus, when pressure is increased from 100 to 200 MPa and a holding time under pressure from 2 to 3 minutes, there is observed some increase in the coefficient of friction f, from 0.092 to 0,108 and the reducing of the mass wear Δm from 0,040 to 0,017 g, as well as (is observed) the reducing of the Im from 0,0236 to 0,0101 g/km, for the samples of the first type after the burnishing period (friction path 1,7 km) (Table 7, samples 1 and 4). These data are in good agreement with the classical theory of wear, according to which the wear intensity of DCM naturally decreases by increasing the hardness of the metal bond. However, according to our data from TEM (Fig. 4) results that the main reason for increasing the wear resistance and strength properties of the samples of the first type is the distinction in the structure of the transition zone diamond-metal bond. Thus, from Fig. 4a, b could be clearly seen that the structure of the transition zone of the sample 1 is composed of Cu and NbN phases, and the structure of the transition zone of the sample 4, of α-Fe and NbN phases (Fig. 4 f). In this case we observed increase in the strength limits upon compressive Rcm from 758 to 890 MPa and upon bending Rbm from 754 to 880 MPa (tab. 6, samples 1 and 4) and the increase of the wear resistance of the composite is 2,3 times (Table 7, samples 1 and 4). This in turn provides an improved retention of the diamond grains and the metal bond and, as a consequence, increases the wear resistance of the DCM. With increasing friction paths from 1,7 to 13,6 km, it is observed a decrease in the coefficient of friction f and in the wear intensity Im, at the testing, for the DCM samples. This process is most notably expressed at the sample 4 for which the coefficient of friction f, the mass wear Δm and the wear intensity Im are reaching the values 0,088, 0,025 and 0,0018, respectively. These data, once more, show that the structural phase state of the transition zone diamond-metal bond is the main reason for the increase of the wear resistance of the DCM.

The schematic picture of wear of the DCM 5-8 samples (samples of the second type) under friction, implemented in our experiments, is not changed comparing to DCM 1-4 samples (samples of the first type). However, the deterioration (wear) of these DCM is developing more intensively. Thus, by increasing the pressure of the hot mounting pressing of the composition diamond-(51Fe-32Cu-9Ni-8Sn) from 100 to 200 MPa and the duration of the process from 2 to 3 minutes, is observed a decrease of mass wear Δm and in wear intensity Im for the burnishing stage, from 0,089 to 0,041 g and from 0,0518 to 0,00241 g/km respectively (Table 7, samples 5 and 8). With increasing friction path from 1,7 to 13,6 km it was also observed a decrease in the values of the mass wear Δm and the wear intensity Im from 0,184 to 0,094 g, and from 0,0135 to 0,0069 g/km, respectively. Such a process of deterioration is also related mainly to the structure of the transition zone diamond-metal bond. Analysis of Fig. 5b shows that the structure of the transition zone of sample 8 obtained at a pressure of 200 MPa, consist of the phases α-Fe and layers Fe3C of nanoscale thickness in the absence of graphitic inclusions. Whereas the structure of the transition zone of the samples 5 and 6 are obtained at a lower pressure of hot mounting pressing (100 MPa), consists of the phases Cu and Ni3Sn with graphite inclusions (Fig. 5a), which is the reason for its premature failure of the mechanism of intensive cracking and deposition of diamond grains from the metal bond.

For the samples of third type (samples 9-12) effect of reducing the mass wear Δm and the wear intensity Im when the pressure of the hot mounting pressing increases, is expressed more strongly in comparison with the samples of the second type (samples 5-8). Thus, by increasing the pressure of the hot mounting pressing from 100 to 200 MPa and the holding time under pressure from 2 to 3 min, is observed a decrease of the wear mass Δm and of the wear intensity Im for DCM samples after their testing stage at burnishing step from 0,083 to 0,032 g and from 0,0488 to 0,0188 g/km, respectively (Table 7, samples 9 and 12). With increasing friction path from 1,7 to 13,6 km, the values of the wear mass Δm and of the wear intensity Im decreases from 0,170 to 0,060 g and 0,0125 to 0,0044 g/km, respectively (Table 7, samples 9 and 12). The effect of improving the wear resistance of the sample 12 as compared with sample 9, is explained due to the presence of nanostructure Fe3C, Cr3C2 and Sr7C3 without graphite inclusions in the first (Fig. 5e, f), which is providing the increase of the strength

limits upon compressive (Rcm) from 730 to 840 MPa and upon bending (Rbm) from 640 to 675 MPa. Whereas the structure of the transition zone of samples 9 and 10 consists of phases Cu, Ni3Sn with graphite inclusions (Fig. 5c, d), which reduces the mechanical properties of such DCM (Table 7). The mechanism of formation of the nanostructure in the transition zone of DCM samples 11 and 12, is explained due to the fact that the carbon which is formed during the surface graphitization of the diamond grains at the stage of sintering of the composition, is interacted with the solid phase α-Fe and CrB2 during its hot mounting pressing, forming carbides of iron and chromium. This in turn, leads to decarburization of the transition zone and improves the mechanical properties of DCM.

Thus, the analysis of the data show that the introduction of additives CrB2 into the composite diamond-(51Fe-32Cu-9Ni-8Sn) leads to lower wear intensity Im of DCM from 0,0069 to 0,0044 g/km (Table 9, samples 8 and 12, respectively), which provides an increase of the wear resistance by 1,6 times. Even more pronounced effect of enhancing the wear resistance (by 2,6 times) is observed when we use NbN additives, which is associated with the formation of two-phase structure of the transition zone (α-Fe and NbN phases) with reduced fragility parameters and more milled grains, as well as the formation of a metal bond structure with increased strength parameters. The observed important effect of the formation of a special structure of the transition zone in the DCM system diamond-(Fe-Cu-Ni-Sn), points out the necessity to continue these studies, in order to establish the generality of this effect for DCM of other systems, to obtain direct evidence of the effect of additives NbN, CrB2 and (or) other additives of transition metals on the formation of the structure, with which are mainly related physical-mechanical and operational properties of the DCM. It should be noted that is observed correlation between the structure of the transition zone diamond-metal bond and the wear resistance of DCM [7].

Conclusions

In this work, the changes in the structure of the transition zone diamond-metal bond and metal bond in the compositions diamond-(49,98Fe-31,36Cu-8,82Ni-7,84Sn-2NbN), diamond-(49,98Fe-31,36Cu-8,82Ni -7,84Sn-2CrB2) and diamond-(51Fe-32Cu-9Ni-8Sn) after sintering in the mold in the oven at 800 C for 1 hour, in dependence from the p-t parameters of hot mounting pressing and their influence on physical -mechanical and tribological properties of sintered composites was investigated.

1. It was found that the metal bond of the composite diamond-(49,98Fe-31,36Cu-8,82Ni-7,84Sn-2NbN) regardless of the technological parameters of hot mounting pressing, consists of solid solutions based on iron and copper of variable composition and phases Cu10Sn3; Cu9NiSn3, Nb4N3, NbN, and the transition zone diamond-metal bond in dependence from the hot mounting pressing may consist of phases Cu; NbN and (or) α-Fe; NbN, as well as of the combination of these phases.

2. It was established that by increasing the pressure from 100 to 200 MPa and the hot mounting pressing from 2 to 3 minutes of the composition diamond-(49,98Fe-31,36Cu-8,82Ni-7,84Sn-2NbN) after sintering in the mold in an oven at 800 C for 1 hour, is providing a 4,3 times increase of the wear resistance of the composites due to the increase of the microhardness of the bond sections for the phases Cu from 2,85 to 3,35 GPa, for the α-Fe from 3,67 to 4,40 GPa, for the strength limit upon compressive from 758 to 890 MPa and for the strength limit upon bending, from 754 to 880 MPa. This is in agreement with the change in the phase composition, the morphology of the phase components and the structure of the composite.

3. It is shown that composite sample diamond-(49,98Fe-31,36Cu-8,82Ni-7,84Sn-2NbN) have abrasive wear resistance higher than composites diamond-(51Fe-32Cu-9Ni-8Sn) 3,8 and 2,4 times more than the samples diamond-(49,98Fe-31,36Cu-8,82Ni-7,84Sn-2CrB2), obtained in the same conditions. Herewith in the composite of metal bond occurs milling of the elements of the structure, which is accompanied by the disappearance of the pores at the interphase boundaries.

4. Different character of the wear of the studied DCM is explained due to the fact that the interaction of the elements in dependence from the type of additive in the process of the formation of the composition takes place in different ways and has different effects on the structure and properties:

- The increase of the wear resistance of DCM samples of second and third types is due to the formation of the transition zone diamond-metal bond of nanostructure respectively from Fe3C and Fe3C, Cr3C2 and Sr7C3, as the result of the interaction of the carbon, which is released at the surface graphitization of diamond grains in the sintering phase of the composition with solid phases α- Fe and CrB2 during the hot mounting pressing, which helps to improve the adhesion properties at the boundary of the diamond-bond section.

- The increase of the wear resistance of DCM samples of the first type (samples diamond-(49,98Fe-31,36Cu-8,82Ni-7,84Sn-2NbN)) is explained by the formation of a longer lasting (stronger) contact on the boundary diamond-metal bond section by the hard compression of the diamond grains by α-Fe and NbN particles whereas milling the elements of the structure to nanoscale sizes. The mechanism of this process has not yet been studied, which is of interest for further research.

Legend (Notation)

P, is pressure of the hot mounting pressing; t, is the duration of the hot mounting pressing; a, b, c are the

lattice parameters; (hkl), is lattice indices; di, is interplanar distance; θ, is the diffraction angle; Ii, is the relative intensity of reflexes; Hv, is microhardness; Rcm, is the strength limit upon compressive; Rbm, is strength limit upon bending; f, is the coefficient of friction; L, is the friction path; Δm , is the mass wear; Im, is the wear intensity

References

1. Bondarenko N.A, Zhukovsky A.N ,Mechnik V.A Basics diamond composite materials for cutting tool. K .: ISM them. V.N Bakul NAS 2008.
2. Maystrenko A.L Formation of structure of composite diamond-containing materials in production processes. K .: Naukova Dumka. 2014.
3. Novikov N.A, Bondarenko N.A, Mechnik V.A Zhukovsky A.N Physical and mathematical modeling of sintering of diamond multicomponent compositions. 1. Mathematical model. // Fiz. - 2004 (7), № 3, 71-77.
4. Novikov N.A, Bondarenko N.A, Kulik O.G Mechnik V.A Zhukovsky A.N Physical and mathematical modeling of sintering diamond multicomponent compositions. 2. Physical and chemical features of formation of structure and properties. // Fiz. - 2004 (7), № 3, 79-87.
5. Funayama N and Matsuda J. Development of High-Performance cBN and Diamond Grinding Wheels for High-Speed Grinding. // New Diamond and Frontier Carbon. 2005 (15), No. 4, 173-180.
6. Sano S, Iwai M, Uematsu T and Suzuki K. Application of Polycrystalline Diamond (PCD) to EDM // Japan Society of Electrical-Machining Engineers , 2008 (42), No. 100, 2008, 65-72. doi: 10.2526 / jseme.42.65.
7. Ensinger W. Formation of Diamond-Like Carbon Films by Plasma-Based Ion Implantation and Their Characterization // New Diamond and Frontier Carbon.,2006 (16), No. 1, 1-31.
8. Shao W. Z., Ivanov V. V., Zhena L., Cuia Y. S. and Wanga Y. A Study on Graphitization of Diamond in Copper / Diamond Composite Materials // Materials Letters. 2004 (58), No. 1-2, 146-149. doi: 10.1016 / S0167-577X (03) 00433-6.
9. Chen Y., Jia X., Zhao G and Wang X. Facile Preparation of Cubic Calcium Carbonate Nanoparticles with Hydrophobic Properties via a Carbonation Route // Powder Technology. 2012 (200), No. 3, 144-148. doi: 10.1016 / j.powtec.2010.02.017.
10. Mizuuchi K., Inoue K., Agari Y., Yamada S., Sugioka M., Itami M., Kawahara M. and Makino Y. Consolidation and Thermal Conductivity of Diamond Particle Dispersed Copper Matrix Composites Produced by Spark Plasma Sintering (SPS) // Journal of the Japan Institute of Metals. 2007 (71), No. 11, 1066-1069. doi: 10.2320 / jinstmet.71.1066.
11. Petrovic M., Ivankovic A. and Murphy N. The Mechanical Properties of Polycrystalline Diamond as a Function of Strain Rate and Temperature // Journal of the European Ceramic Society. 2012 (32), No. 12, 3021-3027. doi: 10.1016 / j.jeurceramsoc.2012.03.026.
12. Mechnik V.A. Diamond composite materials Fe-Cu-Ni-Sn with stable characteristics //physical-chemical and materiales of mechanik.//2012.№ 5, 34-42.
13. Mechnik V.A. Obsession diamond composite material Fe-Cu-Ni-Sn with high wear // Powder metallurgy.2013.№ 9/10, 115 - 127.
14. Mechnik V.A. Evaluation diamond structure with metal bending Fe-Cu-Ni-Sn and diamond to Fe-Cu-Ni-Sn-CrB2 // Physics and chemical solid materials. 2013. T.14, №4. P. 857-868.
15. Mechnik V.A Impact assessment carbon interaction with compounds boride, nitride i silitside on the structure and diamond properties with binding of Fe-Cu-Ni-Sn // Problems of mechanical engineering. 2011 (11), № 5, 72-75.
16. Mechnik V.A. Effect of additives CrB2, TiB2 i WC on the diamond microstructure with Fe-Cu-Ni-Sn binding: receipt, properties, using // Physical Surface Engineering. 2013. (11), №4, 378-392.
17. Mechnik V.A. Laws creating structure in diamond systems Fe-Cu-Ni-Sn-CrB2 // Physical-chemical of materials mechanik. 2013, № 1, 85-92.
18. Mechnik V.A. Influense of tehnologichal parameters of hot pressing and madding of structure diamond with binder Fe-Cu-Ni-Sn-CrB2 // Powder metallurgy. 2013, № 11/12, 123-138.
19. Refractory connection: Right. / Ed. G.V Samsonov, I.M Vinnitsky .M .: Metallurgy, 1976.
20. V.V Skorokhod, A.V Ragulya Sintering at a controlled rate as the ceramic microstructure and management of such sintered materials // Powder metallurgiya.1994, №3 / 4, 1-10.
21. Skorokhod V.V, Uvarova I.V, Ragulya A.V Physical-chem. kinetics in nanostructured systems. K .: Akademperiodika, 2001.
22. V.V Skorokhod, A.V Ragulya nanostructured ceramics and nanocomposites: Achievements and Prospects // Advanced materiales and technology. At 2 m. / National Academy of Sciences of Ukraine. Vid-nya fiz.-tehn. probl. Science of materials K .: HP Akademperiodika , 2003.T.2, 7-34.
23. Andrievsky R.A Nanomaterials: Concept and modern problems // Russian. Chemical Magazin, 2002 Vol. 46, number 5, 50-55.
24. Kraus W. and Nolze G. Powder Cell . A program for the representation and manipulation of crystal structures and calculation of the resulting X-ray powder patterns // J. Appl. Cryst.1996.No. 29.P. 301-303.
25. Selected powder diffraction data for education straining (Search manual and data cards). Published by the Internatoinal Centre for diffraction data. USA. 1988. 432 p.
26. Chichinadze A.V,Brown E.D, Bush N.A., et al. Fundamentals of tribology (friction, wear, lubrication)- Engineering.-2001.

Вісник ХНУ, серія «Фізика», вип. 25, 2016. с. 43-47

УДК 538.945+537.312.62
PACS: 74.72.-h Cuprate superconductors.

Peculiarities of the relaxation processes in $ReBa_2Cu_3O_{7-x}$ (Re = Y, Ho) single crystals at room temperature in air atmosphere

Yu. I. Boyko, V. V. Bogdanov, R. D. Markov, R. V. Vovk

V. N. Karazin Kharkiv National University, 4 Svobody sq., 61077 Kharkiv, Ukraine

The time dependencies of the resistivity of $ReBa_2Cu_3O_{7-x}$ (Re =Y, Ho) single crystals with varying degree of deviation from oxygen stoichiometry was investigated. It was found that the accelerated transport of oxygen ions in the initial stage of the implementation process can be carried out along the one-dimensional non-stoichiometric vacancies' clusters in single file diffusion regime. The final stage of oxygen ions diffusion in $ReBa_2Cu_3O_{7-x}$ (Re = Y, Ho) is described by the usual classical diffusion mechanism.

The substitution of yttrium by holmium significantly affects the charge redistribution and changes the efficient interaction of ions in CuO-planes, thereby modifying the diffusion mass transfer mechanisms in the oxygen subsystem. Thus there is a change in the duration of the time intervals, corresponding to the oxygen ions' single file and classical volume diffusion mechanisms.

Keywords: $ReBa_2Cu_3O_{7-x}$ single crystals; doping; oxygen diffusion kinetics; structural relaxation processes; single file diffusion.

Досліджено залежності від часу величини електроопору монокристалів $ReBa_2Cu_3O_{7-x}$ (Re = Y, Ho) з різним ступенем відхилення від кисневої стехіометрії. Показано, що прискорений транспорт іонів кисню на початковій стадії процесу впровадження реалізується уздовж одновимірних скупчень нестехиометрических вакансій механізмом одноканальній дифузії (single file diffusion). Заключна стадія впровадження іонів кисню в $ReBa_2Cu_3O_{7-x}$ (Re = Y, Ho) описується класичним механізмом об'ємної дифузії.

Заміна ітрію на гольмій істотно впливає на перерозподіл заряду і змінює ефективну взаємодію іонів в CuO-площинах, тим самим, модифікуючи дифузійне перенесення речовини в кисневій підгратці. При цьому відбувається зміна тривалості часових інтервалів, відповідних механізмів одноканальної і об'ємної дифузії іонів кисню.

Ключові слова: монокристали $ReBa_2Cu_3O_{7-x}$; допування; кінетика дифузії кисню; релаксаційні процеси; одноканальна дифузія.

Исследованы зависимости от времени величины электросопротивления монокристаллов $ReBa_2Cu_3O_{7-x}$ (Re =Y,Ho) с различной степенью отклонения от кислородной стехиометрии. Показано, что ускоренный транспорт ионов кислорода на начальной стадии процесса внедрения реализуется вдоль одномерных скоплений нестехиометрических вакансий механизмом одноканальной диффузии (single file diffusion). Заключительная стадия внедрения ионов кислорода в $ReBa_2Cu_3O_{7-x}$ (Re = Y, Ho) описывается классическим механизмом объемной диффузии.

Замена иттрия на гольмий существенно влияет на перераспределение заряда и изменяет эффективное взаимодействие ионов в CuO-плоскостях, тем самым, модифицируя диффузионный перенос вещества в кислородной подрешетке. При этом происходит изменение длительности временных интервалов, соответствующих механизмам одноканальной и объемной диффузии ионов кислорода.

Ключевые слова: монокристаллы $ReBa_2Cu_3O_{7-x}$; допирование; кинетика диффузии кислорода; релаксационные процессы; одноканальная диффузия.

Introduction

Study of mass transfer processes [1,2], along with the research of charge and heat transfer processes [3-5] are important tools to understand the nature of high-temperature superconductivity (HTSC), which still remains unclear, despite the more than 30-year intensive experimental and theoretical investigations.

Notably, in HTSC compounds the diffusion processes, in addition to the classical thermally activated mechanism [1,2], can be relatively affected by the application of high pressure [6,7], and intensively occur at "aging" of the experimental samples [8-10]. Thereby, the mass transfer can be carried out by a number of specific mechanisms: single-file diffusion, upward diffusion, and others [2,11,12,13].

The $YBa_2Cu_3O_{7-x}$ crystal is a well-known and one of the most studied ionic compounds regarding the so called "high-temperature" superconductivity [14]. An important feature of the structural state of this crystal is the presence in its lattice of one-dimensional ordered clusters formed by oxygen vacancies [13]. The formation of such structural defects due to the layered nature of the crystal lattice of the compound, as well as deficiency of oxygen ions, characterized by a parameter (x). The superconducting properties of the $YBa_2Cu_3O_{7-x}$ system (for example the transition

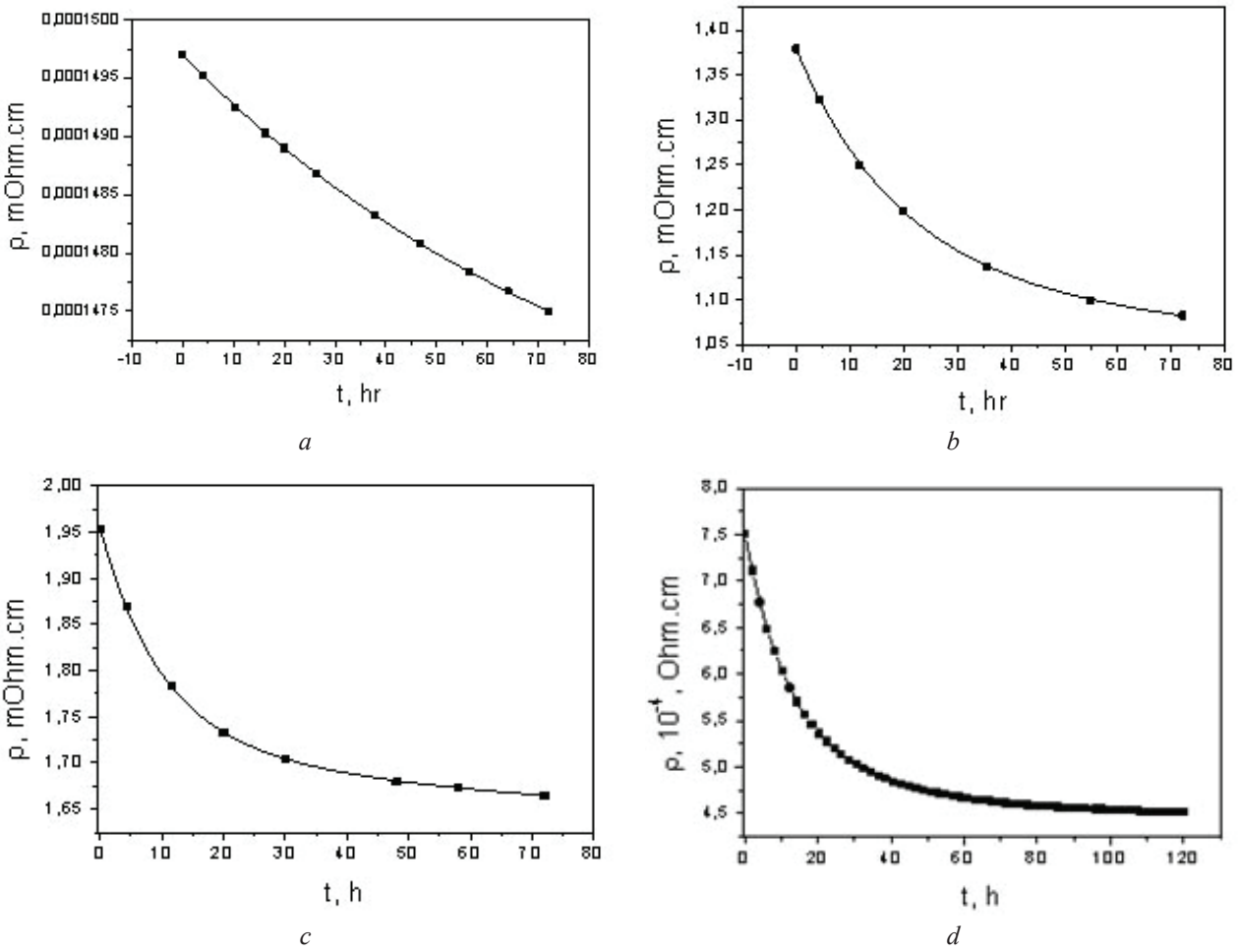

Fig. 1. The dependence of electrical resistivity of K1-K4 single crystals from the time of exposure in air at room temperature a – YBaCuO (T_c = 92 K); b – YBaCuO (T_c = 48 K); c – YBaCuO (T_c = 42 K); d – HoBaCuO (T_c = 73 K).

temperature to the superconducting state T_c, the electrical resistivity ρ, the critical current density J_c) are essentially depend on the degree of filling of vacancy clusters by oxygen ions, ie. on the value of the parameter (x). Thus, for example, when the value of (x) changes from ≈ 0.1 to ≈ 0.4, a decrease for the T_c is observed from $T_c \approx 92$ K to $T_c \approx$ 50 K, and when the value (x) ≥ 0.5, the superconductivity in this crystal disappears [15]. Similar dependencies from the value of (x) are also observed during the investigation of other characteristics of the $YBa_2Cu_3O_{7-x}$ system. This is associated with the formation of one-dimensional chains of oxygen ions (clusters) that are formed as the clusters of vacancies are filled. Oxygen clusters together with Cu ions form the so-called U-centers that are capable to generate coupled electric charge carriers [16].

Formation of clusters occurs by the diffusion of oxygen ions during high temperature annealing of crystal in an oxygen atmosphere. As evidenced by the results of [2], the diffusion filling of the $YBa_2Cu_3O_{7-x}$ crystal by oxygen ions takes place by two different mechanisms. At the initial stage when we have a large deficit of oxygen ions ((x) ≥ 0.4) the process of filling of the crystal lattice by oxygen ions occurs in the regime of "single file" diffusion [17]. This accelerated transport of oxygen ions is replaced by the usual classical volume diffusion mechanism at the final stage of the process, when the parameter (x) → 0.1. Based on this fact, it is natural to assume that many of the relaxation processes observed in the crystal at room temperature, can also be controlled by these mechanisms of oxygen ions diffusion.

As is known [15,18], a characteristic feature of $YBa_2Cu_3O_{7-x}$ compound is the relative simplicity of the full or partial substitution of the yttrium by rare-earth ions. Thus, as in the case of other rare earth elements, when implementing the substitution of Y by the paramagnetic ions Re = Ho, Dy, the superconducting properties of the optimally oxygen doped of the $ReBa_2Cu_3O_{7-x}$ compounds with (x) ≤ 0.1, do not change significantly [15]. Apparently this is due to the localization of these ions away from the superconducting planes, which, in turn, prevents the formation of long-range magnetic order. At the same time it is known that the samples of the HTSC system 1-2-3, with non-stoichiometric composition regarding the oxygen, the rare earth ion may serve as a "sensor", sensitive to the local symmetry of its environment and to the charge density distribution, since the change in these parameters affect the

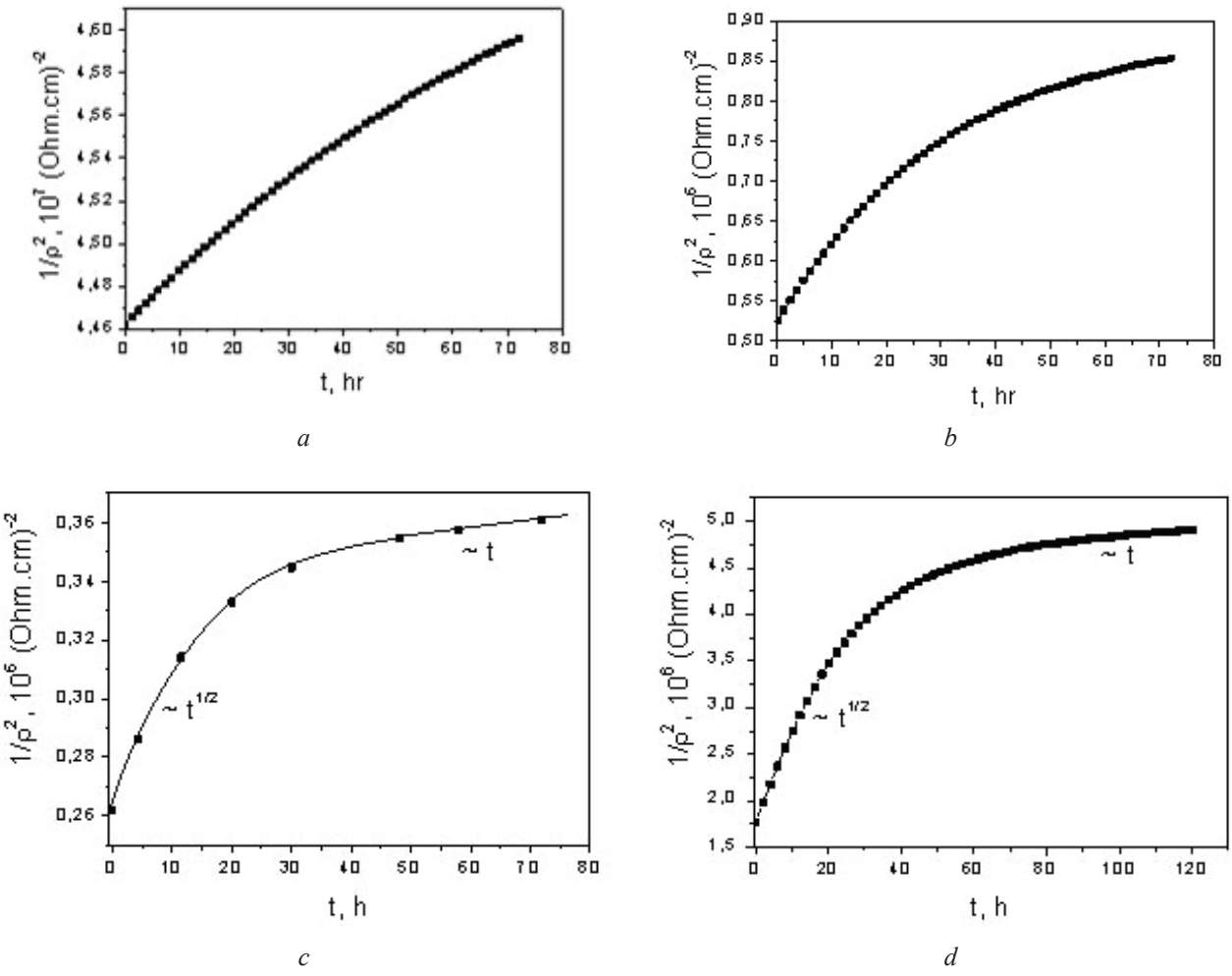

Fig. 2. The plot of $1/\rho^2 = f(t)$ dependence for K1-K4 single crystals. The designations correspond to figure 1 a – YBaCuO ($T_c = 92$ K); b – YBaCuO ($T_c = 48$ K); c – YBaCuO ($T_c = 42$ K); d – HoBaCuO ($T_c = 73$ K).

electric field that forms the electronic structure of the ion [1,19]. Notably, in $HoBa_2Cu_3O_{7-x}$ the oxygen self-diffusion processes is affected by the larger holmium atom, leading to a change of the oxygen ions interaction in the CuO-planes [20].

Oxygen is sufficiently contained in the conventional air atmosphere in which usually-most of the crystals are stored. To verify the legitimacy of the assumptions made, we investigate the relaxation of the electrical resistance of four $ReBa_2Cu_3O_{7-x}$ (Re = Y, Ho) single crystals that were kept for a long time (more than three days) at room temperature in air atmosphere. Presentation of the results of this study and their discussion is devoted to this article.

Experimental methodology

The $ReBa_2Cu_3O_{7-x}$ (Re = Y, Ho) single crystals were grown by the gold crucible solution-melt technology as described in previous work [21]. For the resistive measurements four crystals: K1, K2, K3 ($YBa_2Cu_3O_{7-x}$) and K4 ($HoBa_2Cu_3O_{7-x}$) have been used. Measurement of the electrical resistance of the samples was carried out by the standard four-point scheme using two pairs of silver contacts. The measurements were performed in the drift mode for two opposite directions of transport current to eliminate the impact of interference signal. The temperature was measured by platinum thermistor, the voltage on the sample and the control resistance by V2-38 nano-voltmeters. The critical temperature was determined at the maximum point on the dρ/dT curves in the region of the superconducting transition.

To reduce the oxygen content the samples were annealed for a day at temperature 680 ^{0}C and 690 ^{0}C ($YBa_2Cu_3O_{7-x}$ samples) and 600 ^{0}C ($HoBa_2Cu_3O_{7-x}$ sample) in vacuum. After annealing, the crystals were cooled until room temperature for 2-3 minutes. Then, they were mounted in the measuring cell and cooled until liquid nitrogen temperature for 10-15 minutes. All measurements were performed as the sample heating. To investigate the effect of annealing at room temperature, the sample after the first measurement of ρ(T), was held for several hours at room temperature and repeated measurements were performed. This procedure was repeated several times. The last series of measurements was carried out after the total exposure of the sample at room temperature for 5 days.

Results and discussion

The results of these measurements are presented in Fig. 1. As in previous work [2], we can clearly observe the two-stage process of the resistivity reducing with the exposure time. At the initial stage (approximately 20 hours), accelerated kinetics took place, which is replaced by a slower one, emerging to the saturation at up to three days exposure.

To identify the physical nature of this result, as in [2], we used the fact that at room temperature and above, the $YBa_2Cu_3O_{7-x}$, $(x) = 0.6$, is a common semiconductor. Accordingly, an increase in oxygen ions concentration causes an increase in the electrical conductivity and the corresponding decrease in the electrical resistivity ρ. At the same time, the change in the oxygen concentration in the crystal with time t is described by the same law as the average displacement of the diffusing oxygen ions into the crystal: $<L> = (2Dt)^{1/2}$ (where D is the diffusion coefficient) [22]. Consequently, we can determine from the time dependence $(1/\rho^2) = f(t)$ the time dependence of the mean square displacement of oxygen ions in the process of their diffusion penetration in crystal $<L^2> = f(t)$. In turn, the $<L^2> = f(t)$ dependence defines the ion diffusion mechanism: the $<L^2> \sim t^{1/2}$ dependence corresponds to a single file diffusion, and the dependence $<L^2> \sim t$ is consistent with the common classical volume diffusion [17]. Using the experimental data presented in figure 1, we processed them by using the $(1/\rho^2) = f(t)$ dependence (see. Fig. 2). From this figure it follows that the initial stage of the relaxation process $\rho = f(t)$ is controlled by a single file diffusion mechanism, and at the final stage of this process occurs in the classical diffusion regime.

At the same time it can be seen that the duration of the first stage greatly depends on the oxygen concentration in the sample, and on the type of the rare-earth ion. In the $YBa_2Cu_3O_{7-x}$ single crystals the longest stage of the $<L^2> \sim t^{1/2}$ dependence corresponding the single file diffusion is observed in the sample with the minimum $T_c \approx 42$ K (and, accordingly, with the maximum oxygen deficiency). With the increase of T_c up to 48 K (and, accordingly, as the oxygen deficiency is reduced), in crystal K2, the duration of this stage decreases and reaches to the minimum in the sample with $T_c \approx 90$ K. This result confirms the formulated our assumption that the process of filling of crystal lattice with oxygen ions in the single file diffusion regime is most easily implemented in the samples with its maximum oxygen deficiency $(x) \leq 0.4$, whereas the conventional classical mechanism dominates at $(x) \rightarrow 0.1$.

It is observed that in the case of $HoBa_2Cu_3O_{7-x}$ crystal, despite the relatively high $T_c \approx 73$ K, the single file diffusion is the dominant regime. As noted above, in the case of the Y substitution by other rare-earth elements, there is no significant change occurring regarding the electrical characteristics in the optimally doped samples $(x) < 0.15$. At the same time, as shown in [23], all the characteristic changes in the shape of the temperature dependence of the resistivity and the absolute values of the resistivity parameters that were observed during isobaric annealing of the samples at room temperature in the case of $HoBa_2Cu_3O_{7-x}$ compounds, carried a much more pronounced character in comparison with the $YBa_2Cu_3O_{7-x}$ samples. As mentioned above, in the case of $HoBa_2Cu_3O_{7-x}$ samples, a specific role in the structural ordering in the system is due to yttrium substitution by holmium, which has a much larger ionic radius, which, in turn, leads to a change in the oxygen ions' interaction in the CuO-planes. Indeed, as is known from previous studies [19], when the yttrium substituted by other rare earth elements with larger ion radius, there occurs a significant qualitative changes in $T_c(x)$ dependence. Thus, the characteristic for the $YBa_2Cu_3O_{7-x}$ dependence T_c (x) with two plateaus at 60 and 90 K degenerates into a much sharper monotonic dependence [19]. So, we can assume that in the case of deviation from oxygen stoichiometry the $HoBa_2Cu_3O_{7-x}$ compound should be characterized by a much more unstable oxygen superstructure in comparison with the $YBa_2Cu_3O_{7-x}$. This, in turn, can significantly affect to the diffusion mechanisms and the nature of the diffusion processes in the samples that we observed in the experiment. A certain role in this case may also play the specific mechanisms of quasi-particle scattering [24-29], due to the presence structural and kinematic anisotropy in the system.

It should be emphasized that and some other relaxation processes that are observed in the high-temperature oxide superconductors can also be described by similar kinetic laws. As an example, we can mention the time dependence of the temperature in which the pseudo-gap opens (T*), during exposure of the sample at room temperature in air atmosphere [23] as well as the two-stage relaxation of the electrical resistance of single crystals $YBa_2Cu_3O_{7-x}$ in the process of high hydrostatic pressure-induced redistribution of the labile oxygen [30].

Conclusions

Based on this study we can conclude that in all high-temperature oxide superconductors, characterized by oxygen ions deficiency, and in particular, in the $YBa_2Cu_3O_{7-x}$ compounds, the relaxation of the electrical resistivity at room temperature that is observed, is controlled by the single file and the classical oxygen ions volume diffusion mechanisms. The substitution of yttrium by the holmium significantly affects the charge redistribution and change the interaction of oxygen with the CuO-planes, thereby modifying the diffusive transport of matter in the oxygen sublattice. Thus, there occurs a significant shift of the time intervals corresponding to the single file and the classical oxygen ions volume diffusion mechanisms.

References

1. Marion Klaser, Joachim Kaiser, Fredy Stock, German Muller-Vogt, Andreas Erb / Physica C 306 (1998) 188-198.
2. Yu.I.Boyko, V.V.Bogdanov, G.Ya. Khadzhai, S.V.Savich, R.V.Vovk / FNT, v. 42, N10, 2016.
3. J. Ashkenazi, J. Supercond. Nov. Magn. 24, 1281 (2011).
4. R. V. Vovk, M. A. Obolenskii, A. A. Zavgorodniy, Z. F. Nazyrov, I. L. Goulatis, V.V. Kruglyak, A. Chroneos / Modern Physics Letters B (MPLB) V. 25 (27), p. 2131-2136 (2011).
5. R. V. Vovk, G.Ya. Khadzhai, I. L. Goulatis, A. Chroneos / Physica B: Condensed Matter Volume 436, 1 March 2014, Pages 88–90.
6. S. Sadewasser, J.S. Schilling, A.P. Paulicas, B.M. Veal // Phys. Rev. B. -2000. -V.61, №1. -P.741-749.
7. D.D. Balla, A.V. Bondarenko, R.V. Vovk, M.A. Obolenskii, A.A. Prodan // Low Temp. Phys. - 1997. – Vol. 23, №10. - P. 777-781.
8. Martinez, B. Sandiumenge, F. ; Pinol, S. ; Vilalta, N. ; Fontcuberta, J. ; Obradors, X. // Applied Physics Letters (1995) V. 66 , Issue: 6 P.P. 772 – 774.
9. D. A. Lotnyk, R. V. Vovk, M. A. Obolenskii, A. A. Zavgorodniy, J. Kováč, M. Kaňuchová, M. Šefciková, V. Antal, P. Diko, A. Feher, A. Chroneos // Journal of Low Temperature Physics, DOI 10.1007/s10909-010-0198-z. Journal of Low Temperature Physics V. 161, № 3-4, 387-394, (2010).
10. R.V. Vovk, N.R. Vovk, G.Ya. Khadzhai, Oleksandr V. Dobrovolskiy, Z.F. Nazyrov / J Mater Sci : Mater Electron (2014) 25: 5226-5230 DOI 10.1007/s10854-014-2292-5.
11. Solovjov, M. Tkachenko, R. Vovk, A. Chroneos / Physica C 501 (0) (2014) 24 – 31.
12. Chroneos and R. V. Vovk / Solid State Ionics 274 (2015) 1-3.
13. Esch F., Fabris S., Zhou L., Montini T., Africh C., Fomasiero P., Comelli G., Rosei R. / Science, v. 309, p. 752, 2005.
14. M. K. Wu, J. R. Ashburn, C. J. Torng, P. H. Hor, R. L. Meng, L. Gao, Z. J. Huang, Y. Q. Wang, and C. W. Chu / Phys. Rev. Lett.58 (9) p.p. 908–910 (1987).
15. D. M. Ginsberg (ed), Physical properties high temperature superconductors I. – Singapore: Word Scientific, 1989.
16. K.Mitsen, O.Ivanenko, J. Exp. Theor. Phys, 100, 1082 (2005).
17. Hahn K., Karger J., Kukla V. / Physical Review, Letters, v. 76, № 15, p. 2762, 1996.
18. R.V. Vovk, N.R. Vovk, G.Ya. Khadzhai, I.L. Goulatis, A. Chroneos / Solid State Communications, V. 190, (2014), P. 18–22.
19. Lutgemeier H., Schmenn S., Meuffels P., Storz O., Schollhorn R., Niedermayer Ch., Heinmaa I., Baikov Yu. Physica C **267**, 191 (1996).
20. R.V. Vovk, G.Ya. Khadzhai, Oleksandr V. Dobrovolskiy, Z.F. Nazyrov, and A. Chroneos // Physica C 516 (2015) p.p. 58-61 doi:10.1016/j.physc.2015.06.011.
21. Obolenskii M.A., Vovk R.V., Bondarenko A.V., Chebotaev N.N.. – Low Temp. Phys., v. 32, p. 571, 2006.FNT97pinning.
22. Malkovich R.Sh., Matematika diffuzii v poluprovodnikah – Sankt–Piter–b., «Nauka»,1999, 390 pp.
23. Vovk R.V., Vovk N.R., Dobrovolskiy O.V. / J. Low Temp. Phys, v. 175, p. 614–630, 2014.
24. V.M. Apalkov and M.E. Portnoi, Phys. Rev. B **65**, 125310 (2002).
25. Ruslan V. Vovk, Georgij Ya. Khadzhai, Oleksandr V. Dobrovolskiy / *Appl. Phys. A* (2014) 117: 997-1002 DOI: 10.1007/s00339-014-8670-2.
26. N. Adamenko,K.E.Nemchenko,V. I.Tsyganok and A.I.Chervanev, Low Temp. Phys. 20 (1994) 498.
27. R.V.Vovk, C.D.H.Williams and A.F.G.Wyatt. / Phys. Rev. B **68**, 134508 (2003).
28. R.V.Vovk, C.D.H.Williams and A.F.G.Wyatt. / Phys. Rev. Lett. **91**, 235302 (2003).
29. P.G. Curran, V.V. Khotkevych, S.J. Bending, A.S. Gibbs, S.L. Lee, and A.P. Mackenzie, Phys. Rev. B 84, 104507 (2011).
30. R. V. Vovk, M. A. Obolenskii, A. V. Bondarenko / Fizika Nizkih Temperatur, v. 33, N 1, p. 126-130 (2007).

Вісник ХНУ, серія «Фізика», вип. 25, 2016. с. 48-51

УДК 539.4
PACS: 62.20.F-

The internal stress relaxation modeling in the polygonization in alkali halide single crystals

D.V. Matsokin, I.N. Pakhomova

V.N. Karazin Kharkiv Nation University
4 Svobody sq., 61022, Kharkov, Ukraine
e-mail: matsokin@univer.kharkov.ua

The evolution of the dislocation system during annealing in the absence of external loading after the three-point bending of a single crystal with a NaCl-type lattice, pricked out along the cleavage planes is modeled with the discrete dislocation dynamics method. The change of the average shear stresses value produced by the dislocation structure in the surrounding crystal and stresses acting on the dislocation ensemble themselves are obtained.

Keywords: dislocation dynamics, internal stress, polygonization.

Методом дискретної дислокаційної динаміки промодельовано еволюцію дислокаційної системи при вільному відпалі після триточкового згину монокристала з граткою типу NaCl, що був виколотий по площинах спайності. Визначено зміну величини середніх зсувних напружень, які утворює дислокаційний ансамбль в оточуючому кристалі, та локальних напружень, що діють на самі дислокації ансамблю.

Ключові слова: динаміка дислокацій, внутрішні напруження, полігонізація.

Методом дискретной дислокационной динамики промоделирована эволюция дислокационной системы при свободном отжиге после трехточечного изгиба монокристалла с решеткой типа NaCl, выколотого по плоскостям спайности. Определено изменение величины средних сдвиговых напряжений, создаваемых дислокационным ансамблем в окружающем кристалле, и локальных напряжений, действующих на сами дислокации ансамбля.

Ключевые слова: динамика дислокаций, внутренние напряжения, полигонизация.

Introduction

It is well known that the plastic deformation of single crystals is largely determined by the movement of dislocations. The plastic deformation velocity provided by the motion of dislocations is defined by Orovan:

$$\dot{\varepsilon} = \rho b \upsilon ,$$

where ρ – density of the moving dislocations, b – the Burgers vector value, υ – the average velocity of dislocations.

In turn, the velocity of dislocations motion depends on the applying stress and the dislocation mobility. Effective stress applied to the dislocation is the sum of the external applying stress to the sample, and the stress from all sources within the crystal (internal stresses). In a fairly pure crystals main source of stress is the dislocation ensemble.

Thus, the factors that determine the rate of the crystal deformation are: external stresses (σ_{ext}); dislocation density; dislocation mobility which depends on the temperature and relative position of dislocations (dislocation configuration); the value of the internal stress (σ_{int}), which depends on their relative position at a constant dislocation density. If the external stresses we can change (we could put a define level of the external stresses), the internal stresses are determined mainly by the prehistory of the sample (so we could not influence on a level of internal stresses).

The internal stresses for creep or active loading tend to hinder the movement of dislocations and $\sigma_{eff} = \sigma_{ext} - \sigma_{int}$. Whereas in the absence of the external influence $\sigma_{eff} = \sigma_{int}$.

The field of elastic stresses generated by dislocations is inhomogeneous. We can use superposition principle to the stress. Then the level of stress will substantially depends on the point within the crystal. Therefore, we considered it in terms of the average value of the internal stresses σ_{int}. If the value of the external stresses is insufficient for the new dislocations multiplication, it makes sense to talk about internal stresses only as a consequence of the dislocations interaction themselves.

In considering the dislocation subsystem evolution of the crystal in the absence of external stress (for example, with the annealing in the absence of external loading) the relaxation of the internal stresses will be, mainly by reducing the number of dislocations (annihilation or following dislocation to the surface). The dislocations

ensemble will change it's configuration at a sufficient temperature and time. The question arises, how the rebuilt dislocations change the internal stress?

In the literature there are conflicting data regarding this. From the fact that the internal stresses do not change till they reduce several times [1 - 3].

The internal shear stresses in the equilibrium position can be extremely small for dislocations forming a stable dislocation structure. Therefore such a dislocation can move even by applying slight external stress. However, in order to finally leave the stable structure (and contribute to plastic deformation) dislocation should overcome the potential barrier, much greater stress must be applied (for example, when the dislocation leaves the infinite symmetric tilt boundaries [4, 5]).

The problem of calculation of the field of elastic stresses generated by the dislocation ensemble has been theoretically solved in a few simple cases. For example, it was solved for an infinite symmetrical low-angle boundaries and slip bands with equidistant dislocations [4]. It is difficult to solve for intermediate dislocation configurations occurring during the self-organization process (in particular, in the polygonization) because of cumbersome calculations. Our goal was to determine by computer simulation the average shear stress value in the polygonization process. Furthermore, since the dislocation mobility is determined by elastic stress acting on them values of shear stress acting on a dislocation during polygonization are calculated.

Model description

Using discrete dislocation dynamics method we can make a forecast of dislocation ensemble evolution and estimate the share stresses values which affect on dislocation mobility.

In this paper, by the discrete dislocation dynamics modeling (detailed simulation procedure is described in [6]) the internal average shear stress relaxation in the polygonization process in alkali halide single crystals with the NaCl type lattice is considered. The crystal was pricked out along the cleavage planes and deformed under three-point bending scheme. Such a deformation scheme is convenient because in the central part of crystal basically only edge dislocations with mutually perpendicular Burgers

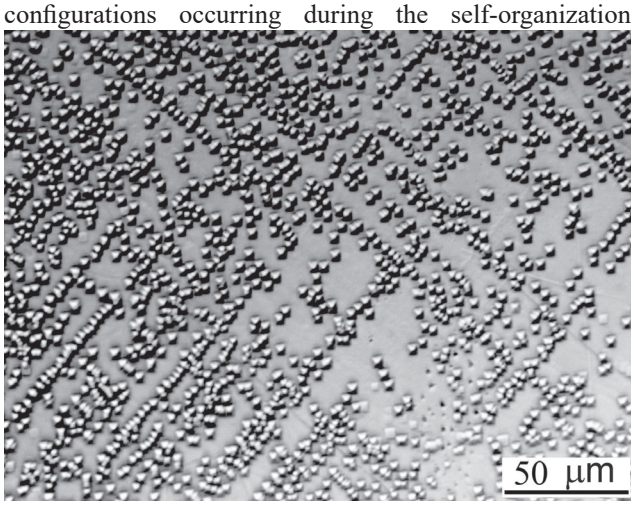

a

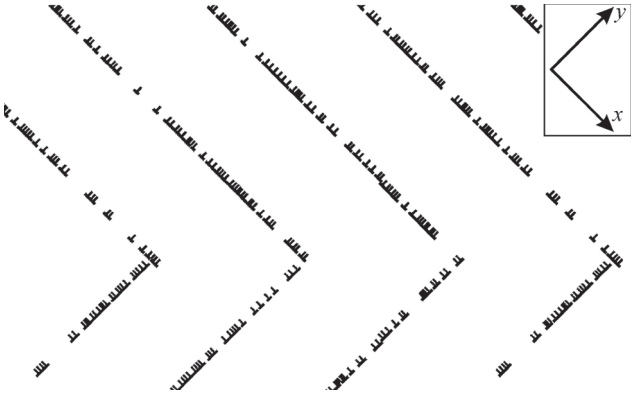

b

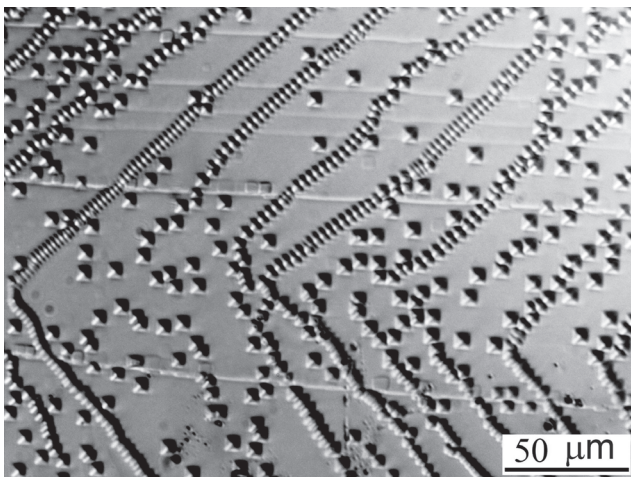

c

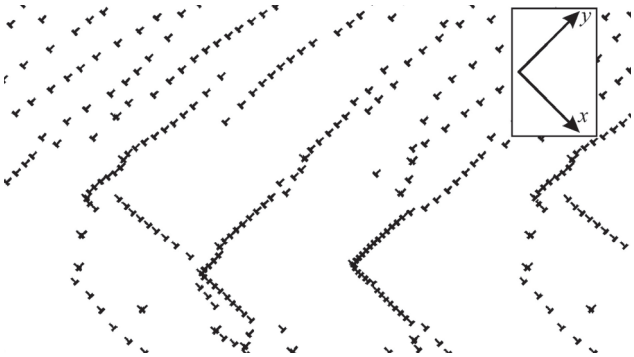

d

Fig.1. Dislocation configuration. a, b – initial distribution; c, d – $t = 200$ min , T = 550°C. NaCl.

vectors are formed. The dislocation lines are parallel to the bending axis. Then the problem of the distribution of dislocations and their movement actually becomes two-dimensional.

In this model, internal stresses are caused by the dislocations. Each dislocation produces around itself an elastic stress field. This field acts on the rest of the ensemble of dislocations. We assume that the velocity of movement of the dislocation line elements at each point is determined only by the total force acting on the element [6]. This model can be used when the radius of the dislocation line curvature greatly exceeds the average distance between dislocations.

The values of elastic moduli and the Burgers vector and parameters combining the dislocation velocity with the value of the applied stress were taken for NaCl crystals. There is easy slip system {110} <110> in crystals with the NaCl type lattice. We choose the coordinate axes so that the x and y axes are oriented along the {110}, the z axis is directed along the banding axis [001].

A system consisting of a straight edge dislocations with mutually perpendicular Burgers vectors («A» – $\vec{b}_A = (b,0,0)$ и «B» – $\vec{b}_B = (0,b,0,)$) is considered. The dislocation lines directed along the z axis. Such type of dislocations are formed in pricked out along the cleavage planes <100> crystals during three-point bending with respect to an axis parallel to the {100}.

Periodic boundary conditions were used to avoid dealing with features associated with the crystal surface. There is the rectangular area of the size $L_x \times L_y$ of the sides parallel to the Burgers vectors direction (it was determined that an arbitrary orientation of the rectangle sides in the xy plane does not change the results, if the size of the area is much larger than the average distance in the range dislocations). There are qualitatively the same results when selecting L_x and L_y in range 100 – 500 μm.

The initial dislocations distribution in the crystal deformed by three-point bending is shown (fig.1 a, b). The dislocations are located in two mutually perpendicular sliding bands. The initial dislocations positions within the area (x_i, y_i) have been set. The contents of this area was repeated 8 times in the surrounding (on the sides and corners) rectangular areas:

$$x_j = x_i + mL_x, \quad m = 0, \pm 1;$$

$$y_j = y_i + nL_y, \quad n = 0, \pm 1;$$

m and n are not simultaneously zero. The dislocation interaction with each other and with all the «clones» in neighboring areas is considered. If the dislocation leaves the selected area, such as a dislocation enters the area from the opposite side.

The first we settle the define initial dislocation arrangement by three point bending plastic deformation. After bending plastic deformation there is no external stresses, and the temperature is sufficient for the active dislocation creep. The number of dislocations is constant.

Results

In the process of modeling the average shear stress value created by the dislocation ensemble in the crystal is calculated. In order to reduce the effect of point observation location the stresses is calculated in 200 points uniformly distributed around the circumference whose radius is greater than tenfold L_x. The results are averaged.

In addition the total shear stress (normalized to the dislocation number) acting on the dislocation ensemble themselves is calculated.

The dependence of the average shear stress from time is shown in fig. 2. σ_{xy}^0 is shear stress at the initial time. It would seem that this average shear stress should be reduced

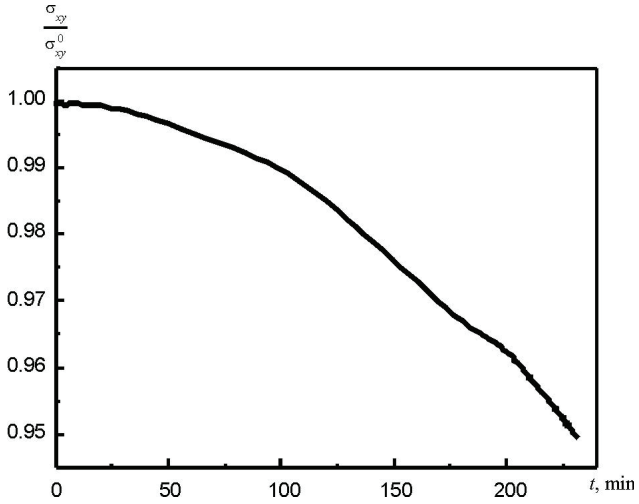

Fig. 2. The average shear stress value created by the dislocation ensemble in the surrounding crystal vs. time. T = 550°C. NaCl.

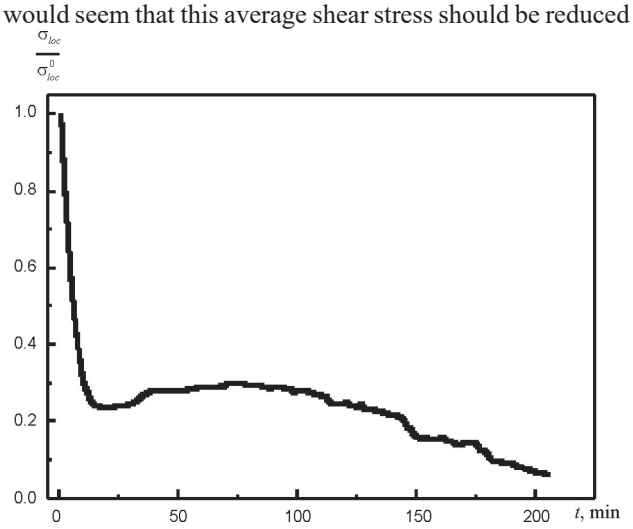

Fig. 3. The local average shear stress value created by the dislocation ensemble vs. time. T = 550°C. NaCl.

during dislocation self-organization process (from the placement of the dislocations in the slip bands to build dislocation boundaries) but average shear stress has changed near 5%. This suggests that if we considered the dislocation density reducing by annihilation process or dislocations leaving by crystal surface, then the effect we have obtained would not put evident contribution to the average shear stress reducing.

The simulation result agrees qualitatively with the conclusion reached by in [7]. Where it is stated that the dislocation self-organization in a condition of forbidden climb, the average shear stress is not changed. In our case, there are the two types of dislocation motion (sliding and climb) thus the average shear stress is reduced, although not so essential.

The internal local shear stress acting on the dislocation ensemble decreases during polygonization 5-10 times (depending on the dislocation density and the initial configuration) (fig. 3). The internal stresses relaxation must be experimentally tangible and will lead to the fact that dislocations are easier to respond to small external influences.

The simulations presented above indicate that the dislocation ensemble configuration affects significantly the level of local shear stresses acting on the individual dislocations, and has virtually no effect on the average shear stresses value produced according to the ensemble in the surrounding crystal.

References

1. T.Hasegawa, U.F.Kocks, Acta Met., V 27, 1705 (1979).
2. H.J.McQueen, L.Vazques, Materials Sciense and Engineering, V 81, 355 (1986).
3. R.J.Amodeo, N.M.Ghoniem, Phys. Rev. B41, N 10, 6968 (1990).
4. Li J.C.M. Theory of strengthening by dislocation grouping. in: Electron Microscopy and Strength of Crystals, New York (1963), P. 713.
5. D.V.Matsokin, I.N.Pakhomova, V.P.Matsokin, Visnyk KhNU, seria «Physica», 600, 89 (2003) (in russian).
6. D.V.Matsokin, I.N.Pakhomova, Visnyk KhNU, seria «Physica», 558, 85 (2002) (in russian).
7. C. Ayas, E. van der Giessen, Philosophical Magazine, V 88, N 30-32, 3461 (2008)

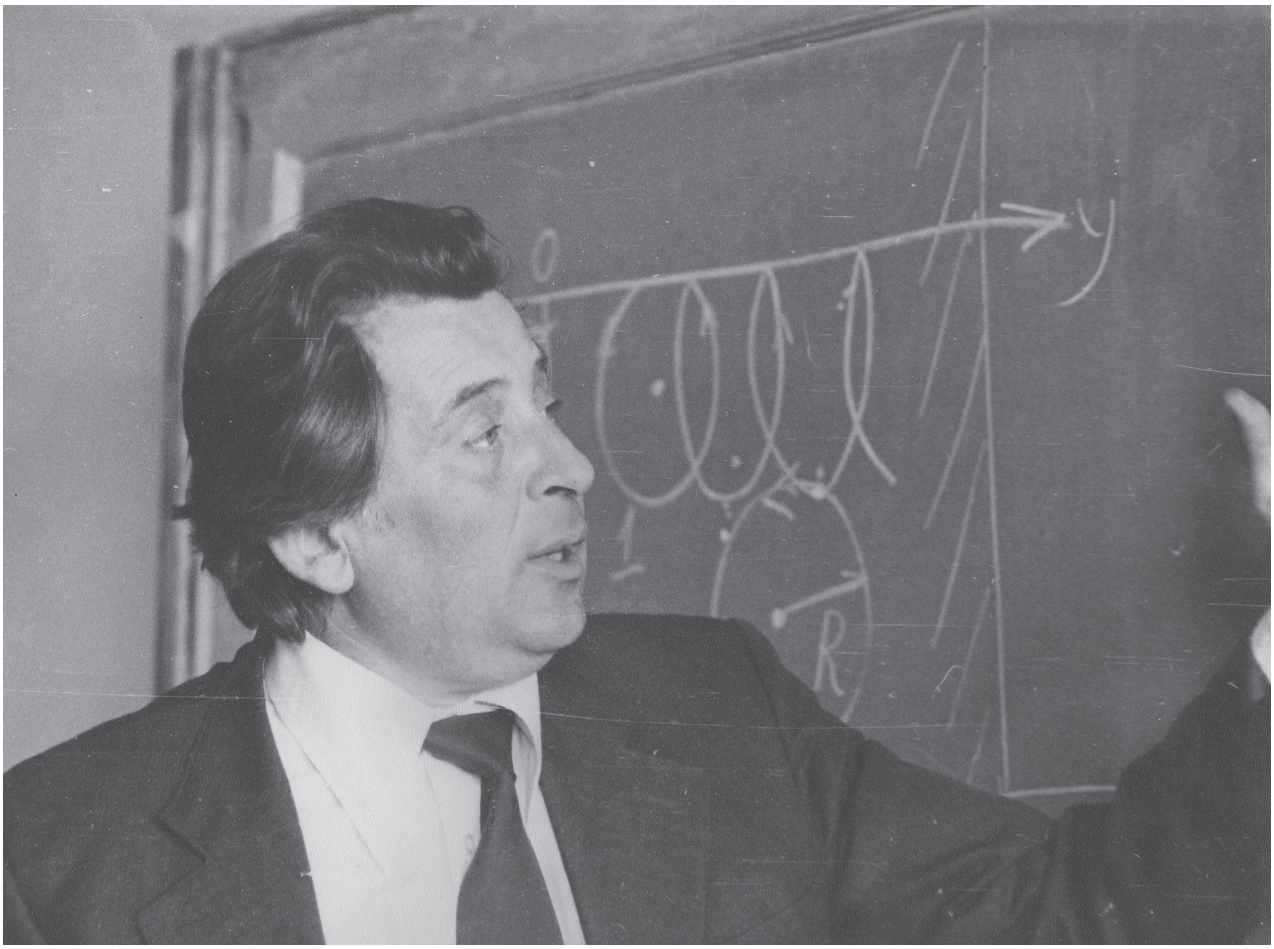

In Memoriam of Emanuil Aizikovich Kaner

Now we celebrate the 85th anniversary of Emanuil Aizikovich Kaner – a corresponding member of Ukrainian Academy of Sciences, the brilliant theoretical physicist, the outstanding scientist and teacher boundlessly devoted to science, the wonderful lecturer and educator.

E.A. Kaner was born in Kharkov on November 19, 1931. In 1954 he graduated from the Physics and Mathematics Faculty of Kharkov State University. Besides the diploma on the basic specialty "theoretical physics", he defended an experimental thesis on optics. Further, during the whole his scientific activity, E.A. Kaner was interested in experiments and much collaborated with experimenters.

E.A. Kaner was one of brilliant representatives of the theoretic school by I.M. Lifshits. The most important E.A. Kaner's investigations refer to the theory of plasma phenomena in metals. Due to the discovery of cyclotron resonance and other his works in this area, the conventional notions on a metal as a medium where any propagation of electromagnetic oscillations is impossible have been revised. E.A. Kaner predicted the existence of different types of such oscillations able to propagate deep into the metal, he revealed a new mechanism of their absorption (so-called Landau's magnetic damping), developed the theoretical concepts on the single-particle ballistic mechanism for metals anomalous transparency.

One of the first, E.A. Kaner began the investigations on magnetic acoustics of metals. He predicted the acoustical cyclotron and helicon-phonon resonances, the resonance in open orbits, giant quantum oscillations of sound speed, strong non-adiabatic effects under the electron-ion interactions; he developed the theoretical basis for the magnetic acoustic-electronics of metals on Rayleigh waves.

E.A. Kaner contributes much into the development of the problem of instability and propagation of waves in semiconductor and gas-discharge plasma – predicted a helicoid instability of coupled sound and spiral electromagnetic waves, developed the theory of a new type cyclotron parametric instability in semiconductors.

The productive scientific ideas by E.A. Kaner were realized in the statistical theory of radio-waves propagation in the turbulent troposphere and wave scattering at hydrometeors, in the area of radio-location, and other areas of the modern radio-physics. Last his years E.A. Kaner actively studied the magneto-impurity waves in metals, the problem of a magnetic breakdown, acoustic properties of low-dimensional disordered systems, non-linear electrodynamics of metals and semiconductors.

E.A. Kaner is the co-author of two fundamental discoveries: 1) The Cyclotron Resonance in Metals (Azbel-Kaner's resonance), 1966; 2) Electromagnetic Surges in Conducting Medium (anomalous propagation), 1970.

For the cycle of works on the magneto-acoustical spectroscopy of metals E.A. Kaner was awarded by the State Premium of Ukraine (1980).

For more than two decades E.A. Kaner carried out an active educational work as the Professor of Kharkov State University. He is the author of general courses on the electrodynamics and on the theory of metals. He developed a lot of tasks for teaching the theoretical physicists also nowadays.

All the methodical achievements by E.A. Kaner are based, first of all, on his highest professional level as a scientist. The communication with this outstanding scientist, brilliant and widely erudite man was a main stimulus for Kaner's learners. His principal motto, rather appeal, was the statement: "Every man should grow over himself".

E.A. Kaner successfully combined his scientific and educational activity with great organization work. He was a member of the editorial board of journals "Solid State Communications", "Physics of Low Temperatures", and "Ukrainian Physical Journal".

E.A. Kaner was a head and an active participant of a lot of scientific seminars. He asserted that the seminar is not a resting-place, but the place for the most intense scientific work. He communicated with young men very much. He considered the scientific activity as the best kind of bringing-up work. His passion and enthusiasm for science influenced much on all his learners (among them there are more than 20 Candidates and 11 Doctors of Sciences) who now actively work in many countries of the world.

Already for 30 years after E.A. Kaner's death, the International Jubilee Seminars take place in Kharkov Scientists House every five years, and annual seminars are carried out for his memory in Kharkov National University named after V.N. Karazin.

Editorial Board

ІНФОРМАЦІЯ ДЛЯ АВТОРІВ СТАТЕЙ

журналу «Вісник ХНУ». Серія «Фізика»

У журналі «Вісник ХНУ». Серія «Фізика» друкуються статті та стислі за змістом повідомлення, в яких наведені оригінальні результати теоретичних та експериментальних досліджень, а також аналітичні огляди літературних джерел з різноманітних актуальних проблем фізики за тематикою видання.

Мова статей – українська, англійська та російська.

ТЕМАТИКА ЖУРНАЛУ

1. Теоретична фізика.
2. Фізика твердого тіла.
3. Фізика низьких температур.
4. Фізика магнітних явищ.
5. Оптика та спектроскопія.
6. Загальні питання фізики і серед них: методологія та історія фізики, математичні методи фізичних досліджень, методика викладання фізики у вищій школі, техніка та методика фізичного експерименту тощо.

ВИМОГИ ДО ОФОРМЛЕННЯ РУКОПИСІВ СТАТТЕЙ

Загальний обсяг тексту рукопису статті повинен займати не більше, ніж 15 сторінок.

Рукопис статті складається з титульної сторінки, на якій вказанно: назва статті; ініціали та прізвища авторів; поштова адреса установи, в якій була виконана робота; класифікаційний індекс за системами PACS та УДК; анотації на окремому аркуші з прізвищем та ініціалами авторів і назвою статті, викладені українською, російською та англійською мовами; основний текст статті; список літератури; підписи під рисунками; таблиці; рисунки: графіки, фотознімки.

Анотація повинна бути за об'ємом не меньш ніж 500 сімволів. Стаття повинна бути структорована. Висновки потрібно пронумеровати та в них потрібні бути висновки а не переписана анотація.

Електронний варіант рукопису статті повинен відповідати таким вимогам: текст рукопису статті повинен бути набраний у форматі MicrosoftWord версії 2013, вирівнювання тексту повинне бути здійснене за лівим краєм, гарнітураTimesNewRoman, без прописних букв у назвах, букви звичайні рядкові, з полями ліворуч, праворуч, зверху і знизу по 2,5 см, формули повинні бути набрані в MathType (не нижче версії 6,5), у формулах кирилиця не допускається, символи з нижніми і верхніми індексами слід набирати в MicrosoftWord, ширина формули не більше 70 мм, графіки та фотографії необхідно подавати в графічному форматі, розрізнення не менше 300 dpi, поширення файлів повинно бути *.jpg, шириною в одну чи дві колонки, для однієї колонки розміри: завширшки 8 мм, для двох колонок – 16 мм. Масштаб на мікрофотографіях необхідно представляти у вигляді масштабної лінійки.

ВИМОГИ ДО ОФОРМЛЕННЯ ГРАФІКІВ

Товщина ліній не більше 0,5 мм, але не менше 0,18 мм. Величина літер на підписах до рисунків не більш 14 pt , але не менше 10 pt, гарнітура Arial.

ПРИКЛАД ОФОРМЛЕННЯ СПИСКУ ЛІТЕРАТУРИ

1. Л.Д. Ландау, Е.М. Лифшиц. Теория упругости, Наука, М. (1978), 730 с.
2. И.И. Іванов. ФТТ, 25, 7, 762 (1998).
3. A.D. Ashby. Phys.Rev., A19, 213 (1985).
4. D.V. Vert. In Progress in Metals, ed. by R. Speer, USA, New York (1976), v.4, p.17.

ДО РЕДАКЦІЇ НАДАЄТЬСЯ

1. Два роздруковані примірники рукопису статті, які підписані її авторами.
2. Електронна версія рукопису та дані щодо контактів для спілкування з її авторами. Для цього потрібно надіслати електронною поштою, тільки на адресу **physics.journal@karazin.ua**.
3. Направлення від установи, де була виконана робота, і акти експертизи у двох примірниках; адресу, прізвище, повне ім'я та батькові авторів; номери телефонів, E-mail, а також зазначити автора рукопису, відповідального за спілкування з редакцією журналу.

Матеріали рукопису статті потрібно направляти за адресою: Редакція журналу «Вісник Харківського національного університету імені В.Н. Каразіна. Серія: фізика», Лебедєву С.В., фізичний факультет, майдан Свободи, 4, Харківський національний університет імені В.Н. Каразіна. тел. (057)-707-53-83.

Наукове видання

Вісник Харківського національного університету імени В.Н.Каразіна

Серія “Фізика”

випуск 25

Збірник наукових праць

Українською, російською та англійською мовами.

Комп’ютерне верстання С.В. Лебедєв

Підписано до друку 28.01.2017. Формат 60x84 1/8.

Папір офсетний. Друк ризограф. Ум. друк. арк. 11,9. Обл.-вид. арк 18,7.

Наклад 100 пр. Зам. №

Надруковано: ХНУ імені В.Н. Каразіна
61022, Харків, майдан Свободи, 4.
Тел.705-24-32

Свідоцтво суб'єкта видавничої справи ДК №3367 від 13.01.09